



HAL
open science

Direct upgrading of biomass-derived compounds to fine chemicals

Marisa Ketkaew

► **To cite this version:**

Marisa Ketkaew. Direct upgrading of biomass-derived compounds to fine chemicals. Other. Université de Bordeaux; Vidyasirimedhi Institute of science and technology (Vistec), 2021. English. NNT : 2021BORD0334 . tel-03892816

HAL Id: tel-03892816

<https://theses.hal.science/tel-03892816>

Submitted on 10 Dec 2022

HAL is a multi-disciplinary open access archive for the deposit and dissemination of scientific research documents, whether they are published or not. The documents may come from teaching and research institutions in France or abroad, or from public or private research centers.

L'archive ouverte pluridisciplinaire **HAL**, est destinée au dépôt et à la diffusion de documents scientifiques de niveau recherche, publiés ou non, émanant des établissements d'enseignement et de recherche français ou étrangers, des laboratoires publics ou privés.

THÈSE EN COTUTELLE PRÉSENTÉE
POUR OBTENIR LE GRADE DE
DOCTEUR DE
L'UNIVERSITÉ DE BORDEAUX
ET DU VIDYASIRIMEDHI INSTITUTE OF SCIENCE
AND TECHNOLOGY

ÉCOLE DOCTORALE SCIENCES CHIMIQUES

SPÉCIALITÉ : Chimie-Physique

Par Marisa KETKAEW

**Amélioration de l'Utilisation de Composés Dérivés de la
Biomasse en Chimie Fine**

Sous la direction de Prof. Dr. Alexander KUHN
et de Asst. Prof. Dr. Chularat WATTANAKIT

Soutenue le 07.12.2021

Membres du jury :

M. FONTAINE, Olivier

Mme. CHAREONPANICH, Metta

M. SÁNCHEZ-SÁNCHEZ, Carlos

M. ZIGAH, Dodzi

M. KUHN, Alexander

Mme. WATTANAKIT, Chularat

Associate Professor, Vidyasirimedhi
Institute of Science and Technology
Professor, Kasetsart University
Doctor, Sorbonne University
Professor, University of Poitiers
Professor, University of Bordeaux
Assistant Professor, Vidyasirimedhi
Institute of Science and Technology

Président

Rapporteur

Rapporteur

Examineur

Directeur de thèse

Directeur de thèse

Title: Amélioration de l'Utilisation de Composés Dérivés de la Biomasse en Chimie Fine

Résumé : En raison de préoccupations énergétiques et environnementales, l'élaboration de nouveaux procédés de développement durable de produits chimiques, à partir de matières premières, est un thème de recherche en pleine expansion. Plus, particulièrement en ce qui concerne, l'utilisation de composés dérivés de la biomasse, qui peuvent être produits naturellement. Différents types de produits peuvent être dérivés de ces procédés, tels que les carburants, les cosmétiques, les parfums, les additifs alimentaires, les détergents et les plastiques. Par conséquent, la mise au point de catalyseurs pour ces processus constitue un défi majeur, tant du point de vue fondamental que du point de vue industriel. Dans cette thèse, nous allons nous concentrer sur le développement de nouveaux catalyseurs hétérogènes et aux électrocatalyseurs à base d'oxydes métalliques tels que l'oxyde de cérium (CeO_2). L'utilisation de ces matériaux ces dernières années est grandissante en raison de leurs propriétés uniques telles que leur capacité à stocker de l'oxygène ou encore leur propriété redox. De plus, les catalyseurs mis au point serviront à oxyder les bioalcools en produits chimiques, tels que la conversion de l'alcool benzylique en benzaldéhyde et les applications de valorisation de l'éthanol qui peuvent être utilisées pour produire d'autres produits chimiques et carburants à haute valeur ajoutée. En outre, l'électrochimie bipolaire est appliquée pour l'élaboration d'électrocatalyseurs. Sur la base de la distribution du potentiel, des fonctions de gradient et de sélection de site peut être réalisée. De plus, la structure et l'activité des catalyseurs seront étudiées par microscopie électrochimique à balayage (SECM) afin de comprendre la relation entre les structures et les performances électrocatalytiques. Cette thèse fournira de nouvelles connaissances pour l'élaboration de catalyseurs et d'électrocatalyseurs, dans le cadre du développement durable de produits chimiques à partir de ressources renouvelables.

Mots clés : Composés dérivés de la biomasse, Amélioration de l'alcool, Oxyde de cérium (CeO_2), Zéolithes hiérarchiques, Electrochimie bipolaire, Particules Janus, Électrocatalyseur bifonctionnel

Title: Direct upgrading of biomass-derived compounds to fine chemicals

Abstract : Owing to energy and environmental concerns, the development of new processes for sustainable production of chemicals from renewable feedstocks is one of the most interesting research topics. Among them, the direct upgrading of biomass-derived compounds has attracted attention recently. Various types of products can be derived from these procedures, such as fuel, cosmetics, perfumes, food additives, detergents, and plastic. Therefore, the development of catalysts for these processes is a major challenge from both scientific and industrial points of view. In this thesis, we will focus on the development of novel heterogeneous catalysts and electrocatalysts based on metal oxides, such as cerium oxide (CeO_2), which get more attention every year because of their unique properties such as redox property and oxygen-storage capacity. In addition, the developed catalysts will be used in the oxidation of bio-alcohols towards chemicals such as the conversion of benzyl alcohol to benzaldehyde and ethanol upgrading applications that can be used to produce other high value-added chemicals and fuel. Moreover, bipolar electrochemistry is applied for electrocatalyst elaboration. Based on potential distribution, gradient and site-selective features can be performed. Additionally, the structure and activity of catalysts was investigated by scanning electrochemical microscopy (SECM) to understand the relationship between the catalyst structures and the electrocatalytic performances. We expect that this thesis will provide novel knowledge for the development of catalysts and electrocatalysts and potential characterization methods that benefit the sustainable production of chemicals from renewable resources.

Keywords : Biomass-derived compounds, Alcohol upgrading, Cerium oxide (CeO_2), Hierarchical zeolites, Bipolar electrochemistry, Janus particles, Bifunctional electrocatalyst

Université de Bordeaux

Bordeaux INP, Site ENSCBP, 16 avenue Pey Berland 33607 France

Acknowledgement

Throughout my milestone journey, being a Ph.D. student under the cotutelle program between University of Bordeaux, France, and Vidyasirimedhi Institute of Science and Technology (VISTEC), Thailand, has been a very challenging experience of my life. This journey would not have been possible without all the support and advice I received from my supervisors and colleagues.

First of all, I would like to thank my supervisor, Prof. Dr. Alexander Kuhn, for giving me an opportunity to be part of the NSysA group at the University of Bordeaux. It has been a memorable experience for me. I appreciate his patience, precious motivation, and strong support. Additionally, I would like to thank my co-supervisor, Asst. Prof. Dr. Chularat Wattanakit, for her supervision throughout my Ph.D. I am truly thankful to her for always believing in my abilities, giving me advice, and providing me with strong motivation. I sincerely appreciate her patience, support, and understanding over these years. I would like to express my gratitude to both advisors for the opportunity to participate in the Franco-Thai exchange program. I would not have been able to complete my Ph.D. without the assistance of both supervisors.

Apart from my supervisors, I will always remember to express my deepest gratitude to Prof. Dr. Dodzi Zigah. He is my mentor for the bipolar electrochemistry and Scanning Electrochemical Microscopy (SECM) technique. I appreciate his encouragement, helpful advice, and all-around support.

Besides, I would like to take this opportunity to express my gratitude to all committees for accepting my thesis assessment as well as all helpful comments and suggestions, especially Prof. Dr. Metta Chareonpanich, Assoc. Prof. Dr. Olivier Fontaine, and Dr. Carlos Sánchez-Sánchez for accepting the invitation to join this jury as examiners.

My special thanks go to Dr. Thittaya Yuthalekha, Dr. Anawat Thivasasith for their kind advice and assistance. I would like to express my gratitude to Dr. Wannaruedee Wannapakdee, Dr. Duangkamon Suttipat, Dr. Saros Salakhum, Asst.Prof.Dr. Thidarat Imyen and Pannida Dugkhuntod for their thoughtful

suggestions, support, and joyful atmosphere. I am particularly grateful to Dr. Sunpet Assavapanumat and Sapon Butcha for sharing their electrochemistry experience and knowledge. I would like to warmly thank Sorasak Klinyod for his great assistance and nice contribution. Many thanks also go to my friends (Kachaporn, Thitapond, Panyapat, and Natchanok) and all AMPM colleagues for their friendships, encouragement, and supportive environments.

My life abroad would not be easy and memorable without friends and colleagues in the NSysA group at Bordeaux. I would like to give special thanks to Dr. Laurent Bouffier for his kindly supportive experience, Dr. Getnet Sewnet Kassahun for his great help and encouragement. My sincere thanks also go to Malinee, Pacharapon, JeongEun, Jing, Ariana, Ashwin, Jerry, and all NSysA members for their friendships, assistance, and nice environment.

I would like to acknowledge the financial support and characterization equipment from the Vidyasirimedhi Institute of Science and Technology (VISTEC). In addition, the nice experience in France was supported by Campus France and the Embassy of France in Thailand with a Ph.D. cotutelle scholarship in 2019. Many thanks also go to the staffs and scientists in VISTEC and NSysA for helping me use the instruments, set the experiments, discuss the results, and make a friendly atmosphere.

Last but not least, I would like to express my heartfelt gratitude to my family for their unconditional love, support, warm caring, and encouragement in every moment. Their dedication is limitless and priceless.

This accomplishment would not have been possible without all mentioned people above.

Marisa Ketkaew

7 December 2021

Contents

	Page
Acknowledgement	ii
List of Tables	vi
List of Figures	vii
List of Abbreviations	xvii
Chapter 1 Introduction	1
1.1 Conversion of biomass-derived compounds	1
1.2 Design of heterogeneous catalysts	3
Hierarchical zeolites	3
Noble metals	7
Metal oxides	8
Noble metal and metal oxide modified hierarchical zeolites	9
1.3 Design of electrocatalysts using bipolar electrochemistry	13
Surface modification by bipolar electrochemistry	14
1.4 Scanning Electrochemical Microscopy (SECM)	16
Chapter 2 Scope of Thesis	20
Chapter 3 Fine-tuning catalytic structures of ceria incorporated in hierarchical zeolites for ethanol dehydration	23
3.1 Introduction	23
3.2 Experimental section	25
Materials	25
Catalyst preparation	25
Characterization	27
Catalytic activity test	28
3.3 Results and discussion	29
3.4 Conclusion	47
Chapter 4 Elaboration of nanoceria-platinum modified hierarchical zeolites for selective alcohol oxidation	48
4.1 Introduction	48
4.2 Experimental section	50
Materials	50

Contents (Cont.)

	Page
Catalyst preparation.....	51
Characterization.....	52
Catalytic activity test	53
4.3 Results and discussion	54
4.4 Conclusion	69
Chapter 5 Electrochemical activity mapping of Pt-CeO ₂ gradient films prepared by bipolar electrochemistry	70
5.1 Introduction	70
5.2 Experimental section.....	72
Materials	72
Film preparation.....	72
Electrochemical System and Instrumentation	73
5.3 Results and discussion	74
5.4 Conclusion	88
Chapter 6 Bifunctional Pt/Au Janus electrocatalyst for furfural electrochemical conversion	89
6.1 Introduction	89
6.2 Experimental section.....	92
Materials	92
Method and instrumentation	92
6.3 Results and discussion	94
6.4 Conclusion	103
Chapter 7 Conclusion and thesis perspectives.....	104
Résumé	108
Summary	112
References	116
Author's Biography	138

List of Tables

Table		Page
3.1	Relative crystallinity of the prepared catalysts.	32
3.2	Elemental points analysis data.	38
3.3	Textural properties of all the prepared catalysts.	39
3.4	Acid density of all the prepared catalysts obtained from NH ₃ -TPD measurement.	41
3.5	Basic density of all the prepared catalysts obtained from CO ₂ -TPD measurement.	41
3.6	Reducibility of all the prepared catalysts obtained by using H ₂ -TPR measurement.	42
4.1	Textural properties.	60
4.2	Metal dispersion properties.	61
4.3	Quantitative analysis of Ce oxidation obtained from XANES for fresh and used catalysts.	68

List of Figures

Figure		Page
1.1	Primary energy utilization by fuels (toe = tonnes of oil equivalent). *Renewables: wind, solar, geothermal, biomass, and biofuels.	1
1.2	a) Schematic illustration of the pore size effect on the diffusion of large (red) and small (black) molecules. b) Effects of pore diameter on molecular diffusivity (D) and of the energy of activation (E_a) on diffusion.	4
1.3	Schematic illustration of accessibility and transport/diffusion limitations in conventional and hierarchical zeolites.	5
1.4	Zeolite formation around carbon particles as hard templates.	6
1.5	Summary of desilication procedures used for different Si/Al ratios.	7
1.6	The noble metals employed in catalysis can be rated by their bond-cracking capabilities.	8
1.7	Optimized structures of a) ZnO and b) ZrO ₂ clusters.	8
1.8	Relationship of reaction activity as a function of the heat of adsorption of the reactant and product on various noble metals.	10
1.9	a) The asymmetric oxygen vacancy sites of M-□(-Ce) ₃ in doped ceria. b) The redox catalytic series on an asymmetric oxygen vacancy site for aerobic oxidation of CO as a model reaction. c) Schematic illustration of correlation of the oxygen vacancy microstructure and its redox property.	11
1.10	Differences in terms of experimental set-up between a) conventional and b) bipolar electrochemical cell. The red dotted line symbolizes an ideal electric field produced between the feeder electrodes.	14

List of Figures (Cont.)

Figure		Page
1.11	a) Scheme of the principle of bipolar electrochemistry and b) Scheme indicating the driving force variation along the bipolar electrode.	14
1.12	Schematic illustration of a bipolar setup showing the different applications of bipolar electrochemistry such as electrografting, electrodeposition, sensing, and modification of graphene.	15
1.13	Schematic illustration of SECM operation modes: (a) Steady-state diffusion in bulk solution, (b) Negative feedback mode, (c) Positive feedback mode, (d) Tip generation/substrate collection mode, (e) Substrate generation/tip collection mode and (f) Redox competition mode.	17
1.14	a) Scheme of the SECM measurement setup, b) Pt UME tip current densities obtained from the SECM scan attributed to the three products of CO ₂ reduction reaction: (a) HCOO ⁻ , (b) CO _{ad} , (c) H ₂ .	18
3.1	Schematic illustration of conventional ZSM-5 preparation.	26
3.2	Schematic illustration of fine-tuned CeO ₂ preparation using different support materials including conventional ZSM-5 (ZSM5-CON), hierarchical ZSM-5 (ZSM5-HIE), and hierarchical silicalite-1 (Silicalite1-HIE); I, II, III, and IV denoted as Ce(Imp)-Silicalite1, Ce(Imp)-ZSM5-HIE, Ce(Exc)-ZSM5-HIE, and Ce(Exc)-ZSM5-CON.	30
3.3	XRD results of (A) hierarchical zeolite supports: (a) ZSM5-HIE, (b) 5Ce(Imp)-ZSM5-HIE, (c) 5Ce(Exc)-ZSM5-HIE, (d) Silicalite1-HIE, and (e) 5Ce(Imp)-	31

List of Figures (Cont.)

Figure		Page
	Silicalite1-HIE, and (B) conventional zeolite supports: (a) ZSM5-CON and (b) 5Ce(Exc)-ZSM5-CON.	
3.4	(A) XRD results and (B) Normalized Ce L3 edge XANES spectra of (a) 5Ce(Exc)-ZSM5-HIE, (b) 5Ce(Imp)-ZSM5-HIE, (c) 5Ce(Imp)-Silicalite1-HIE and (d) 5Ce(Exc)-ZSM5-CON.	32
3.5	TEM images and nanosheet thickness distribution of (A-C) Silicalite1-HIE and (D-F) ZSM5- HIE.	33
3.6	SEM images and zeolite particle size distribution of (A) 5Ce(Exc)-ZSM5-CON, (B) 5Ce(Exc)-ZSM5-HIE, (C) 5Ce(Imp)-ZSM5-HIE and (D) 5Ce(Imp)-Silicalite1-HIE.	34
3.7	SEM images of (A,B) 5Ce(Exc)-ZSM5-CON, (C,D) 5Ce(Exc)-ZSM5-HIE, (E,F) 5Ce(Imp)-ZSM5-HIE and (G,H) 5Ce(Imp)-Silicalite1-HIE employing a secondary electron detector (SE mode, left) and a low-angle backscattered electron detector (LABE mode, right), respectively.	35
3.8	TEM images and CeO _x particle size distribution of (A) 5Ce(Exc)-ZSM5-CON, (B) 5Ce(Exc)-ZSM5-HIE. (C) 5Ce(Imp)-ZSM5-HIE, and (D) 5Ce(Imp)-Silicalite1-HIE.	36
3.9	STEM-EDS images of (A) 5Ce(Exc)-ZSM5-CON, (B) 5Ce(Exc)-ZSM5-HIE, (C) 5Ce(Imp)-ZSM5-HIE and (D) 5Ce(Imp)-Silicalite1-HIE.	37
3.10	SEM-EDS elemental points analysis of (A) 5Ce(Exc)-ZSM5-CON, (B) 5Ce(Exc)-ZSM5-HIE, (C) 5Ce(Imp)-ZSM5-HIE and (D) 5Ce(Imp)-Silicalite1-HIE.	37
3.11	N ₂ adsorption/desorption isotherms of (a) 5Ce(Exc)-ZSM5-CON, (b) 5Ce(Imp)-ZSM5-HIE, (c) 5Ce(Exc)-ZSM5-HIE, and (d) 5Ce(Imp)-Silicalite1-HIE.	39

List of Figures (Cont.)

Figure		Page
3.12	Chemisorption profiles of (A) NH ₃ TPD and (B) CO ₂ TPD for (a) 5Ce(Exc)-ZSM5-HIE, (b) 5Ce(Imp)-ZSM5-HIE, (c) 5Ce(Imp)-Silicalite1-HIE, (d) 5Ce(Exc)-ZSM5-CON, and (e) commercial CeO ₂ nanoparticles.	40
3.13	Chemisorption profile of NH ₃ TPD for ZSM5-HIE.	41
3.14	Chemisorption profiles of H ₂ TPR for (a) 5Ce(Exc)-ZSM5-HIE, (b) 5Ce(Imp)-ZSM5-HIE and (c) commercial CeO ₂ nanoparticles.	42
3.15	Catalytic activity in terms of ethylene yield for different CeO ₂ loadings on ZSM5-HIE prepared by ion-exchange process: Reaction condition at 350°C after 12h of reaction time.	43
3.16	Catalytic performance of 5 wt.% of CeO ₂ on different materials: (a) 5Ce(Imp)-Silicalite1-HIE, (b) 5Ce(Exc)-ZSM5-CON, (c) 5Ce(Imp)-ZSM5-HIE and (d) 5Ce(Exc)-ZSM5-HIE.	44
3.17	Catalytic activity including ethanol conversion and product selectivity over various catalysts: (A) 5Ce(Exc)-ZSM5-HIE, (B) 5Ce(Imp)-ZSM5-HIE. (C) 5Ce(Imp)-Silicalite1-HIE and (D) 5Ce(Exc)-ZSM5-CON.	45
3.18	Catalytic activity including ethanol conversion and product selectivity over hierarchical zeolites: (A) Catalytic activity of (a) Silicalite1-HIE and (b) ZSM5-HIE and (B) Product distribution over ZSM5-HIE.	46
3.19	Catalytic activity including ethanol conversion and product selectivity of commercial CeO ₂ nanoparticles: (A) Catalytic activity, and (B) Product distribution.	46
3.20	Catalytic activity including ethanol conversion and product selectivity: (A) Catalytic performance of (a)	47

List of Figures (Cont.)

Figure		Page
	5Ce(Imp)-ZSM5-CON, (b) 5Ce(Imp)-SiO ₂ and (c) 5Ce(Imp)-Al ₂ O ₃ and product distribution of (B) 5Ce(Imp)-ZSM5-CON, (C) 5Ce(Imp)-SiO ₂ and (D) 5Ce(Imp)- Al ₂ O ₃ .	
4.1	Schematic illustration of impregnation method.	52
4.2	A) XRD patterns of Pt/CeO ₂ on hierarchical zeolites with different CeO ₂ contents: (a) Silicalite1-HIE; (b) 1Pt/5CeO ₂ -Silicalite1-HIE; (c) 1Pt/10CeO ₂ -Silicalite1-HIE; (d) 1Pt/20CeO ₂ -Silicalite1-HIE; (e) 1Pt/30CeO ₂ -Silicalite1-HIE and B) XRD patterns of Pt/CeO ₂ on hierarchical zeolites with different Pt contents: (a) 0.5Pt/20CeO ₂ -Silicalite1-HIE; (b) 1Pt/20CeO ₂ -Silicalite1-HIE; (c) 2Pt/20CeO ₂ -Silicalite1-HIE.	55
4.3	Structural information of prepared catalysts from XRD results of different nanoceria-platinum modified supports including (a) 1Pt/20CeO ₂ -Silicalite1-CON, (b) 1Pt/20CeO ₂ -Silicalite1-HIE, (c) 1Pt/20CeO ₂ -ZSM5-HIE, and (d) 1Pt/CeO ₂ .	56
4.4	SEM images of (A) 1Pt/20CeO ₂ -Silicalite1-HIE; (B) 1Pt/20CeO ₂ -Silicalite1-CON; (C) 1Pt/20CeO ₂ -ZSM5-HIE; (D) 1Pt/CeO ₂ .	57
4.5	Particle size distribution obtained from SEM images of (A) 1Pt/20CeO ₂ -Silicalite1-HIE; (B) 1Pt/20CeO ₂ -Silicalite1-CON; (C) 1Pt/20CeO ₂ -ZSM5-HIE; (D) 1Pt/CeO ₂ .	57
4.6	TEM images and the particle size distribution of (A-C) 1Pt/20CeO ₂ -Silicalite1-HIE; (D-F) 1Pt/20CeO ₂ -Silicalite1-CON.	58

List of Figures (Cont.)

Figure		Page
4.7	TEM-EDS images of (A-D) 1Pt/20CeO ₂ -Silicalite1-HIE; (E-H) 1Pt/20CeO ₂ -Silicalite1-CON.	59
4.8	N ₂ adsorption/desorption isotherms of (a) 1Pt/20CeO ₂ -ZSM5-HIE; (b) 1Pt/20CeO ₂ -Silicalite1-HIE; (c) 1Pt/20CeO ₂ -Silicalite1-CON; (d) 1Pt/CeO ₂ .	60
4.9	(A) H ₂ -Temperature programmed reduction (H ₂ -TPR) profiles of (a) 1Pt/20CeO ₂ -Silicalite1-CON and (b) 1Pt/20CeO ₂ -Silicalite1-HIE, and (B) H ₂ -TPR profiles of (a) 1Pt/20CeO ₂ -ZSM5-HIE and (b) 1Pt/CeO ₂ .	62
4.10	Schematic illustration of benzyl alcohol oxidation to benzaldehyde.	63
4.11	Catalytic activity for the selective benzyl alcohol oxidation to benzaldehyde (selectivity=100%) at 24 h of reaction time using a batch reactor at 80°C over (A) 1 wt% of Pt supported on Silicalite1-HIE combined with different CeO ₂ contents and (B) 20 wt% of CeO ₂ supported on Silicalite1-HIE combined with different Pt contents.	63
4.12	Catalytic performance of different support catalysts: (a) 1Pt/20CeO ₂ -ZSM5-HIE, (b) 1Pt/20CeO ₂ -Silicalite1-HIE, (c) 1Pt/CeO ₂ and (d) 1Pt/20CeO ₂ -Silicalite1-CON (100% selectivity towards benzaldehyde).	64
4.13	Catalytic performance for the selective benzyl alcohol oxidation to benzaldehyde (selectivity=100%) in a batch reactor at 80°C for 24 h of reaction time over 1 wt% of Pt combined with 20 wt% of CeO ₂ supported on different materials: (a) 1Pt/20CeO ₂ -Silicalite1-CON; (b) 1Pt/20CeO ₂ - Silicalite1-HIE; (c) 1Pt/20CeO ₂ -	65

List of Figures (Cont.)

Figure		Page
	ZSM5(Si/Al=400)-HIE; (d) 1Pt/20CeO ₂ -ZSM5(Si/Al=100)-HIE	
4.14	Normalized Ce L ₃ edge XANES spectra of different prepared catalysts: (a) 1Pt/20CeO ₂ -ZSM5-HIE, (b) 1Pt/20CeO ₂ -Silicalite1-HIE, (c) 1Pt/20CeO ₂ -Silicalite1-CON, (d) 1Pt/CeO ₂ and Ce ³⁺ (yellow) and Ce ⁴⁺ (pink) standard references.	66
4.15	Schematic illustration of the proposed structures of the prepared catalysts.	67
4.16	Fitting curves of XANES spectra of the Ce L ₃ edge for 1Pt/20CeO ₂ -ZSM5-HIE.	67
4.17	Schematic illustration of catalytic reaction mechanism of alcohol oxidation on Pt/CeO ₂ supported on hierarchical zeolite surfaces.	69
5.1	CV at a glassy carbon electrode in KNO ₃ 0.1 M solution (black line) containing 1 mM of CeO ₂ precursor (red line), 1 mM of Pt precursor (blue line), and both of them (pink line) with the scan rate of 50 mV s ⁻¹ .	76
5.2	SEM images of the homogeneous (a) CeO ₂ film, (b) Pt film and (c) Pt-CeO ₂ film fabricated on GC electrode at -0.6 V for 1 min.	77
5.3	X-ray photoelectron spectra fitting of Pt-CeO ₂ homogeneous film for (a) Ce 3d and (b) Pt 4f binding energy regions at 0 s, (c) Elemental analysis along the different etching time and (d) Raman spectra of Pt-CeO ₂ homogeneous film.	78
5.4	Cyclic voltammogram of the prepared electrode in H ₂ SO ₄ 0.5 M at scan rate 20 mV s ⁻¹ .	79

List of Figures (Cont.)

Figure		Page
5.5	Schematic illustration of benzyl alcohol electrooxidation to benzaldehyde.	80
5.6	Benzyl alcohol electrooxidation at the homogeneous films: CeO ₂ (black line), Pt (red line) and Pt-CeO ₂ (blue line), in KOH 0.1 M solution containing benzyl alcohol 0.2 M under room temperature at $v = 50 \text{ mV s}^{-1}$.	80
5.7	Schematic illustration of a two-step deposition on a glassy carbon electrode at -0.6 V for 1 min in each step to prepare two layers of Pt and CeO ₂ film: (i) CeO ₂ /Pt for Pt deposition first, then coated with CeO ₂ film and (ii) Pt/CeO ₂ for CeO ₂ deposition first, then coated with Pt film.	81
5.8	Benzyl alcohol electrooxidation at the homogeneous films: Pt-CeO ₂ (blue line), Pt/CeO ₂ (green line) and CeO ₂ /Pt (pink line), in KOH 0.1 M solution containing benzyl alcohol 0.2 M under room temperature with the potential scan rate = 50 mV s^{-1} .	81
5.9	Schematic illustration of bipolar electrodeposition experiment.	82
5.10	(a) SEM image and SEM-EDS line scan profiles of the Pt-CeO ₂ film fabricated by using Ce(NO ₃) ₃ 1 mM, K ₂ PtCl ₆ 1 mM and KNO ₃ 0.1 M at applied potential 1.93 V cm^{-2} for 1 min and (b-d) a higher magnification of each area of film.	83
5.11	(a) Elemental analysis from XPS of the Pt-CeO ₂ gradient film at different positions starting from the edge of the electrode and (b) Surface-enhanced Raman scattering (SERS) spectra of Pt-CeO ₂ gradient film at different positions.	85

List of Figures (Cont.)

Figure		Page
5.12	Schematic illustration of SECM measurement of Pt-CeO ₂ film fabricated by using Ce(NO ₃) ₃ 1 mM, K ₂ PtCl ₆ 1 mM and KNO ₃ 0.1 M at applied potential 1.93 V cm ⁻² for 1 min from the edge (x=0) toward the middle of the electrode (x=4000) using applied potential -0.4 V at the UME and -0.1 V at the substrate with scan rate 50 μm s ⁻¹ in a solution containing BnOH 50 mM and KOH 0.1 M.	86
5.13	Schematic illustration of SECM measurement of the Pt-CeO ₂ film fabricated by using Ce(NO ₃) ₃ 1 mM, K ₂ PtCl ₆ 1 mM and KNO ₃ 0.1 M at applied potential 1.93 V cm ⁻² for 1 min from the edge (x=0) toward the middle of the electrode (x=3000) using apply a potential of 0.5 V at the UME and 0 V at the substrate with scan rate 50 μm s ⁻¹ in solution containing ferrocenedimethanol 1 mM and KNO ₃ 0.1 M, and (c) Surface profiles of Pt-CeO ₂ gradient film determined by optical profilometer.	87
6.1	Schematic illustration of furfural conversion to furfuryl alcohol and furoic acid via reduction and oxidation reaction, respectively.	89
6.2	Calibration curves based on the integrated peak area obtained from HPLC measurement for (A) Furfural, (B) Furfuryl alcohol, and (C) Furoic acid.	94
6.3	Cyclic voltammograms of (A,C,E,G) furfural electroreduction and (B,D,F,H) furfural electrooxidation at a (A-B) Au electrode, (C-D) Pt electrode, (E-F) Ni electrode and (G-H) Cu electrode, respectively, in KOH 50 mM in the absence and the presence of 15 mM furfural using a scan rate of 20 mV s ⁻¹ .	96

List of Figures (Cont.)

Figure		Page
6.4	SEM-EDS images of (A-D) Pt bipolar electrodeposition at different potentials: (A) 20 V, (B) 40 V, (C) 60 V, (D) 70 V for 10 min, and (E-H) Au electrodeposition at different potentials: (E) 20 V, (F) 40 V, (G) 60 V and (H) 80 V for 10 min.	97
6.5	Schematic illustration of the electrodeposition process to synthesize the Pt/Au Janus particles in two steps including: (i) Pt deposition on a carbon bead and (ii) Au deposition on the opposite side by switching electric field direction.	98
6.6	(A) SEM-EDS images and (B) SEM-EDS line scan profiles of a Pt/Au Janus particle synthesized by bipolar electrodeposition at 60 V for 10 min each side.	99
6.7	Schematic illustration of a bipolar cell coupling the two opposite furfural conversion mechanisms on a Pt/Au Janus particle.	100
6.8	(A) Electrocatalytic performance of different Janus particles in KOH 50 mM with 15 mM of furfural using the bipolar cell with an applied potential of 48 V for 30 min. Red and black bars represent furoic acid and furfuryl alcohol selectivity, respectively, while the circle refers to the total furfural conversion.	101
6.9	Reusability test of 24 bifunctional Pt/Au Janus particles in KOH 50 mM with 15 mM of furfural in a bipolar cell at an applied potential of 48 V for 30 min for 3 cycles. Red and black bars represent furoic acid and furfuryl alcohol selectivity, respectively, while the circle symbol refers to furfural conversion.	102

List of Abbreviations

Ag/AgCl	Silver/Silver chloride reference electrode
BET	Brunauer–Emmett–Teller method
BnOH	Benzyl alcohol
BPE	Bipolar electrochemistry
Ce(NO ₃) ₃	Cerium nitrate
CeO ₂	Cerium oxide or ceria
CNTs	Carbon nanotubes
CO ₂ -TPD	CO ₂ temperature-programmed desorption
CON	Conventional zeolite
CV	Cyclic voltammetry
DI	Deionized water
E _a	Activation energy
EAS	Electrochemical active surface area
EDS	Energy dispersive X-ray spectroscopy
Exc	Ion-exchange method
FDCA	2,5-furan-dicarboxylic acid
GC	Gas chromatography
H ⁺	Proton
H ₂ PtCl ₆	Hexachloroplatinic (IV) acid
H ₂ -TPR	H ₂ temperature-programmed reduction
HIE	Hierarchical zeolite
HOR	Hydrogen oxidation reaction
HPLC	High-performance liquid chromatography
HZSM-5	Proton (H ⁺) exchanged ZSM-5 zeolite
Imp	Impregnation method
K ₂ PtCl ₆	potassium hexachloroplatinate(IV)
KNO ₃	Potassium nitrate
LABE	Low-angle backscattered electron detector
MOFs	Metal organic frameworks
NaOH	Sodium hydroxide

List of Abbreviations (Cont.)

NH ₃ -TPD	Temperature-programmed desorption of ammonia
OH ⁻	hydroxyl ions
PDA	Pore-directing agents
S _{BET}	BET specific surface area (m ² /g)
SDA	Structure-directing agents
SECCM	Scanning electrochemical cell microscopy
SECM	Scanning electrochemical microscopy
SEM	Scanning electron microscope
S _{ext}	External surface area (m ² /g)
Si/Al	Atomic mole ratio of Si and Al
S _{micro}	Micropore surface area (m ² /g)
STEM	Scanning transmission electron microscopy
TBPOH	Tetrabutylphosphonium hydroxide
TCD	Thermal Conductivity Detector
TEM	Transmission electron microscope
TEOS	Tetraethyl orthosilicate
TPAOH	Tetrapropylammonium hydroxide
UME	Ultra-micro electrode
V _{ext}	External pore volume (cm ³ /g)
V _{micro}	Micropore volume (cm ³ /g)
WDXRF	Wavelength-dispersive X-ray fluorescence spectroscopy
WHSV	Weight hourly space velocity
XANES	X-ray Absorption Near Edge Structure
XAS	X-ray Absorption Spectra
XPS	X-ray Photoelectron Spectroscopy
XRD	X-ray diffraction
ZSM-5	Zeolite Socony Mobil-5

Chapter 1

Introduction

1.1 Conversion of biomass-derived compounds

Alcohols as bioproducts derived from biomass have several advantages. For example, bioethanol is one of the most important alcohols, because it can be used as a fuel additive and intermediate to produce versatile high-value products, such as olefins, higher alcohols, and aromatic compounds.[1, 2] In addition, energy consumption has been continuously increasing every year, whereas typical energy resources (oil, natural gas, coal, shale oil) are decreasing. More than 75% of the energy demand is projected to come from fossil fuels in 2035 (Figure 1.1). Then, the global annual energy requirement of over 12 billion tons of oil equivalent (Btoe) generates a large CO₂ emission, approximately 39.5 Gt.[3] Therefore, it is essential to provide in an efficient way energy for daily consumption and the chemical industry. Many efforts have been focused on new catalytic processes and alternative energy resources.

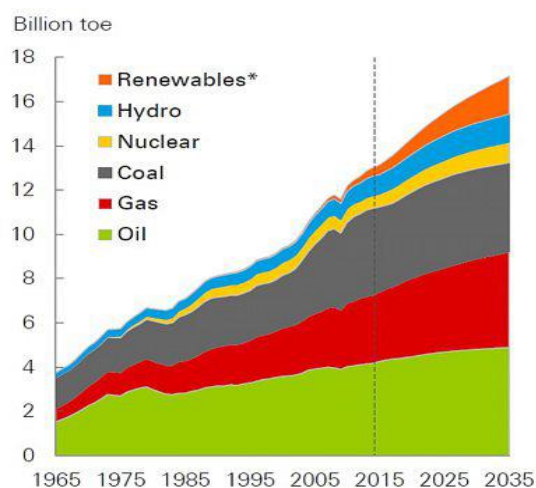


Figure 1.1 Primary energy utilization by fuels (toe = tonnes of oil equivalent).

*Renewables: wind, solar, geothermal, biomass, and biofuels. Taken from ref. [3]

Hopefully, renewable ethanol can reduce the average greenhouse gas emission against fossil fuels.[4] Therefore, not only fossil fuels have been replaced by renewable energy, but also the fine-chemicals industry tends to use alternative resources as feedstock.

Numerous studies have been devoted to the development of catalysts to achieve the transformation of biomass into higher value-added products.[5-7] Among these studies, alcohol upgrading is one of the most promising processes. For example, ethanol has been used as an initial reagent to produce many chemicals, such as paraffins, olefins, and aromatics.[8-11] To date, various solid acid catalysts have been developed for ethanol/bioethanol upgrading.[12-15] Among them, HZSM-5 zeolite has emerged as one of the best catalysts in several studies. For example, *K.B. Tayeb et al.*[15] reported the catalytic performance of ethanol on HZSM-5 zeolites with various Si/Al ratios ranging from 16 to 500. The results exhibited an excellent activity in ethanol conversion with HZSM-5 (Si/Al = 40) due to optimal fine-tuned Brønsted acid density, which is beneficial to the chemical and refining industry. For further developments, integrating various types of metals into a zeolite framework could considerably improve ethanol transformation. For instance, *M. Inaba et al.*[5] prepared noble metals incorporated in a zeolite framework for ethanol transformation. They revealed that the addition of Au into zeolite could suppress further side reactions due to the reduction of the initial acidity of the zeolite and inhibit the deposition of coke on the catalyst surfaces during the reaction, resulting in a longer lifespan of the catalyst. However, these types of catalysts are less used because of the sintering effect due to the weak metal-support interaction.[16] Therefore, other promoters or materials should be combined in order to improve the metal-support interaction. To illustrate this concept, *X. Xie et al.*[17] reported that the high catalytic performance could be attributed not only to the architecture of the catalyst, but also to the synergistic effect between CeO₂ and Pt metal. Consequently, the addition of CeO₂ is one of the most interesting approaches.[18] The publication trend in the development of CeO₂ based catalysts is increasing because CeO₂ can be used as both catalyst itself and non-inert support catalysts[19, 20] due to its redox properties ($\text{Ce}^{3+} \leftrightarrow \text{Ce}^{4+}$) and oxygen-storage capacity, which are valuable for alcohol upgrading applications.

Furthermore, metal dispersion is also an important parameter that can be easily tuned when using zeolite as a support material to improve catalytic performance.[21, 22] To further develop, the modification of zeolite structures, such as the incorporation of additional meso- or macroporous structures, namely hierarchical zeolites, have been studied to overcome the diffusion limitation of originally microporous zeolite because of their higher surface area and tunable porosity.[23-25] Moreover, due to the aforementioned catalytic properties, the modified materials possessing designed properties were used for various alcohol upgrading (e.g., benzyl alcohol and ethanol) to desired products. Therefore, in this work, we focused on the design materials having potential properties for upgrading applications. For instance, the oxidation reaction of benzyl alcohol can be used to produce benzaldehyde by using a modified hierarchical zeolite catalyst under an environmentally friendly condition.[26]

1.2 Design of heterogeneous catalysts

As stated above, metal-CeO₂ modified zeolite is one of the most promising catalysts. The development of metals supported on hierarchical zeolite catalysts to demonstrate the improved properties such as nature of active species, the dispersion of active sites and metal-support interaction to enhance the catalytic activity of alcohol upgrading is illustrated in the following.

1.2.1 Hierarchical zeolites

Zeolites are aluminosilicate crystalline structures involving tetrahedral SiO₄ and AlO₄ as primary building units, associated with the division of one oxygen atom for two tetrahedra in order to form 3D frameworks with porous structures at molecular dimensions (typically 0.25–1 nm).[27] They have played an important role in many industrial processes due to their numerous distinctive properties, involving high specific surface area, strong acidity, good ion-exchange capability, and most significantly, high thermal/hydrothermal stability.[28-30] However, the active sites of microporous zeolites turn out to be unreachable since bulky molecules cannot penetrate into active sites, which are normally located in a microporous framework due to the strong diffusion limitation of guest molecules inside a small microporous network.[31] Diffusion mechanisms are generally observed over solid materials containing mesopores (Knudsen regime) and macropores (molecular regime)).[32] The low diffusivities in micropores decrease the transfer of several substances to and

from active sites. The slow transportation of reagents facilitates the transformation of adsorbed molecules to undesired by-products, which can additionally produce coke precursors. This initiates a blocking of the micropores, eventually leading to catalyst deactivation and shortening of its lifespan. Consequently, only the outer part of the zeolite is involved in the catalytic reaction, whereas the interior remains catalytically inactive, as shown in Figure 1.2.

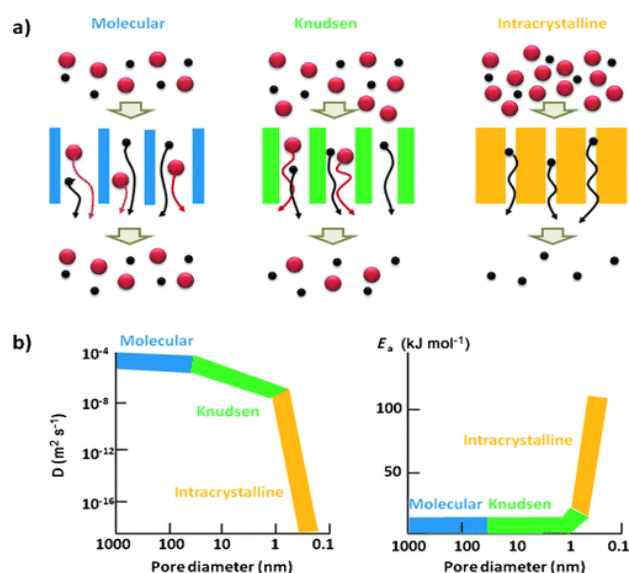


Figure 1.2 a) Schematic illustration of the pore size effect on the diffusion of large (red) and small (black) molecules. b) Effects of pore diameter on molecular diffusivity (D) and of the energy of activation (E_a) on diffusion. Taken from ref. [33]

Therefore, many efforts have been made to overcome these limitations of zeolites. One of the most promising strategies is to introduce an additional pore network with a diameter larger than 2 nm (meso- or macropores) to produce hierarchical zeolites. This approach intends to accelerate the accessibility of large molecules to the active centers of the materials, while the acidity and crystallinity of zeolites are maintained.

Hierarchical zeolites, with at least two levels of porous structures, have been continuously developed to improve the accessibility and molecular transport of guest molecules.[34] The benefits of hierarchical zeolites are shown in Figure 1.3, the yellow spheres are large molecules, which suffer from a low diffusion in a microporous network. Obviously, the secondary porosity improves the number of pore mouths that

can increase the diffusion of molecules through the pores (indicated by the green spheres). For the modified zeolite, the increase of the exterior surface regularly conducts the improvement of reactivity and selectivity. The red dots stand for bulky molecules, which can only react on pore mouths, increasing the opportunity for big molecule transformation.

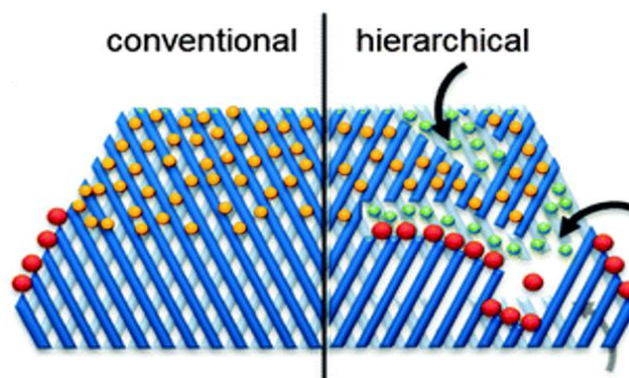


Figure 1.3 Schematic illustration of accessibility and transport/diffusion limitations in conventional and hierarchical zeolites. Taken from ref. [35]

Typically, there are two main approaches for producing hierarchical zeolites. The first one is primary synthesis, namely “Bottom-up”, which typically employs templates. Another approach is post-synthetic adjustments, namely “Top-down”, which comprises the treatment of completed zeolite.

1.2.1.1 Bottom-up approach

The bottom-up approach is based on using a template to modify the zeolite structure. In the procedure, the synthesis gel is typically composed of a molecular structure-directing agent (SDA), which is accountable for the micropore structure, and an additional template acting as a mesoporegen to create the desired mesoporous structures. The synthesis of hierarchical zeolites can be achieved by following one of the two approaches: (i) “hard” and (ii) “soft” templating methods. For the hard templating approach, rigid or solid materials containing various types of carbon materials, such as carbon nanoparticles,[36, 37] carbon nanotube,[38] ordered mesoporous carbons,[39, 40] have been widely used. After removing the templates, mesopores are present in the porous zeolite network. For example, larger pores can be generated after the combustion of carbon particles, as shown in Figure 1.4. Apart from carbon materials, a polymer such as a polystyrene[41] can also be used as a

mesoporous template. The polymer can be simply eliminated by calcination under air atmosphere. However, the main drawback of this process is that the high temperature leads to polymer glassification.[32] Additionally, soft templates such as surfactant,[42] block-copolymer,[43] and organosilane[44, 45] have also been widely used as template materials, which can induce the secondary porosity during the zeolite formation. For instance, *R. Ryoo et al.*[46] reported hierarchical zeolite synthesis using a surfactant. Compared to amorphous silica and bulk silica zeolite, the surfactant-guided zeolite nanosheets displayed an extraordinarily long catalytic lifespan and high product selectivity for the cyclohexanone oxime conversion to ϵ -caprolactam, which can be used as a precursor of Nylon-6 synthesis.

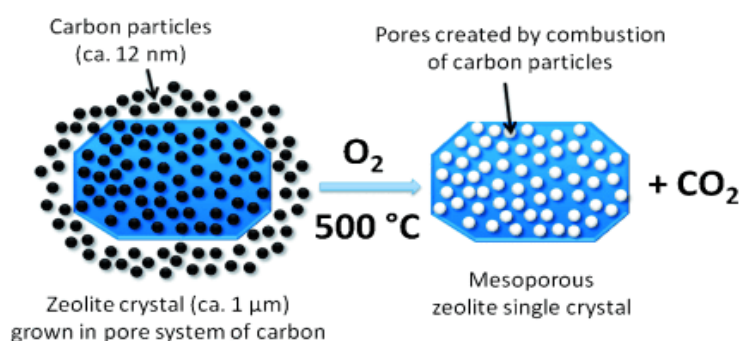


Figure 1.4 Zeolite formation around carbon particles as hard templates. Taken from ref. [37]

1.2.1.2 Top-down approach

The top-down method starts with the original microporous zeolites, which are transformed to hierarchical zeolites via a post-synthetic procedure. After synthesizing microporous zeolites, amorphous regions in the zeolite framework can be produced via special treatment, including dealumination or desilication. These amorphous regions can provide mesopores after their removal. For example, Figure 1.5, illustrates schematically the desilication procedure for zeolites with various Si to Al ratios starting from low to high ratios. Interestingly, Figure 1.5(a) demonstrates that the zeolite with a low ratio of Si/Al provides the displaced AlO_4^- -tetrahedra assemblies at the zeolite mesopore sides. A secondary acid wash can release mesopore blockage. However, in the case of Figure 1.5(b), a one-step standard desilication of the medium Si/Al zeolite is achievable (0.2 M NaOH, 30 min, and 65 °C). For a high ratio of Si/Al, with a lower stability (Figure 1.5(c)), the typical conditions cause an extreme dissolution. Therefore, alternative procedures such as using milder bases,

recrystallization with surfactants, adding pore-directing agents (PDA), and partial detemplation were used for desilication.

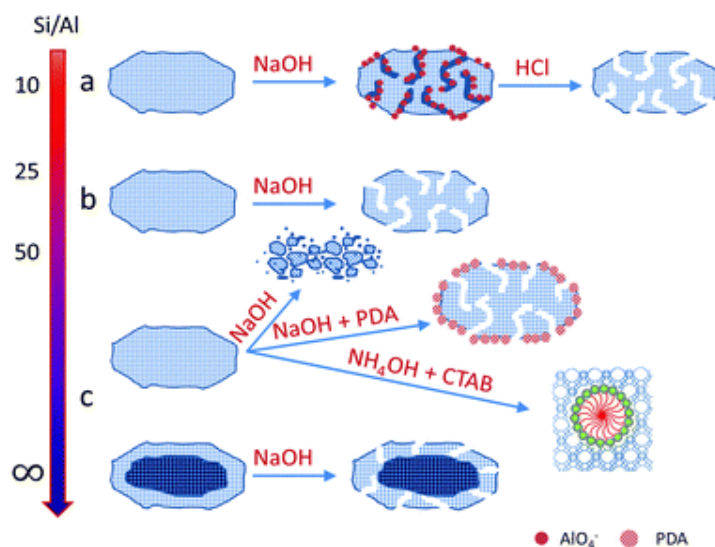


Figure 1.5 Summary of desilication procedures used for different Si/Al ratios. Taken from ref. [47]

As mentioned above, because of the outstanding properties of hierarchical zeolites, they have been broadly employed as catalysts or support materials for various reactions.[48] Especially, due to their high catalytic performance, noble metals supported on zeolites are widely employed for many reactions, such as selective oxidation of CO, hydro-addition reactions to alkynes and alkenes.[49, 50]

1.2.2 Noble metals

Noble metals are materials that can resist corrosion and oxidation in moist air. One valuable aspect about the differences between noble metals is to categorize them regarding bond-breaking ability.[51] Noble metals have been widely used in various industries because of their high efficiency to catalyze reactions and their bond-breaking capabilities.[52] Because numerous transformations are required in catalysis, these processes need different selectivities and specificities of the catalyst to break bonds. Hence, the capability of each metal to interact specifically with certain chemical bonds is revealed. Figure 1.6 displays examples of noble metals employed in catalysis with their bond-cracking capabilities.

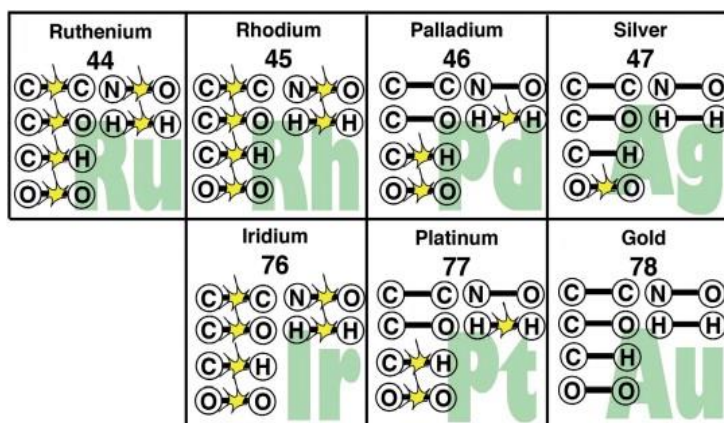


Figure 1.6 The noble metals employed in catalysis can be rated by their bond-cracking capabilities. Taken from ref. [51]

1.2.3 Metal oxides

Metal oxides represent a class of inorganic materials that have been used for various applications ranging from biomedical features,[53] sensors,[54, 55] to catalysts,[56] and energy storage[57]. Typically, oxide surfaces are terminated by oxide O^{2-} anions, as shown in Figure 1.7. Consequently, the M^{n+} cation symmetry is disturbed at the surface. Furthermore, several kinds of defects and environments (kinks, steps, terraces) can be obtained at the surface of an oxide, resulting in different catalytic properties.

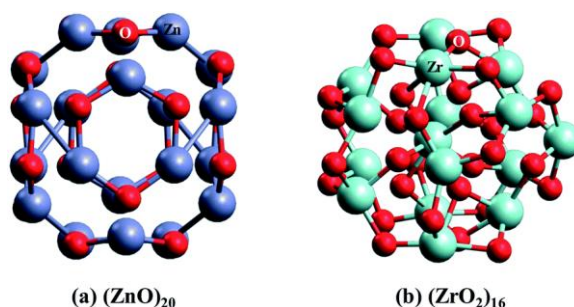


Figure 1.7 Optimized structures of a) ZnO and b) ZrO_2 clusters. Taken from ref. [58]

Metal oxides possess distinct properties, for instance, acidity and basicity (Lewis and Brønsted) and redox performance, leading to distinctive catalytic properties. In catalysis, the crucial considerations that influence the metal oxide properties are the surface area of materials involving the number of atoms within the metal oxides. The metal oxide performance is improved by reducing the particle size to the nanoscale, approximately 1 to 100 nm size range, leading to enhanced catalytic

performances per unit weight compared to their bulk structure. An increase in surface area results in a higher amount of surface atoms, influencing the optical, electrical, and magnetic properties of metal oxide nanoparticles and eventually improving their reactivity and strength.[53] Thus, the utilization of metal oxides at the nanoscale has been considered as a significant factor in the development of new properties and functions for catalysis.

In addition, metal oxides, such as alumina, silica, silica-alumina, porous oxides, and MOFs, can be employed as support materials for other active species like noble metals. Their combination can impact the catalytic features because of the complementary effect between active materials and metal oxide surface interactions.

1.2.4 Noble metal and metal oxide modified hierarchical zeolites

As stated above, noble metals have been used for various reactions because of their high efficiency.[52] However, their high cost limits their use. Therefore, using noble metals as catalysts but still keeping the costs low has attracted increasing attention over the past decades. Several reports illustrate the development of various strategies to reach this goal. Among the most interesting solutions are, using supporting materials, improving the structure or morphology of the catalyst, and finding new synergies between materials.[59, 60] The strong interaction with support materials, such as ZrO₂,[61] Al₂O₃,[62] TiO₂[63], and CeO₂[64, 65], can also enhance the catalytic activity. Especially, CeO₂ (ceria) has been widely used in the catalysis field. The outstanding feature of ceria is enhanced when combining it with various precious metals such as Pt, Pd, Ru, and Rh. The combination is not only preventing the noble metal from sintering but also allows stabilizing the dispersed states. In 2004, *A. Corma et al.*[66] studied the synergistic effect between Au and CeO₂ to increase the catalytic performance for CO oxidation. They found that the combination of Au and CeO₂ promotes catalytic activity due to the presence of Ce³⁺ ions on the nanocrystalline support surface that is able to adsorb and stimulate O₂, enhancing the catalyst reactivity. In 2009, *M. Inoue et al.*[67] developed Ru combined with CeO₂. Interestingly, a 60% yield of benzaldehyde can be achieved over 2%Ru/CeO₂. The surface Ce⁴⁺ reduction was greatly enhanced by Ru species distributed on CeO₂. Recently, *R. Bal et al.*[68] reported the partial oxidation of methane to synthesis gas (a mixture of CO and H₂) over Pt/CeO₂ catalyst. As stated above, the combination of

noble metals and CeO₂ can enhance the catalytic performance up to 80% of methane transformation at 600°C. For this case, the high catalytic activity is related to the fact that smaller particles, easily reducible, can enhance the catalytic activity. *R. Li and J. Fan et al.*[69] reported the synthesis of three types of simple Pt–CeO₂ hybrid nanostructures: nanoflowers, nanonecklaces, and nanosatellites. The modified morphology of CeO₂ prolongs the catalytic lifetime compared to conventional Pt nanoparticles due to the inhibition of metal aggregation. In particular, Pt, which exhibits the highest efficiency among the noble metals (see Figure 1.8), has been widely investigated. In addition, many strategies can be used to improve the catalytic performance of Pt-based catalysts. Due to powerful bond-breaking abilities but expensive, Pt should be modified with other metals to improve reaction selectivity and enhance metal dispersion for cost-effectiveness.[70]

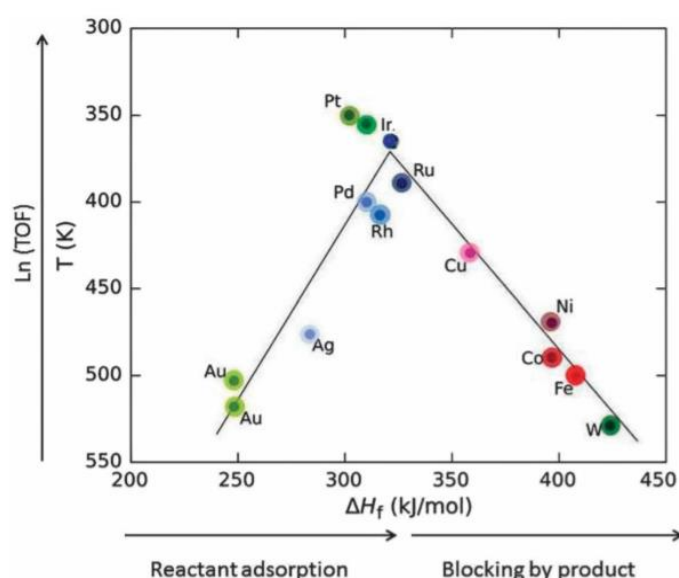


Figure 1.8 Relationship of reaction activity as a function of the heat of adsorption of the reactant and product on various noble metals. Taken from ref. [71]

Besides, for further clarification, the combination of Pt and CeO₂ can form asymmetric sites assigned as M–O(–Ce)₃ or M–□(–Ce)₃, where M refers to metal and □ symbolizes an oxygen vacancy (Figure 1.9(a)). These sites can be defined as “asymmetric oxygen vacancies”, which can play a key role as active sites in several redox reactions (Figure 1.9(b)). In these asymmetric sites, different surrounding cations influence different oxygen occupancy and redox properties. Figure 1.9(c) illustrates the generated asymmetric oxygen vacancy sites of M–□(–Ce)₃ and their

influence on the catalytic behavior of the oxides.[72] It can be seen that the modified CeO_2 with other metals can have a great impact on its redox properties due to different oxygen storage-release capabilities. Compared to symmetric vacancy sites, asymmetric vacancies can be easily filled and released by adsorbed oxygen species, identified as the intrinsic active sites in a redox reaction, enhancing their catalytic performance. While symmetric vacancies prefer to be filled by adsorbed oxygen species but are difficult to release oxygen for $\text{Ce}-\square-(\text{Ce})_3$, and the reverse results can be obtained in the case of $\text{M}-\square-\text{M}$.

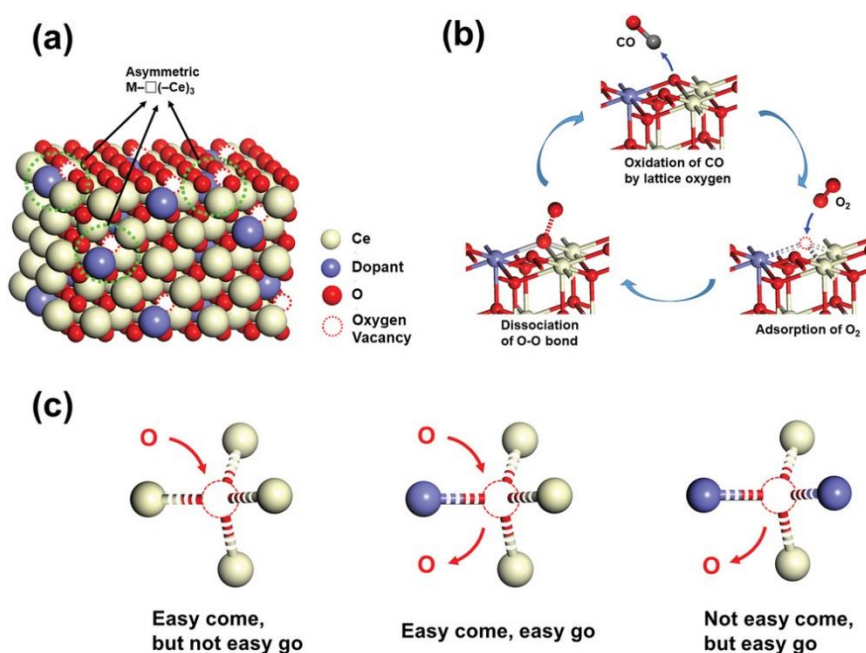


Figure 1.9 a) The asymmetric oxygen vacancy sites of $\text{M}-\square-(\text{Ce})_3$ in doped ceria. b) The redox catalytic series on an asymmetric oxygen vacancy site for aerobic oxidation of CO as a model reaction. c) Schematic illustration of correlation of the oxygen vacancy microstructure and its redox property. Taken from ref. [72]

Owing to the outstanding properties of zeolites, they have been widely used as support materials. Materials, which can provide highly dispersed active sites, are required. Compared to the conventional $\gamma\text{-Al}_2\text{O}_3$ support material, zeolite has some distinct physical properties, such as an adjustable Si/Al ratio, special three-dimensional channels, and a huge surface area.[73] As mentioned, Pt agglomeration should be avoided to retain high catalytic activity. Thus, the high surface area of zeolite as support plays a key role because of its exceptional ability to maintain the Pt

nanoparticles dispersed, which is crucial to attaining the catalyst performance stability. Furthermore, metal oxides, especially CeO₂, are used to promote the performance of active sites. An optimized amount of CeO₂ can be used to disperse Pt on the support and adjust the support acidity, eventually suppressing the formation of side reactions and coke deposition.[74-76]

For further understanding the catalysis process, apart from the heterogeneous catalyst, the metal-CeO₂ modified materials are also interesting for electrocatalytic systems. *P.K. Shen et al.*[77] have successfully fabricated a Pt-CeO₂/C catalyst for ethanol electrochemical oxidation. They found that the addition of CeO₂ to Pt catalyst could considerably enhance the performance of the electrode, especially in poisoning tolerance. Oxygen-containing molecules can be transformed from CO-like poisoning species on Pt to CO₂ at low potential, providing the available active Pt sites for more electrochemical reactions. Similar results can be observed for methanol electro-oxidation. For example, *X. Qiu et al.*[78] discovered CeO₂ as a co-catalyst together with Pt for electro-oxidation of methanol. Pt and CeO₂ modified carbon nanotubes (CNTs) as Pt-CeO₂/CNTs catalysts were synthesized. In contrast with Pt supported on CNTs, Pt-CeO₂/CNTs demonstrated higher catalytic performance and lower potential for CO stripping, suggesting that CeO₂ can facilitate the electro-oxidation of CO, which is useful for CO and methanol electro-oxidation. Additionally, CeO₂ can enhance not only poisoning resistance, but also active site dispersion of electrocatalyst. *C-T Yeh et al.*[79] reported the synthesis of Pt-Ru/C catalyst combined with CeO₂. The promotion of CeO₂ was ascribed to an expanded alloy particle dispersion. The highest-exposed surface area of Pt-Ru nanoalloys displayed the best electroactivity for the oxidation of methanol. Recently, *A.O. Neto et al.*[80] developed CeO₂ crystals as a support material for Pt nanoparticles as electrocatalysts for oxidation of ethanol. Compared to Pt/C, the nanocomposite demonstrated much higher mass activity and considerably enhanced anti-poisoning capability. The superior activity was assigned to improved metal-support interactions between CeO₂ and metal coupled with a shrinkage of the CeO₂ bandgap assisting the electron transport from the Pt-CeO₂ boundary to the strongly adsorbed byproducts. In addition, *H. Yu et al.*[81] have successfully developed Ir/CeO₂-C for the hydrogen oxidation reaction (HOR). The extremely dispersed Ir nanoparticles can be ascribed to the strong metal-support interaction of Ir and CeO₂. The improved electrocatalytic

performance is also due to the oxophilic effect owing to the sophisticated oxygen storage-release ability of CeO₂.

As mentioned above, CeO₂ has been widely used as electrocatalysts for various reactions due to its great properties when combined with other metals, eventually enhancing the catalytic performance.[24, 82] To extend the scope of the designed catalyst apart from heterogeneous catalyst preparation, the elaboration of catalysts using electrochemical approaches is a low cost, easy process, combined with a controllable selectivity as shown in more detail below.

1.3 Design of electrocatalysts using bipolar electrochemistry

In electrochemistry, current can be used to perform organic synthesis reactions using electron transfer at the interface between the electrode surface and the species in solution. For this purpose, an external power supply connected with two electrodes, including cathode and anode, is employed to provide power to the system. In contrast to the classical electrochemical setup, a bipolar electrochemical system contains a pair of driving electrodes linked to an external power supply together with a bipolar electrode (BPE) located between the driving electrodes.[83, 84] Such a wireless BPE can perform cathodic and anodic reactions simultaneously, as shown in Figure 1.10(b). As there are no direct electrical connections, the key benefit of BPE over conventional electrochemistry is that objects can be modified in a true bulk process with almost no limitations with respect to shape, size, and the quantity of BPEs. Therefore, these features offer interesting perspectives to design reaction systems.[85]

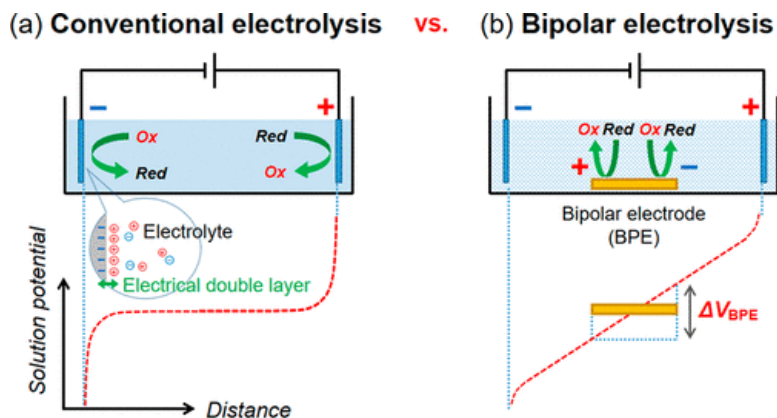


Figure 1.10 Differences in terms of experimental set-up between a) conventional and b) bipolar electrochemical cell. The red dotted line symbolizes an ideal electric field produced between the feeder electrodes. Taken from ref. [85]

1.3.1 Surface modification by bipolar electrochemistry

In bipolar electrochemistry, the potential changes linearly through the electrolyte, and an interfacial polarization occurs along the conductive object. The polarization of the electrolyte and the BPE induces reactions at the two ends of the BPE. Moreover, a potential gradient is formed along the BPE.[86] The schematic diagram of the principle of bipolar electrochemistry presents a potential drop across the BPE, as shown in Figure 1.11.

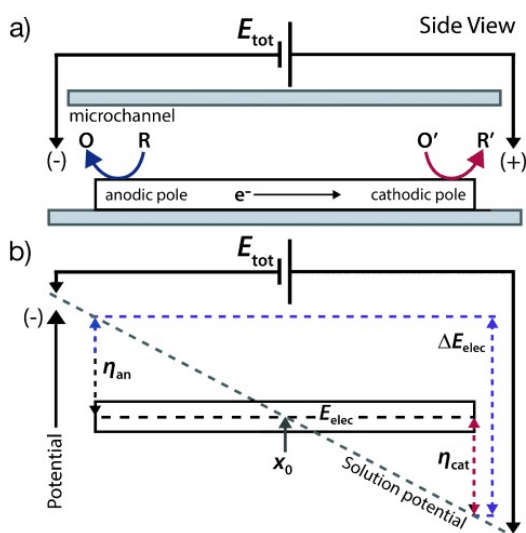


Figure 1.11 a) Scheme of the principle of bipolar electrochemistry and b) Scheme indicating the driving force variation along the bipolar electrode. Taken from ref. [86]

Based on this polarization, reduction and oxidation reactions take place at the two opposite sides of the BPE. This offers site-selective functionalization, such as cathodic deposition. The feature gives access to various surface modifications such as electrografting,[87] electrodeposition,[88] and sensing,[89] as shown in Figure 1.12. Furthermore, the potential drop across the BPE provides means for gradient generation. For instance, *Bouffier et al.*[90] studied the formation of a metal gradient with up to three different metals, including copper, nickel, and zinc on a flat gold electrode. It was found that bimetallic or trimetallic gradients can be successfully deposited in a single experiment. The variation of the chemical composition along the BPE surface can be predicted based on the different standard potentials. Thus, bipolar electrochemistry is a simple method to generate chemical gradients on a bipolar electrode.

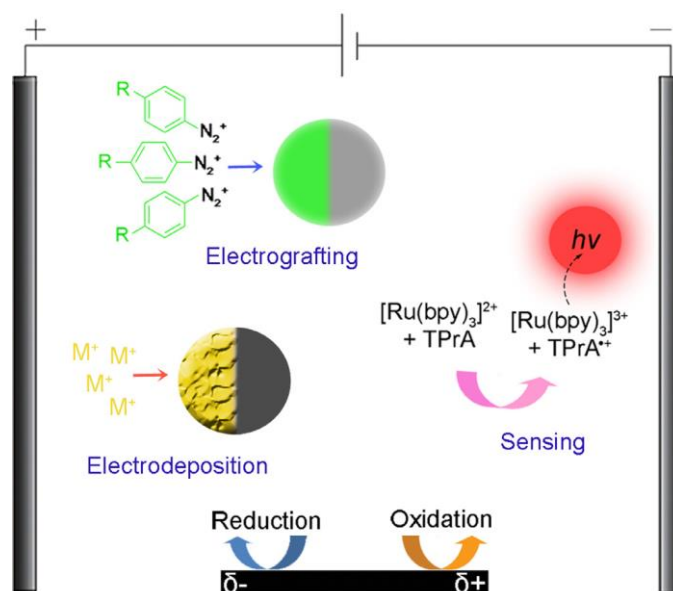


Figure 1.12 Schematic illustration of a bipolar setup showing the different applications of bipolar electrochemistry such as electrografting, electrodeposition, sensing, and modification of graphene. Taken from ref. [91]

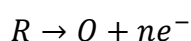
Especially gradients of electrocatalysts with varying properties can be generated in this way. Their local electrochemical properties be characterized among others by scanning electrochemical microscopy (SECM), an interesting technique for the local investigation of electroactivity.

1.4 Scanning Electrochemical Microscopy (SECM)

Scanning electrochemical microscopy (SECM) will be used to investigate the structure and functionality of the catalyst layers. SECM is quite unique among scanning probe techniques since it can image the electrochemical activity, i.e., the reaction rate at surfaces.[92, 93] In general, the information of topology and discrete variations in conductivity and chemical reactivity is accessible at high resolution from SECM measurements. This technique of chemical imaging is based on a mobile ultramicroelectrode (UME). The tip is scanned at a close distance across the surface of the sample, and its current response is immediately monitored as a function of the x-axis and y-axis tip position,[94] as shown in Figure 1.14(a). SECM imaging relies strongly on the measurement of the electrochemical tip response as a function of the tip-to-sample distance and the sample's surface properties with respect to its electrochemical activity/conductivity.[95, 96] The current response leads to an electrochemical image of the topographical feature.[97, 98]

1.4.1 SECM operation modes

According to various purposes of SECM experiments, different operation modes can be applied, as shown in Figure 1.13.[96, 99] The following equation shows the SECM study based on a reduced species "R" existing as a free redox mediator in the bulk solution, which gets oxidized to the oxidized species "O" by a polarized UME.



In a bulk solution when the tip is placed at a large distance away from the substrate, a steady-state diffusion-limited current, $i_{T,\infty}$, is established, as shown in Figure 1.13(a). In feedback mode, the conductive nature of the substrate can be determined using the recorded current from the UME tip (i_T). The insulator or non-active substrate demonstrates the negative feedback due to a consequence of the physical hindering of the diffusion of the redox mediator to the electrode surface by the substrate (Figure 1.13(b)), producing a decrease in the recorded current ($i_T < i_{T,\infty}$). While the conductor or electrochemically active substrate shows positive feedback (Figure 1.13(c)) which means the substrate can immediately reduce the formed oxidized species leading to an increase of the tip current ($i_T > i_{T,\infty}$). In generation/collection mode, the electrochemically active redox mediator is produced at either the probe electrode or the substrate electrode. If the production of the redox mediator is at the substrate

surface and then reacts electrochemically on the tip, this is called substrate generation/tip collection (SG/TC) mode, Figure 1.13(d). Conversely, if the production of the redox mediator is at the UME probe surface and then reacts electrochemically on the substrate, this is called tip generation/sample collection (TG/SC) mode, Figure 1.13(e). These generation/collection modes offer higher sensitivity due to lesser background currents. Compared to feedback mode, this measurement can be achieved at larger distances between the tip and the substrate. Moreover, lesser background current can be achieved compared to TG/SC mode by using the redox competition mode (RC) based on the competition for the same analyte between the tip and the substrate, as shown in Figure 1.13(f). Therefore, to obtain a high resolution of SECM imaging, the selection of operation SECM mode plays an important role depending on many factors such as the source, concentration of analytes, background current, and the electrochemical reactions in the solution.

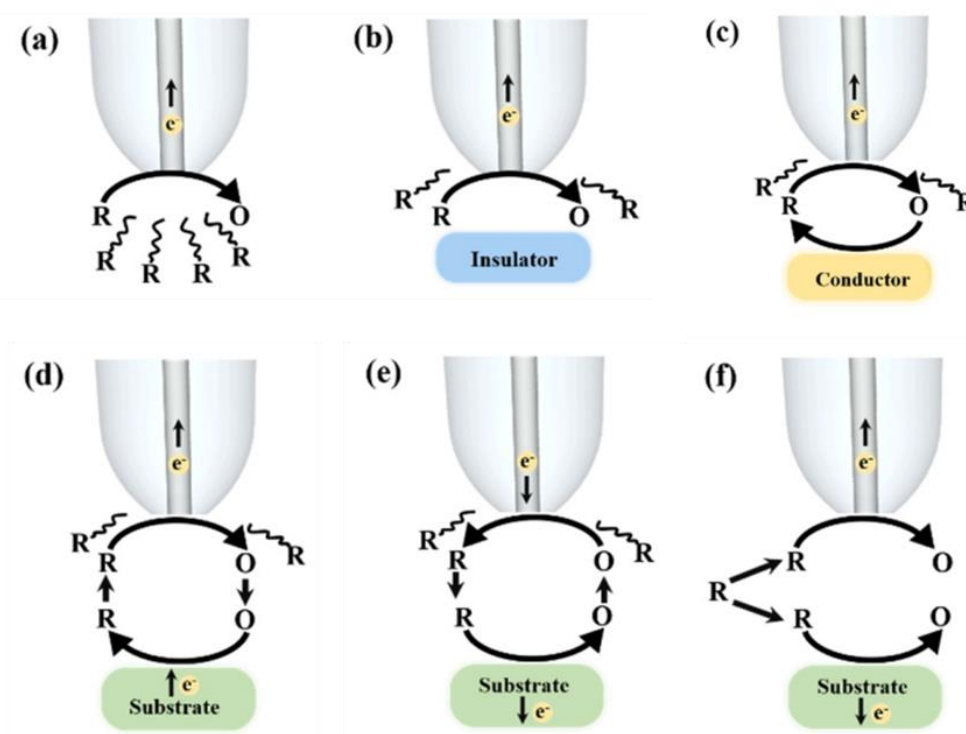


Figure 1.13 Schematic illustration of SECM operation modes: (a) Steady-state diffusion in bulk solution, (b) Negative feedback mode, (c) Positive feedback mode, (d) Tip generation/substrate collection mode, (e) Substrate generation/tip collection mode and (f) Redox competition mode. Taken from ref. [99]

For example, Gyenge *et al.*[100] reported simultaneous SECM scans using SG/TC mode over a catalyst array composed of three Sn/SnO_x catalysts for the CO₂ reduction reaction (see Figure 1.14(b)). They demonstrated distinct electrocatalytic activities for the three compositionally and morphologically different Sn/SnO_x catalysts quantified by in situ detection of the products (HCOO⁻, CO, and H₂) at a Pt ultramicroelectrode. These findings can provide a better understanding of catalytic features and more specifically the role of metal modified electrocatalyst.

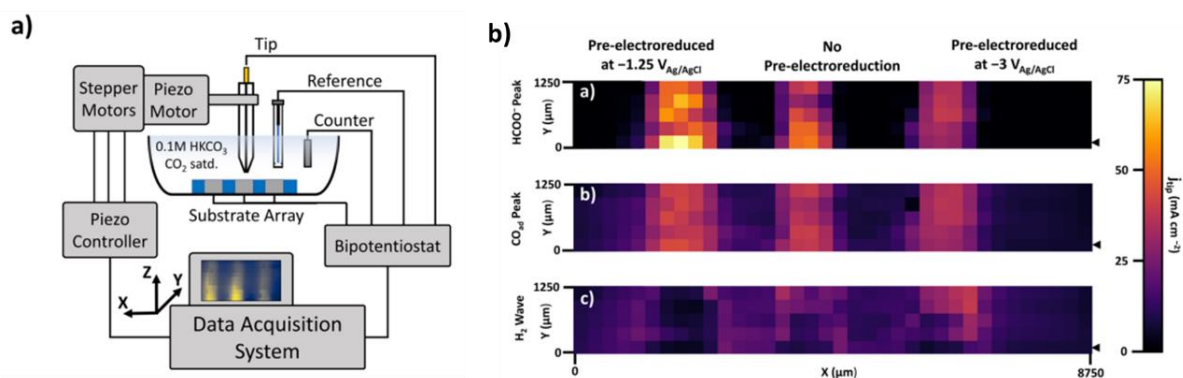


Figure 1.14 a) Scheme of the SECM measurement setup, b) Pt UME tip current densities obtained from the SECM scan attributed to the three products of CO₂ reduction reaction: (a) HCOO⁻, (b) CO_{ad}, (c) H₂. Taken from ref.[100]

In this thesis, we report the development of alternative design strategies for various catalyst materials, including noble metals, metal oxides, and hierarchical zeolites. The selected metal oxide, CeO₂, supported on hierarchical zeolites was systematically studied and applied as promising catalyst for ethanol dehydration to ethylene in *Chapter 3*. Moreover, the combination of noble metal and metal oxide demonstrates the improvement of catalytic activity due to their synergy effect, which is beneficial for selective oxidation of alcohols. *Chapter 4* illustrates the significantly enhanced catalytic performance of Pt-CeO₂ modified hierarchical zeolites because of the synergistic effect. In addition, bipolar electrochemistry was applied to elaborate hybrid Pt-CeO₂ catalyst gradients in *Chapter 5* to find the best combination of these two materials for electrocatalysis. To investigate the electrocatalytic properties of the gradient film generated by bipolar electrodeposition, SECM was used as a local technique. Finally, Janus particles were designed as bifunctional catalysts in order to perform reduction and oxidation reactions simultaneously for the electrochemical conversion of furfural by using bipolar electrochemistry, as described in *Chapter 6*.

Hence, this thesis covers the development of both heterogeneous catalysts and electrocatalysts. It describes their catalytic properties in the frame of the upgrading of biomass-derived compounds, as well as the relationship between material structure and reaction mechanisms for both heterogeneous catalysts and electrocatalysts.

Chapter 2

Scope of Thesis

The development of catalysts for alcohol upgrading processes has received particular attention due to the petroleum shortages and environmental concerns. Therefore, alcohol upgrading can be considered as a clean process to meet human needs. This thesis presents the original design of various catalysts combining metal, metal oxides, and hierarchical structures of solids. They have been successfully elaborated via two different methods, ion exchange and impregnation. Moreover, they have been applied to numerous alcohol upgrading processes, including the dehydration of ethanol and the oxidation of benzyl alcohol, as shown in detail below.

Chapter 3 focuses on the development of catalysts for a sustainable process for the production of ethylene. A metal oxide (CeO_2), supported on hierarchical zeolites via a simple hydrothermal synthesis approach, was investigated to improve the catalyst efficiency for alcohol upgrading. Ethanol is one of the most promising molecules which can offer many beneficial features, such as the lack of toxicity, easy handling, and availability from renewable resources. Various high value-added chemicals, especially ethylene, which is one of the most interesting compounds for plastic production industries, can be produced from ethanol conversion. Over the past decade, catalytic dehydration of ethanol to ethylene was considered as an environmentally friendly process that could be achieved at a lower reaction temperature than traditional ethylene production via thermal cracking of petroleum gas or naphtha. CeO_2 nanoparticles supported on hierarchical zeolite catalysts have been successfully developed by two methods: wet impregnation and ion-exchange methods. Numerous factors, such as the type of support materials, CeO_2 loading methods, CeO_2 content, and Si to Al ratio of the zeolite support, influence the catalytic activity. This was confirmed by many techniques to gain detailed information on the synthesized catalysts that exhibit different properties allowing the optimization of catalytic performance. Interestingly, a higher ethylene yield (~99%) can be achieved

over the modified CeO₂ exchanged hierarchical zeolite prepared by the ion-exchange method. CeO₂ contains mostly Ce^{+IV} in the exchanged conventional zeolite. As a result, this zeolite exhibits an inferior catalytic activity for dehydration of ethanol. However, by increasing the fraction of Ce^{+III} in CeO₂ exchanged hierarchical zeolite, the catalytic performance is enhanced. Moreover, the chemical state of Ce and acidity can be simply adjusted by employing a hierarchical zeolite and using an ion-exchange technique, improving the metal-support interaction, acidity, and Ce reducibility, eventually boosting the dehydration of ethanol to ethylene.

Besides that, CeO₂-based hierarchical zeolite catalysts can be combined with other active sites such as noble metals for other important processes. In *Chapter 4*, the selective oxidation of alcohols to aldehydes, which is important for organic synthesis, from both, an academic and industrial point of view, was systematically studied. Among them, aromatic aldehydes are key intermediates for various fine chemicals; and therefore, their effective production has been widely investigated. Benzaldehyde has various applications ranging from dye production, food and agrochemical issues to perfumery, cosmetics, and pharmaceuticals. As a consequence, the oxidation of benzyl alcohol to benzaldehyde was chosen as a model reaction to study the catalytic performances of Pt supported on hierarchical zeolite catalysts. Owing to cost effectiveness and environmental concerns, molecular oxygen and CeO₂ were used as an oxidant and oxygen carrier in the reaction, respectively. The effect of CeO₂, which could facilitate the lattice mobility of oxygen and play a key role in the catalytic performance of the material, has been systematically investigated. Interestingly, the synergic effect between Pt and CeO₂ can considerably improve the catalytic performances. The benzaldehyde yields reached almost 100 % for Pt supported on CeO₂-hierarchical zeolite, whereas it was less than 40 % with the conventional catalyst. The hierarchical structure of zeolite can: (1) enhance the amount of available active sites due to its unique high surface area, (2) avoid the agglomeration of Pt and CeO₂ nanoparticles, and (3) help to control the oxidation state of CeO₂. The existence of a high fraction of trivalent Ce species (Ce^{+III}) on hierarchical zeolite nanosheets promotes the catalytic oxidation reaction. Furthermore, the tuneable Si to Al ratio of prepared zeolite catalysts can also significantly improve the catalytic performance because of its influence on metal-support interaction and thus Pt size leading to a better catalytic performance.

Apart from the heterogeneous catalysis point of view, electrocatalytic aspects are also essential. In *Chapter 5*, Pt-CeO₂ elaborated by using bipolar electrodeposition was used as an electrocatalyst for benzyl alcohol electro-oxidation. Therefore, this work builds on the previous chapter to explore in more detail the metal-modified electrocatalyst to complement the catalytic perspectives. Thanks to the potential distribution along the bipolar electrode, a Pt-CeO₂ film gradient can be observed. The electrocatalytic properties of the gradient were characterized by scanning electrochemical microscopy (SECM). SECM is a powerful tool for studying the local electrochemical properties of substrates. This technique allows chemical imaging, by using a mobile ultramicroelectrode. SECM imaging is highly dependent on the distance between the tip and the substrate, but also on the local electrochemical properties of the substrate. Hence, SECM can help to elucidate in more detail the role of metal modified electrocatalysts in the catalysis process.

In addition, bipolar electrochemistry was further applied to synthesize a bifunctional electrocatalyst, as discussed in *Chapter 6*. Owing to the asymmetric behavior of conductive materials in a bipolar electrochemical set-up, gradual functionalization of surfaces can be achieved. We illustrate the proof-of-concept that bipolar electrochemistry can produce Janus particles as bifunctional electrocatalysts, which can be used to simultaneously reduce and oxidize a chemical species. Two active species covering the opposite sides of bipolar objects can play a crucial role in converting reactants into the corresponding reduction and oxidation products. Furfural was selected as a model system due to its capability to undergo both types of redox reactions. The investigation demonstrated that Au and Pt layers are suitable to play a crucial role in the catalytic reduction and oxidation reaction of furfural, respectively. Therefore, furfuryl alcohol and furoic acid can be produced simultaneously via a reduction and oxidation of the furfural starting compound. This feature opens up interesting perspectives with respect to the use of Janus particles as bifunctional electrocatalysts.

Chapter 3

Fine-tuning catalytic structures of ceria incorporated in hierarchical zeolites for ethanol dehydration

3.1 Introduction

Ethylene production is one of the most interesting industrial processes due to its utility for several applications, such as surfactant chemicals, plastics, and textiles.[101-103] The thermal cracking of petroleum gas or naphtha is the typical primary process for ethylene production, commonly producing a lot of CO₂ as a by-product.[104, 105] However, the shortages of petroleum resources and serious environmental issues become the limitation for further development of this process. Thus, bioethanol utilization as a renewable feedstock is considered as an alternative way to generate ethylene.[106]

To date, various solid acid catalysts have been developed for ethanol/bioethanol dehydration into ethylene, ranging from mesoporous silica,[12] and alumina,[13] to metal oxides[14] and zeolites.[15] However, their limitations for practical use are the harsh operating conditions and their high acidity. In addition, the fast deactivation of catalysts from coke formation is unavoidable.[107] Among them, one of the most promising catalysts is ZSM-5, Zeolite Socony Mobil-5, an aluminosilicate zeolite belonging to the pentasil family of zeolites, even though its high acidity remains the main concern because it will result in fast catalyst deactivation.[108] There are numerous attempts to overcome this drawback, such as fine-tuning the zeolite acidity depending on its Si/Al ratio and incorporating into hierarchical structures.[109] For instance, the optimal Brønsted acid sites can be finely tuned by changing Si/Al ratios ranging from 16 to 500 to improve the catalytic performances of HZSM-5 assigned as proton exchanged ZSM-5.[15] To decrease the coke formation, a new class of zeolite with hierarchical structures is introduced.[110-112] In such a case, the addition of meso- or macroporous structures into initially

microporous zeolite provides an exceptionally high surface area and tunable porous features.[109, 112]

Up to date, various post-processing concepts have been used to increase the catalytic activity for ethanol dehydration, such as desilication or dealumination, which allow to refine the acidity of the zeolites but also the modification of their hierarchical pore structure.[113] Recently, a high ethylene yield obtained from ethanol/bioethanol dehydration could be achieved with hierarchical HZSM-5 nanosheets having various Si/Al ratios. However, a high ethylene yield cannot be obtained by employing a silica-rich HZSM-5.[114]

Additionally, metal oxides, for instance, cerium oxide (CeO_2), are among the most attractive materials with respect to their active catalytic sites.[18, 115, 116] Currently, CeO_2 catalysts have attracted considerable attention due to their superior properties, such as the redox states of Ce^{3+} and Ce^{4+} , that can be easily shifted from one to the other, an oxygen-storage capacity, high thermal stability, and acid-base properties.[19] The oxygen vacancy sites are also advantageous to be applied in ethanol dehydration. However, since the acidity of CeO_2 is not sufficient to react with the hydroxyl group of ethanol, using pure CeO_2 catalyst itself for ethanol dehydration is not efficient.[117] It is therefore essential to adjust its acidic properties by combining it with additional acid catalysts or other promoters, such as Y/CeO_2 [117], Ce/NaY [118], and $\text{H}_3\text{PW}_{12}\text{O}_{40}/\text{Ce}_{0.8}\text{Zr}_{0.2}\text{O}_2$. [14]

The idea reported in this chapter is to modify the acidity and the chemical state of Ce species by incorporated them in hierarchical zeolites for ethanol dehydration. The combination of Ce species and hierarchical zeolite would be a promising approach due to the above-mentioned distinct properties of Ce species and the capability of hierarchical zeolite to offer a high amount of exposed active sites.[119] Herein, several types of zeolite were employed to investigate their effects on the acidity and chemical state of Ce species, to enhance the catalytic performance for ethanol dehydration. Furthermore, different preparation techniques for Ce insertion, a wet impregnation, and an ion-exchange procedure, were also investigated to better understand the impact of the preparation process on the acidity and chemical state of Ce species.

3.2 Experimental section

3.2.1 Materials

All chemicals with analytical grade were employed as obtained without additional purification. The aluminium and silica sources were aluminium isopropoxide (Sigma-Aldrich, $\geq 98.0\%$) and tetraethyl orthosilicate (TEOS, Sigma-Aldrich, $\geq 99.0\%$), respectively. The mineralizing agent in the preparation process was sodium hydroxide (NaOH, Carlo Erba, $\geq 98.0\%$). Different structure-directing agents (SDAs) were used for conventional zeolites and hierarchical zeolite synthesis. Tetrapropylammonium hydroxide (TPAOH, 1.0 M in H_2O) was employed as an SDA for conventional zeolite, while tetrabutylphosphonium hydroxide (TBPOH, Sigma-Aldrich, 40% in H_2O) was used for hierarchical zeolites. Moreover, cerium (III) acetate (TCI, $>98.0\%$) was used as a cerium precursor. Besides, ethyl alcohol (Sigma-Aldrich, $\geq 99.0\%$) was used as a reactant to study the catalytic activity.

3.2.2 Catalyst preparation

Catalysts were prepared based on zeolite support materials including conventional zeolite and hierarchical zeolite. The distinctive features of structure-directing agents (SDA) were used to construct different zeolite supports.[120]

3.2.2.1 Synthesis of conventional ZSM-5 zeolite (ZSM5-CON)

The conventional ZSM-5 zeolite was typically synthesized according to the molar synthesis composition of $10\text{SiO}_2: 0.05\text{Al}_2\text{O}_3: 1\text{TPAOH}: 1.03\text{NaOH}: 400\text{H}_2\text{O}$. After mixing 7 g of TEOS and 3.42 g of TPAOH to obtain a silica-SDA solution, 0.14 g of sodium hydroxide, dissolved in DI water, was added gently into the silica-SDA solution, and the mixture was stirred at room temperature for 2 hours. After that, the obtained gel was transferred to the hydrothermal synthesis reactor and heated to $180\text{ }^\circ\text{C}$ for 3 days. Then, the prepared sample was washed with DI water, filtered, and dried at $110\text{ }^\circ\text{C}$. Finally, the calcination process was carried out at $650\text{ }^\circ\text{C}$ for 6 hours to remove SDA and get the final product, namely ZSM5-CON, as illustrated in Figure 3.1.

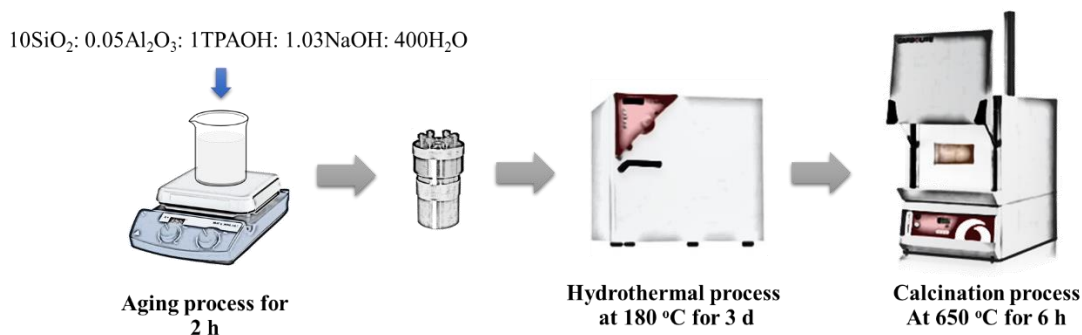


Figure 3.1 Schematic illustration of conventional ZSM-5 preparation.

3.2.2.2 Synthesis of hierarchical Silicalite-1 (Silicalite1-HIE) and ZSM-5 zeolites (ZSM5-HIE)

Hierarchical Silicalite-1 and ZSM-5 with different Si/Al ratios were synthesized with the molar composition of $60\text{SiO}_2: x\text{Al}_2\text{O}_3: 18\text{TBPOH}: 0.75\text{NaOH}: 600\text{H}_2\text{O}$, where x was 0 and 0.3, denoted as Silicalite1-HIE and ZSM5-HIE, respectively. Initially, TEOS and aluminium isopropoxide were mixed as a silica-alumina solution. Another solution containing 8.62 g of TBPOH, 0.02 g of sodium hydroxide dissolved in DI-water was gently added into the silica-alumina solution, followed by stirring at room temperature for 12 hours. After that, the obtained gel was put in the hydrothermal synthesis reactor and heated to 130 °C for 2 days. Then, the prepared sample was washed with DI water, filtered, and dried at 110 °C. Finally, the calcination process was carried out at 650 °C for 6 hours to remove SDA and get the final product, namely Silicalite1-HIE and ZSM5-HIE zeolite. Similar synthesis sequence is shown in Figure 3.1.

After zeolite preparation, CeO_2 was loaded in the next step. Two methods were selected to load CeO_2 nanoparticles on zeolite supports, including ion-exchange and wet impregnation methods. The impregnation method consists of three basic steps: first, support with high surface area is impregnated with a solution containing the metal precursors, then the solvent is evaporated at an elevated temperature, and finally, the metal precursors are reduced under designated environment to produce the catalysts.[121] The ion exchange method uses the ion exchange features of the support materials that can have binding preferences for certain ions, depending on the physical properties and chemical structure of both the ion exchanger and the ion. It depends on the size, charge, or structure of the ions.

Typically, impregnation leads to a rather weak metal-support interaction, leading to large metal particles, whereas ion exchange results in a higher initial dispersion.[122]

3.2.2.3 Preparation of ceria supported on zeolites using ion-exchange method (Exc)

The prepared zeolites were used as solid supports for the cerium species. The mixture of a zeolite and the desired amount of cerium (III) acetate was prepared using DI water as solvent at 80 °C for 2 hours. Subsequently, the mixture was filtered, washed with DI water, and finally dried at 100 °C overnight. Finally, the calcination process was carried out at 550 °C for 4 hours to get a catalyst corresponding to yCe(Exc)-ZSM5-HIE, and yCe(Exc)-ZSM5-CON for the hierarchical ZSM-5 and the conventional ZSM-5, respectively (y = 0, 1, 5, 10 and 20 wt% of CeO₂).

3.2.2.4 Preparation of ceria supported on zeolites using impregnation method (Imp)

The prepared zeolites were combined with the desired cerium (III) acetate content and DI-water at room temperature for 24 hours using an impregnation method. Subsequently, the solvent was removed by a rotary evaporator, and the acquired materials were finally dried at 100 °C overnight. Then, the calcination process was carried out at 550 °C for 4 hours to obtain the catalysts, denoted as yCe(Imp)-Silicalite1-HIE, yCe(Imp)-ZSM5-HIE for the hierarchical silicalite-1, and the hierarchical ZSM-5, respectively (y = 5 wt% of CeO₂).

It should be noted that all samples are denoted as yCe(M)-zeolite support, where y is the CeO₂ content. M refers to the preparation method (Exc = ion-exchange method; Imp = impregnation method).

3.2.3 Characterization

The powder X-ray diffraction (XRD) patterns of the synthesized catalysts were studied with a Bruker D8 ADVANCE device with CuK α radiation (40 kV, 40 mA) in the 2 θ ranging from 5° to 60° with a step size of 0.02° and a scan rate of 1° min⁻¹. Scanning electron microscopy (SEM) images and transmission electron microscopy (TEM) images to study the morphology of the catalysts were recorded with a JEOL JSM-7610F microscope and JEOL JEM-ARM200F microscope at 200 kV, respectively. N₂ adsorption-desorption measurement was used to determine the

textural properties of all the prepared catalysts at $-196\text{ }^{\circ}\text{C}$ by using a MicrotracBEL, BELSORP-max model, and all samples were degassed at $350\text{ }^{\circ}\text{C}$ for 24 hours prior to the investigation. The specific surface area (S_{BET}), micropore surface area, and pore volume were evaluated by the Brunauer–Emmett–Teller (BET) and t -plot methods, respectively. Moreover, wavelength-dispersive X-ray fluorescence spectroscopy (WDXRF) recorded with a Bruker S8 TIGER ECO machine. Scanning electron microscopy coupled with energy dispersive X-ray spectroscopy (SEM-EDS) acquired with a JEOL JSM-7610F microscope were used to analyze the elemental composition. In addition, the surface properties were investigated, including acidity, performed by NH_3 temperature-programmed desorption (NH_3 -TPD), basicity, performed by CO_2 temperature-programmed desorption (CO_2 -TPD), and metal reducibility performed by H_2 temperature-programmed reduction (H_2 -TPR). The measurements were conducted using a BELCAT II instrument equipped with thermal conductivity detectors (TCD). Prior to the NH_3 -TPD and CO_2 -TPD measurements, 0.05 g of the sample was pretreated typically at $300\text{ }^{\circ}\text{C}$ for 1 hour under He flow to entirely eliminate the adsorbed molecules on the sample surface, and then it was cooled down to $100\text{ }^{\circ}\text{C}$, together with supplying saturated NH_3 gas (5 vol% in He) or CO_2 gas for 30 min (50 mL min^{-1}), followed by He flushing (50 mL min^{-1}) for 30 min at $100\text{ }^{\circ}\text{C}$. The desorption steps of both NH_3 and CO_2 were recorded in the temperature range from 100 to $800\text{ }^{\circ}\text{C}$ with a heating rate of $10\text{ }^{\circ}\text{C}\cdot\text{min}^{-1}$. In the case of H_2 -TPR, the samples were pretreated typically at $300\text{ }^{\circ}\text{C}$ for 1 hour with a heating rate of $10\text{ }^{\circ}\text{C min}^{-1}$ under Ar flow and then cooled down to $50\text{ }^{\circ}\text{C}$. Subsequently, the measurement was performed from $50\text{ }^{\circ}\text{C}$ to $900\text{ }^{\circ}\text{C}$ with a heating rate of $5^{\circ}\text{C min}^{-1}$ in a flow of 2 v/v% of H_2 in Ar (50 mL min^{-1}). Besides, the Ce oxidation state was carefully characterized using X-ray absorption near-edge structure (XANES). All samples were pretreated typically at $350\text{ }^{\circ}\text{C}$ for 2 hours under a N_2 flow to remove adsorbed molecules on the samples. Ce L3-edge XANES spectra were obtained in transmission mode at the BL5.2 station at Siam Photon Laboratory (Synchrotron Light Research Institute (Public Organization), SLRI), Thailand.

3.2.4 Catalytic activity test

A fixed-bed reactor was used to study the catalytic performance for ethanol dehydration. Initially, 0.1 g of the catalyst was pretreated at $350\text{ }^{\circ}\text{C}$ under a N_2 flow of 5 mL min^{-1} for 2 hours. Then, the reaction was performed under N_2 flow at 350

°C with a controlled weight of ethanol feed flowing per unit weight of catalyst per hour, called weight hourly space velocity (WHSV_{EtOH}), equal to 5 h⁻¹. The quantification of products was investigated by a gas chromatograph (GC, Agilent 7890B) equipped with a flame ionization detector (FID) and a PoraBOND Q capillary column (25 m x 0.32 mm) at a time interval of 1 hour. Subsequently, the conversion of ethanol (X_{EtOH}) and the product selectivity (S_i) were estimated by the following equations:

$$X_{EtOH} = \left(\frac{(n_{EtOH})_0 - (n_{EtOH})_t}{(n_{EtOH})_0} \right) \times 100\%$$

$$S_i = \left(\frac{n_i}{(\sum n)_t} \right)$$

Where (n_{EtOH})₀, (n_{EtOH})_t, n_i, Σn are the initial mole content of ethanol, the ethanol mole content at a particular time, the mole content of the desired product i, and the total moles of all the products, respectively.

3.3 Results and discussion

The scheme of Figure 3.2 illustrates the preparation process of several zeolites involving hierarchical ZSM-5 (ZSM5-HIE), hierarchical silicalite-1 (Silicalite1-HIE), and conventional ZSM-5 (ZSM5-CON). The variation of Ce species (I, II, III, and IV) could be found due to the various solid supports and the different insertion procedures, including simple impregnation (Imp) and ion-exchange techniques (Exc).

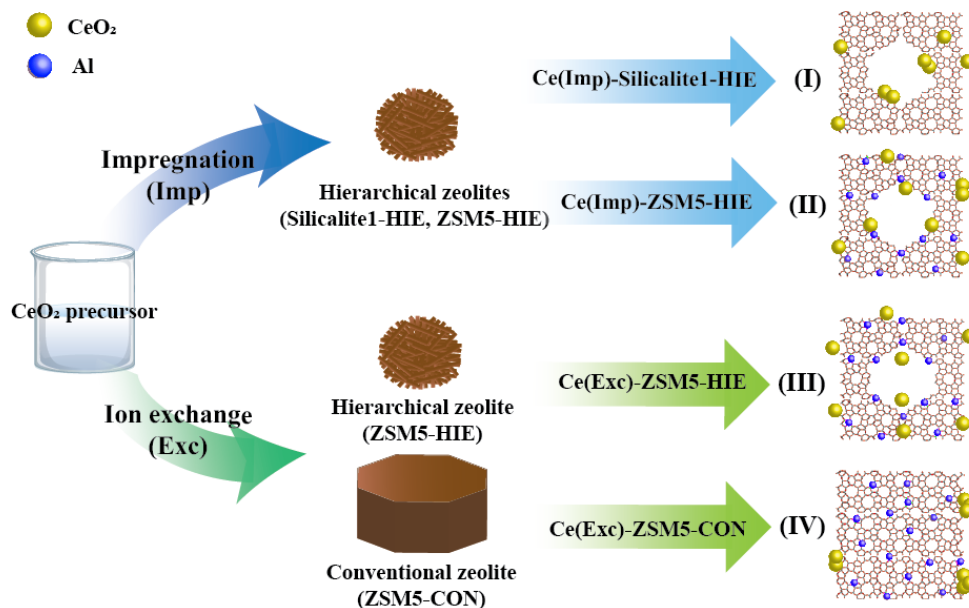


Figure 3.2 Schematic illustration of fine-tuned CeO_2 preparation using different support materials including conventional ZSM-5 (ZSM5-CON), hierarchical ZSM-5 (ZSM5-HIE), and hierarchical silicalite-1 (Silicalite1-HIE); I, II, III, and IV denoted as Ce(Imp)-Silicalite1, Ce(Imp)-ZSM5-HIE, Ce(Exc)-ZSM5-HIE, and Ce(Exc)-ZSM5-CON, respectively.

The crystalline structure is corroborated by XRD results for all the synthesized catalysts, as shown in Figure 3.3. The XRD patterns (Figure 3.4A) and the relative crystallinity (Table 3.1) demonstrate that CeO_2 insertion does not destroy the MFI crystalline structure of ZSM-5, which belongs to the pentasil family of zeolites as compared to pristine ZSM5-HIE. Because the content of Ce species is quite high (5 wt.% obtained from XRF measurement), the characteristic peaks of CeO_2 at 2θ of 28, 33, 48, and 56 degrees[123] can be clearly seen, especially at 28 degrees (Figure 3.4A(d)). In contrast, the corresponding peaks are invisible in the XRD patterns of prepared hierarchical zeolites, even when using the same CeO_2 content, suggesting that well-dispersed Ce species can be obtained on hierarchical zeolite surfaces.

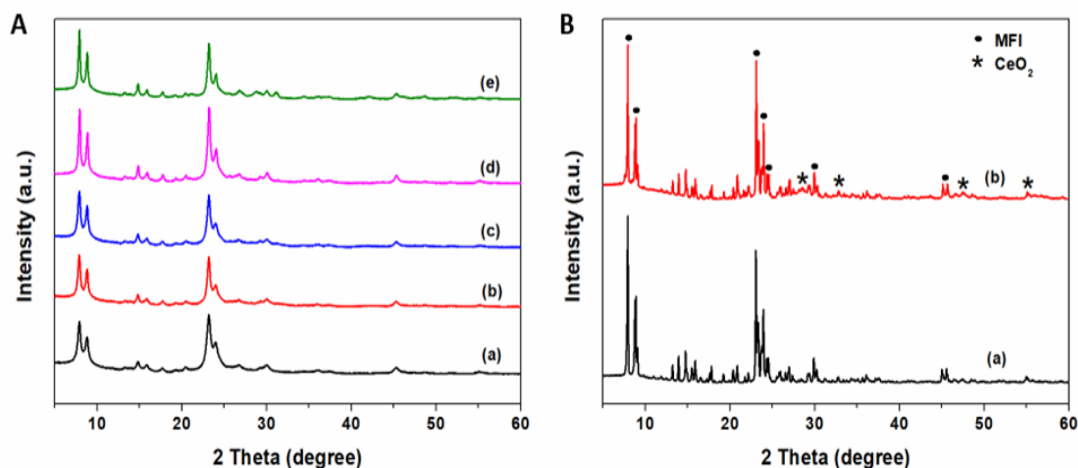


Figure 3.3 XRD results of (A) hierarchical zeolite supports: (a) ZSM5-HIE, (b) 5Ce(Imp)-ZSM5-HIE, (c) 5Ce(Exc)-ZSM5-HIE, (d) Silicalite1-HIE, and (e) 5Ce(Imp)-Silicalite1-HIE, and (B) conventional zeolite supports: (a) ZSM5-CON and (b) 5Ce(Exc)-ZSM5-CON.

The X-ray absorption near edge structure (XANES) indicates the Ce oxidation states of the synthesized catalysts. Generally, CeO₂ nanoparticles have a cubic fluorite structure with a mixed-valence state between Ce⁴⁺ and Ce³⁺.^[124] A major contribution of the Ce³⁺ state can be observed for 5Ce(Imp)-Silicalite1-HIE, 5Ce(Imp)-ZSM5-HIE, and 5Ce(Exc)-ZSM5-HIE samples, while the Ce⁴⁺ state is predominant in a conventional zeolite (5Ce(Exc)-ZSM5-CON) as can be seen in Figure 3.4B. These observations imply that the well-dispersed ultra-small Ce particles typically contain a high fraction of Ce³⁺.^[125] Hence, it is reasonable to conclude that the hierarchical zeolite surfaces can provide highly dispersed Ce species.

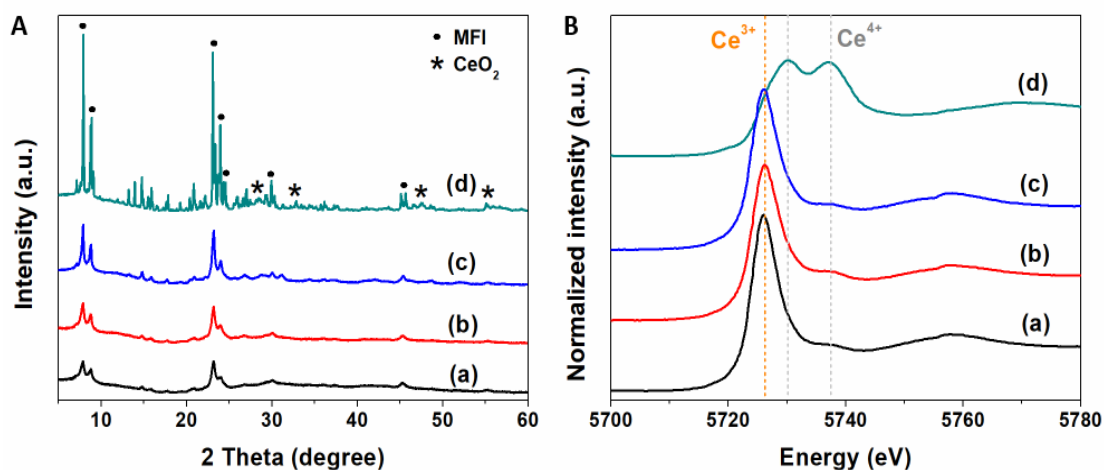


Figure 3.4 (A) XRD results and (B) Normalized Ce L3 edge XANES spectra of (a) 5Ce(Exc)-ZSM5-HIE, (b) 5Ce(Imp)-ZSM5-HIE, (c) 5Ce(Imp)-Silicalite1-HIE and (d) 5Ce(Exc)-ZSM5-CON.

Table 3.1 Relative crystallinity of the prepared catalysts.

Tag	Catalyst	Relative crystallinity (%) [*]
A-(a)	ZSM5-HIE	100.0
A-(b)	5Ce(Imp)-ZSM5-HIE	91.2
A-(c)	5Ce(Exc)-ZSM5-HIE	95.4
A-(d)	Silicalite1-HIE	100.0
A-(e)	5Ce(Imp)-Silicalite1-HIE	95.2
B-(a)	ZSM5-CON	100.0
B-(b)	5Ce(Exc)-ZSM5-CON	87.2

The relative crystallinity of CeO₂ modified catalysts before and after CeO₂ modification was calculated by using the integrated data of the three most intense peaks at 2θ of 7.8°, 8.9° and 23.2° from XRD measurement. The sample before modification was used as the reference to calculate the relative crystallinity of the samples in each case.

Moreover, TEM images confirm the morphology of the synthesized hierarchical zeolite with MFI zeolite nanosheet assemblies (Figure 3.5).

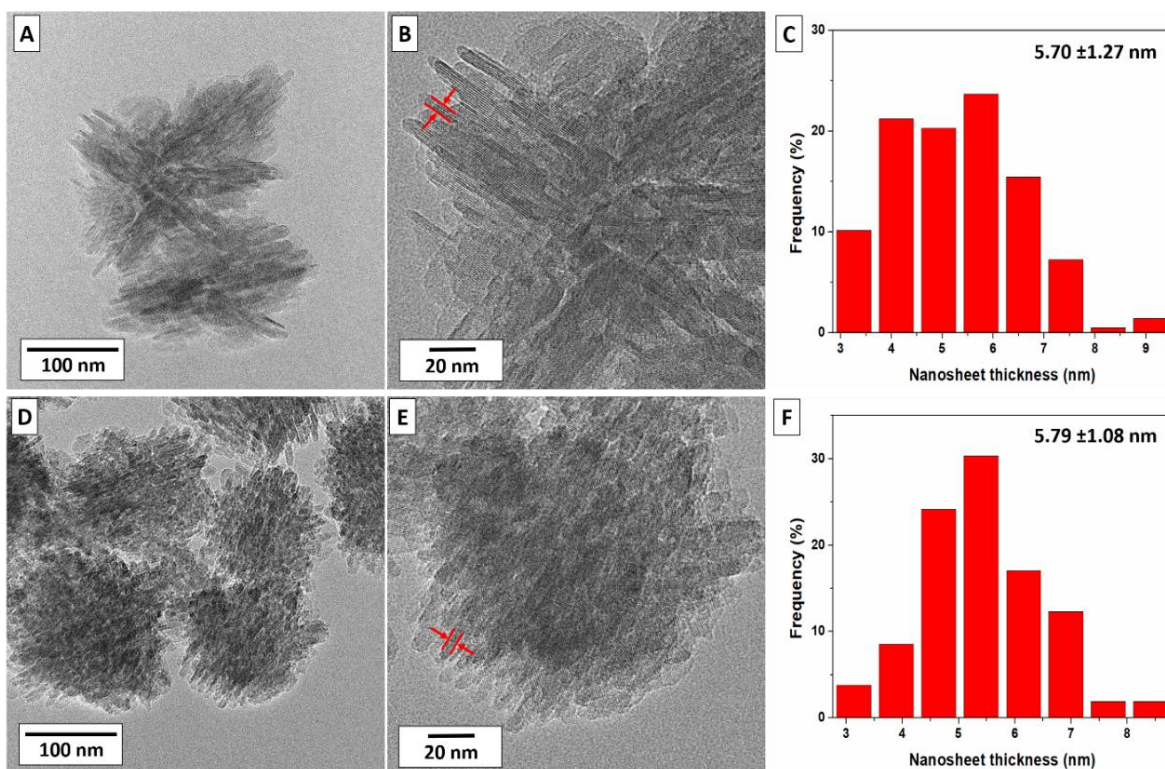


Figure 3.5 TEM images and nanosheet thickness distribution of (A-C) Silicalite1-HIE and (D-F) ZSM5- HIE.

In addition, the hierarchical zeolites clearly demonstrate the higher surface roughness with respect to the conventional one (Figure 3.6). The average particle sizes are around $3.17 \mu\text{m}$, 233 nm , 157 nm , and 154 nm for 5Ce(Exc)-ZSM5-CON, 5Ce(Imp)-Silicalite1-HIE, 5Ce(Imp)-ZSM5-HIE, and 5Ce(Exc)-ZSM5-HIE, respectively. This again confirms that the CeO_2 loading doesn't influence the structure, morphology, and size of the zeolite supports.

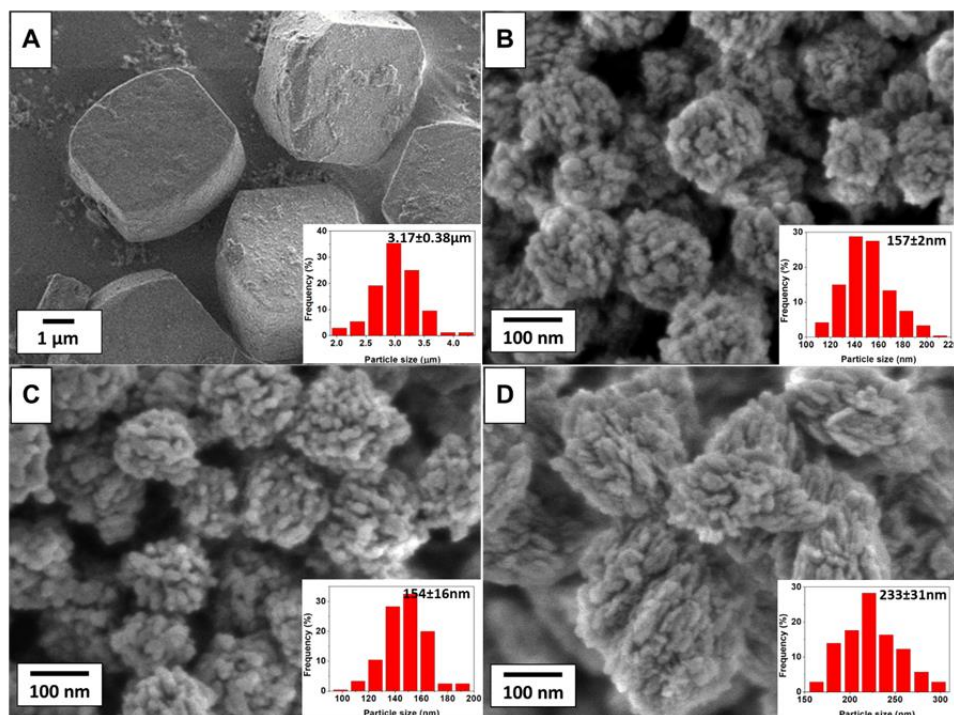


Figure 3.6 SEM images and zeolite particle size distribution of (A) 5Ce(Exc)-ZSM5-CON, (B) 5Ce(Exc)-ZSM5-HIE, (C) 5Ce(Imp)-ZSM5-HIE and (D) 5Ce(Imp)-Silicalite1-HIE.

Moreover, more detailed information about the Ce species dispersion was obtained by scanning electron microscopy (SEM) equipped with the low-angle backscattered electron detector (LABE), as shown in Figure 3.7. This method collects backscattered electrons released at lower angles from the surface of the material. Typically, because the backscattered electrons are proportional to the atomic number of elements, heavy elements appear brighter compared to lighter elements, providing higher sensitivity to changes in the surface structure.[126] Thus, LABE tomography can deliver qualitative compositional data via Z-contrast of nanoparticles owing to the difference of electron scattering properties between Ce species and zeolites.[127] As can be seen in Figure 3.7, bright spots refer to the position of Ce species, while the darker background reveals the zeolite part. Noticeably, the big bright spots assigned to CeO₂ are easily seen for the 5Ce(Exc)-ZSM5-CON, while hierarchical zeolites offer well-dispersed metal oxide species, especially when they are synthesized using an ion-exchange method (5Ce(Exc)-ZSM5-HIE). It reveals that both the insertion procedure and the support materials strongly influence the dispersion of Ce species.

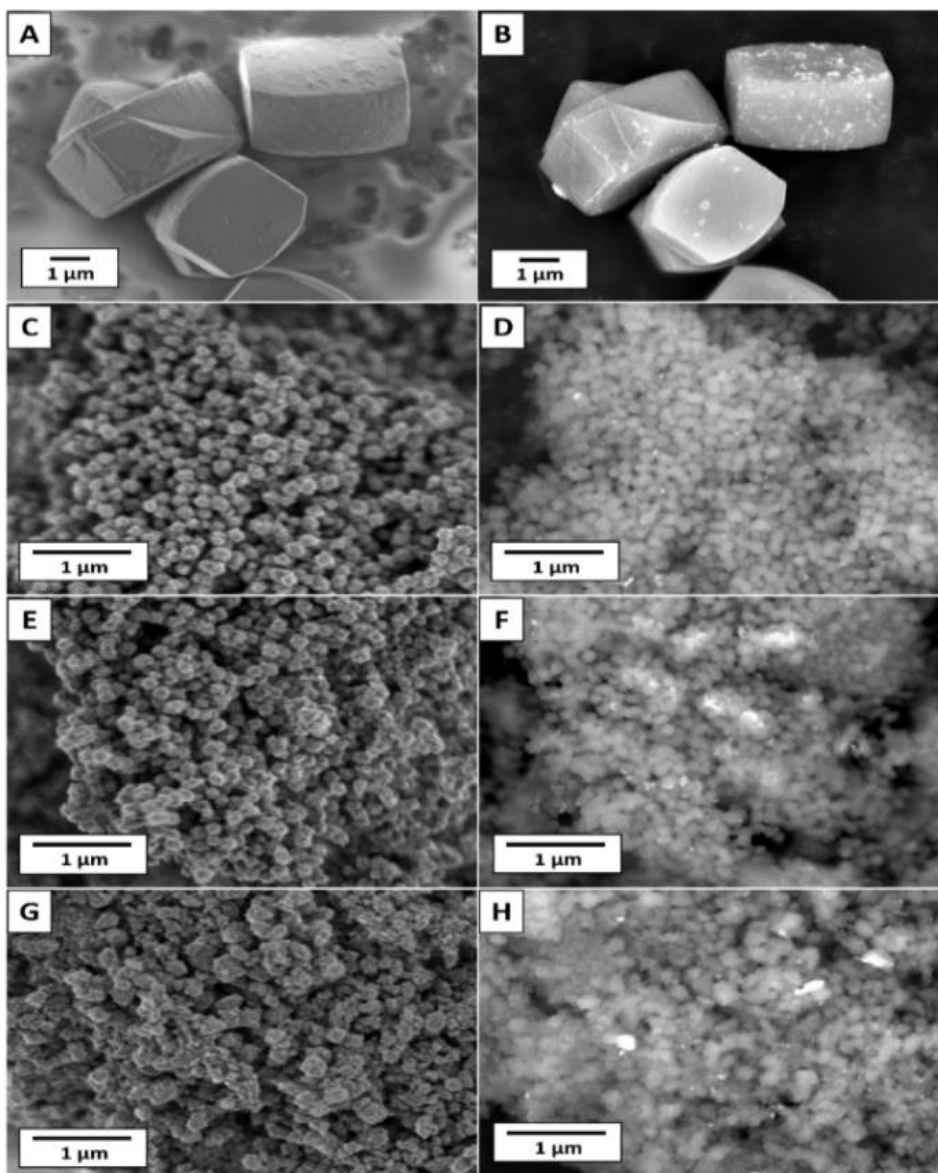


Figure 3.7 SEM images of (A,B) 5Ce(Exc)-ZSM5-CON, (C,D) 5Ce(Exc)-ZSM5-HIE, (E,F) 5Ce(Imp)-ZSM5-HIE and (G,H) 5Ce(Imp)-Silicalite1-HIE employing a secondary electron detector (SE mode, left) and a low-angle backscattered electron detector (LABE mode, right), respectively.

Moreover, further information of CeO_2 dispersion at higher magnification was explored by transmission electron microscopy (TEM), as can be seen in Figure 3.8. These observations again prove that the smallest Ce species can be obtained with 5Ce(Exc)-ZSM5-HIE.

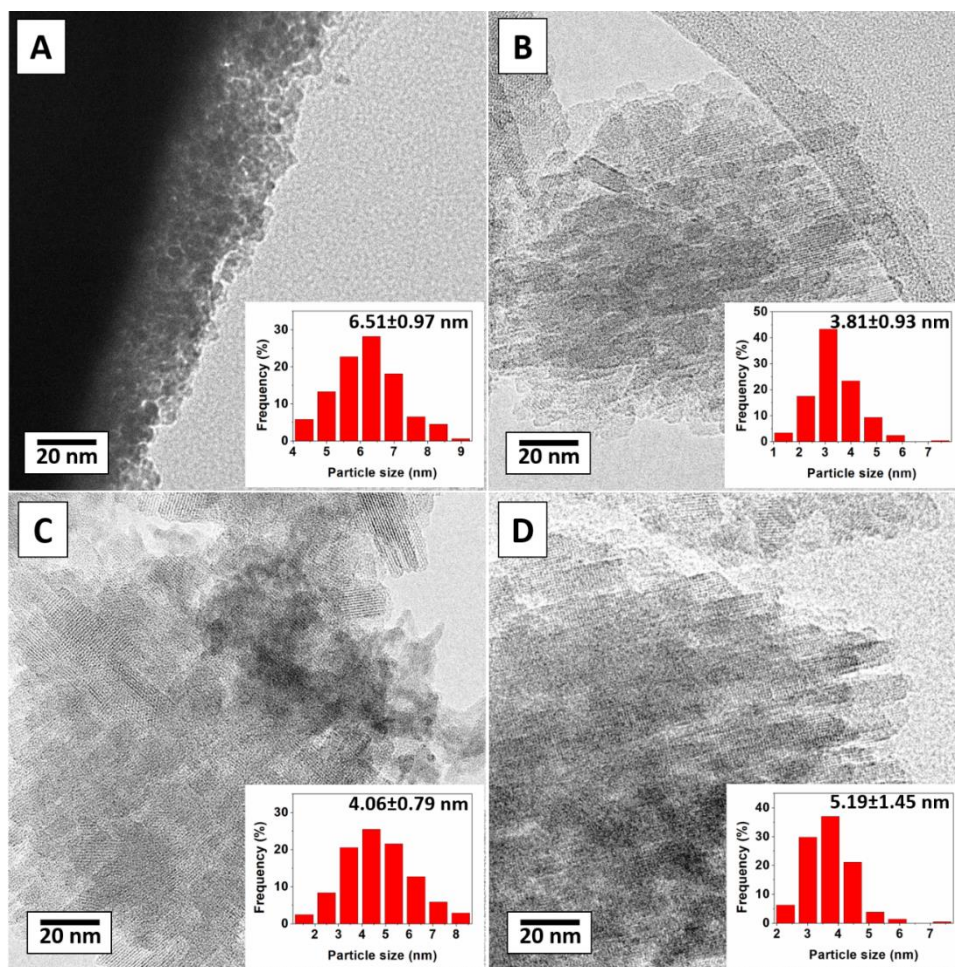


Figure 3.8 TEM images and CeO_x particle size distribution of (A) 5Ce(Exc)-ZSM5-CON, (B) 5Ce(Exc)-ZSM5-HIE. (C) 5Ce(Imp)-ZSM5-HIE, and (D) 5Ce(Imp)-Silicalite1-HIE.

Energy-dispersive X-ray spectroscopy (EDS) in scanning transmission electron microscopy (STEM) allows to perform the chemical mapping illustrated in Figure 3.9. In the case of a conventional support, CeO₂ nanoparticles can be clearly observed on the outer surface of ZSM5-CON, whereas a better CeO₂ dispersion can be seen with hierarchical zeolites. The brighter spots compared to the zeolite background of the hierarchical structure can be assigned to Ce, which is a heavier element than the components of zeolites. The elemental analysis by SEM-EDS is illustrated in Figure 3.10 and detailed in Table 3.2. The elemental mappings and the variation of the Ce to Si ratio again indicate a superior distribution of Ce modified hierarchical ZSM-5 obtained by the Ce-ion-exchange process.

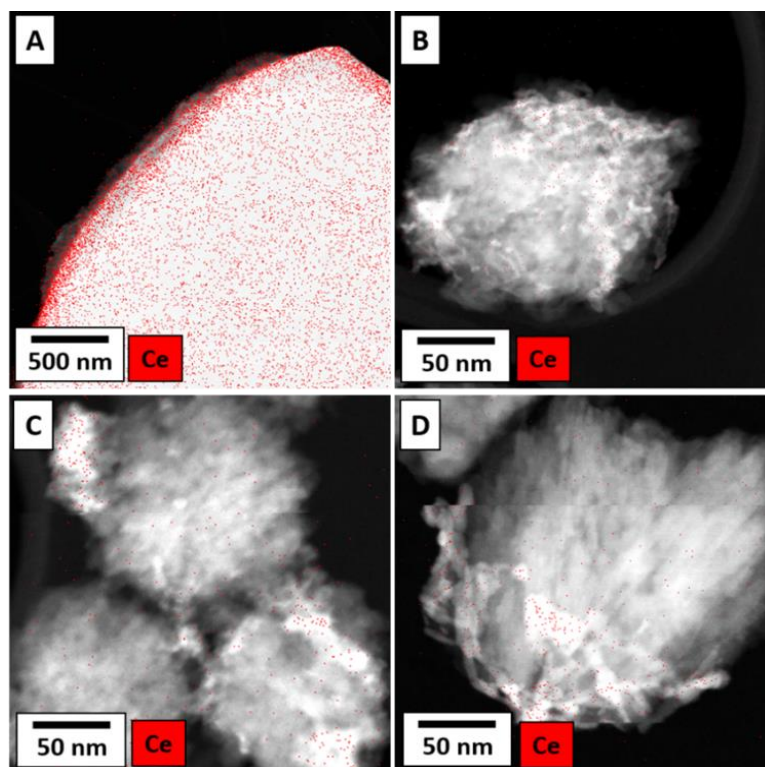


Figure 3.9 STEM-EDS images of (A) 5Ce(Exc)-ZSM5-CON, (B) 5Ce(Exc)-ZSM5-HIE, (C) 5Ce(Imp)-ZSM5-HIE and (D) 5Ce(Imp)-Silicalite1-HIE.

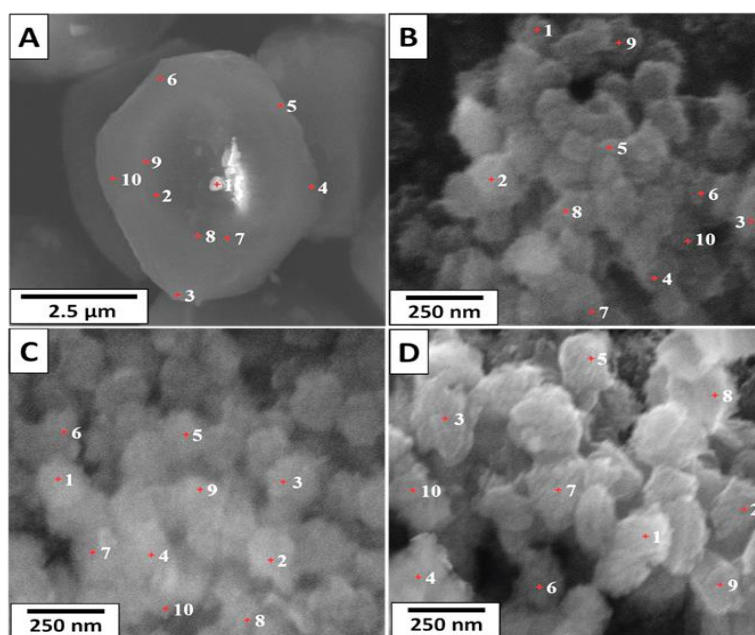


Figure 3.10 SEM-EDS elemental points analysis of (A) 5Ce(Exc)-ZSM5-CON, (B) 5Ce(Exc)-ZSM5-HIE, (C) 5Ce(Imp)-ZSM5-HIE and (D) 5Ce(Imp)-Silicalite1-HIE.

Table 3.2 Elemental points analysis data

Point	Ce/Si ratio			
	5Ce(Exc)-ZSM5-HIE	5Ce(Exc)-ZSM5-CON	5Ce(Imp)-Silicalite1-HIE	5Ce(Imp)-ZSM5-HIE
1	1.24	7.18	8.59	6.57
2	1.39	10.39	8.65	8.56
3	1.05	22.70	8.16	5.99
4	1.67	7.45	8.46	7.74
5	1.11	13.58	4.77	5.90
6	0.78	16.02	7.93	5.76
7	0.89	14.69	9.76	6.48
8	1.80	10.87	9.02	8.91
9	0.78	15.20	7.12	8.86
10	1.45	24.56	9.05	7.83
Average	1.22 ±0.36	14.26 ±5.82	8.15 ±1.39	7.26 ±1.26

The textural properties of the prepared catalysts were studied using N₂ physisorption measurements. Conventional zeolite normally reveals a type I isotherm, indicating that it possesses only a microporous structure, as can be seen in the case of 5Ce(Exc)-ZSM5-CON (Figure 3.11 and Table 3.3).[128] In contrast, mixed isotherms between type I due to the micropore filling at the low relative pressure and type IV isotherm because of the high N₂ uptake and mesopore capillary condensation at the relative pressure of 0.4 to 0.8 can be found for the hierarchical zeolites.[129] This confirms that hierarchical zeolites can provide a superior surface area, enhanced metal distribution, eventually improving the catalytic activity.

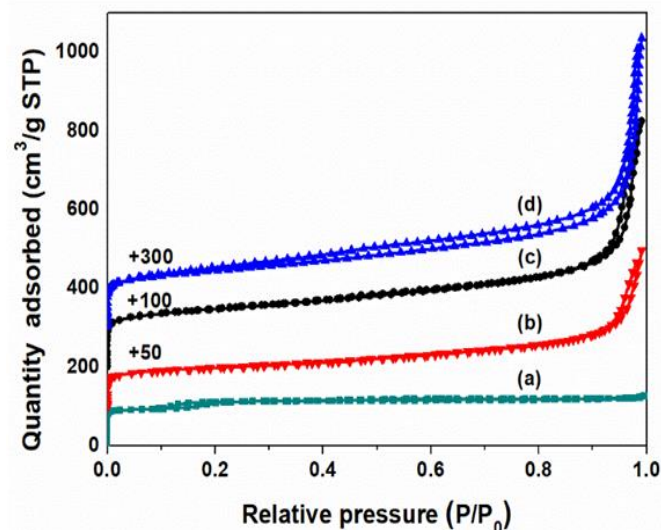


Figure 3.11 N₂ adsorption/desorption isotherms of (a) 5Ce(Exc)-ZSM5-CON, (b) 5Ce(Imp)-ZSM5-HIE, (c) 5Ce(Exc)-ZSM5-HIE, and (d) 5Ce(Imp)-Silicalite1-HIE.

Table 3.3 Textural properties of all the prepared catalysts

Catalysts	Si/Al ^a	S _{BET} ^b (m ² g ⁻¹)	S _{ext} ^c (m ² g ⁻¹)	S _{micro} ^d (m ² g ⁻¹)	V _{total} ^e (cm ³ g ⁻¹)	V _{micro} ^f (cm ³ g ⁻¹)	V _{ext} ^g (cm ³ g ⁻¹)
5Ce(Exc)-ZSM5-HIE	60.7	464	206	258	0.956	0.147	0.809
5Ce(Exc)-ZSM5-CON	97.6	383	5	378	0.191	0.177	0.014
5Ce(Imp)-ZSM5-HIE	58.4	356	139	217	0.604	0.104	0.500
5Ce(Imp)-Silicalite1-HIE	∞	475	196	279	0.877	0.112	0.765

^a Si/Al determined by wavelength dispersive x-ray fluorescence.

^b S_{BET}: Specific surface area (m²g⁻¹) determined by BET method.

^c S_{ext}: External surface area (m²g⁻¹).

^d S_{micro}: micropore surface area (m²g⁻¹), determined by t-plot method.

^e V_{total}: total pore volume (cm³g⁻¹) obtained at P/P₀=0.99.

^f V_{micro}: micropore volume (cm³g⁻¹), determined by t-plot method.

^g V_{ext}: external pore volume (cm³g⁻¹), V_{ext}=V_{total}-V_{micro}.

From the additional investigation of the surface properties of the prepared catalysts, as shown in Figure 3.12A, it can be seen that the type of support materials and modification methods to load CeO_2 can impact the acid properties, including overall acidity and the acid strength compared to pristine ZSM5-HIE (Figure 3.13). Two noticeable peaks at low (200°C) and high temperatures (400°C), assigned to weak and strong acid sites, respectively,[130] can be observed from the NH_3 temperature-programmed desorption (TPD) profiles for the 5Ce(Exc)-ZSM5-HIE sample. In contrast, other catalysts, including commercial CeO_2 nanoparticles, indicate lower acidity, as summarized in Table 3.4. It should be noticed that all the prepared catalysts were synthesized without a proton ion-exchange process. It is therefore reasonable to assume that acid sites could be the result of Ce species modification. Moreover, CO_2 TPD profiles of the prepared catalysts can indicate the basic properties, revealing three desorption peaks related to weak, moderate, and strong basic sites at a temperature of 200, 450, and 650°C, respectively (Figure 3.12B). Remarkably, the total basicity of hierarchical samples is stronger than for commercial CeO_2 and a modified conventional zeolite, implying the more considerable number of CeO_2 defect sites on hierarchical zeolite (Table 3.5).[131]

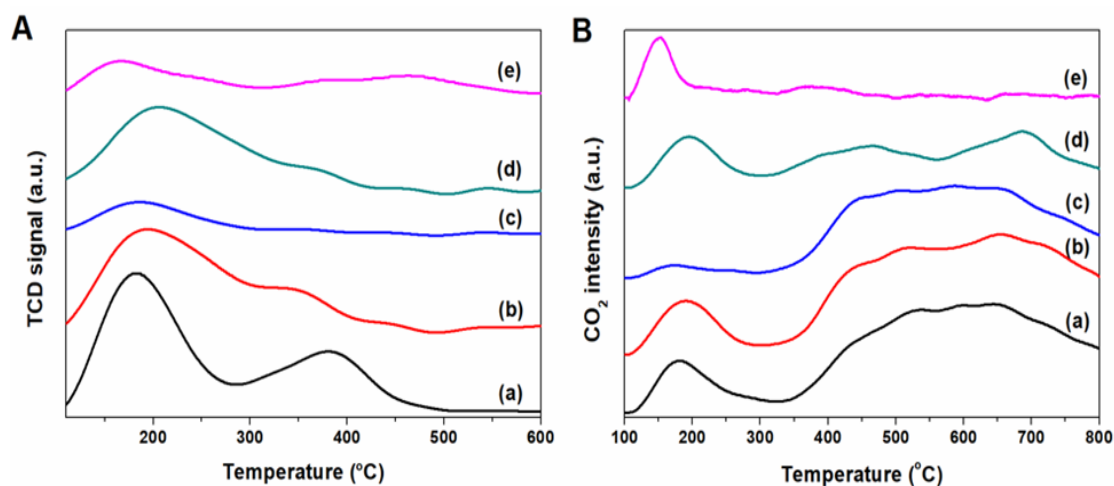


Figure 3.12 Chemisorption profiles of (A) NH_3 TPD and (B) CO_2 TPD for (a) 5Ce(Exc)-ZSM5-HIE, (b) 5Ce(Imp)-ZSM5-HIE, (c) 5Ce(Imp)-Silicalite1-HIE, (d) 5Ce(Exc)-ZSM5-CON, and (e) commercial CeO_2 nanoparticles.

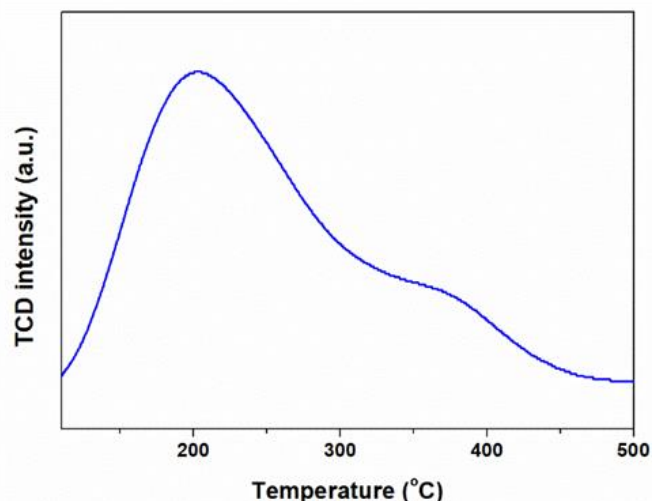


Figure 3.13 Chemisorption profile of NH₃ TPD for ZSM5-HIE.

Table 3.4 Acid density of all the prepared catalysts obtained from NH₃-TPD measurement.

Catalysts	Acidity amount ($\mu\text{mol g}^{-1}$)		Total acid density ($\mu\text{mol g}^{-1}$)
	Weak (180-200°C)	Strong (350-400°C)	
ZSM5-HIE	79	34	113
5Ce(Imp)-ZSM5-HIE	73	39	112
5Ce(Imp)-Silicalite1-HIE	24	4	28
5Ce(Exc)-ZSM5-HIE	95	57	152
5Ce(Exc)-ZSM5-CON	71	21	92
CeO ₂	23	12	45

Table 3.5 Basic density of all the prepared catalysts obtained from CO₂-TPD measurement.

Catalysts	Basicity amount ($\mu\text{mol g}^{-1}$)			Total basic density ($\mu\text{mol g}^{-1}$)
	Weak (150-200°C)	Moderate (450-500°C)	Strong (600-700°C)	
5Ce(Imp)-ZSM5-HIE	37	101	247	385
5Ce(Imp)-Silicalite1-HIE	8	95	171	273
5Ce(Exc)-ZSM5-HIE	35	146	169	350
5Ce(Exc)-ZSM5-CON	33	60	77	170
CeO ₂	21	19	2	42

Besides, H₂-TPR profiles of the prepared catalysts were recorded to evaluate the reducibility of the catalysts (Figure 3.14 and Table 3.6). Generally, two characteristic Ce peaks at 500 and 850°C are detected related to the reduction of Ce⁴⁺ to Ce³⁺ with surface oxygen and bulk oxygen, respectively,[132] as can also be seen in the profile of commercial CeO₂. [133] Interestingly, hierarchical catalysts offer a lower Ce reduction temperature, indicating the formation of ultra-small Ce particles, eventually leading to enhanced reducibility. These observations again verify that by using the hierarchical zeolite supports, higher surface/lattice oxygen mobility can be obtained.[134] Normally, smaller particle sizes and higher surface areas of CeO₂ materials are likely to have more crystal edges and corners, resulting in a greater density of surface oxygen species allowing using lower temperatures for reduction processes to occur.[135] The most appropriate performance among these prepared catalysts is 5Ce(Exc)-ZSM5-HIE due to its active surface oxygen, which should be advantageous for the catalytic performance.

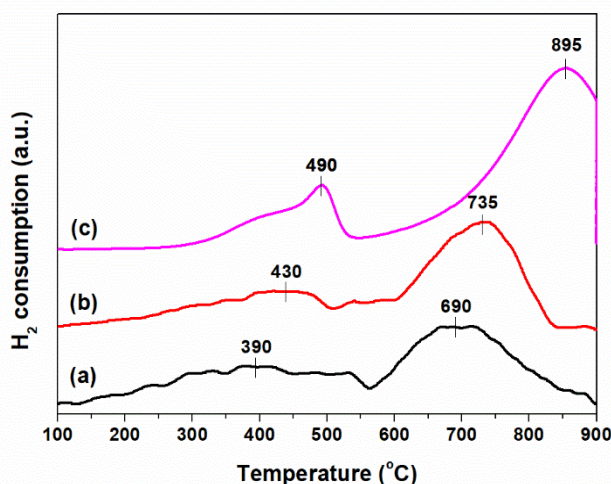


Figure 3.14 Chemisorption profiles of H₂ TPR for (a) 5Ce(Exc)-ZSM5-HIE, (b) 5Ce(Imp)-ZSM5-HIE and (c) commercial CeO₂ nanoparticles.

Table 3.6 Reducibility of all the prepared catalysts obtained by using H₂-TPR measurement.

Catalysts	H ₂ consumption (mmol g ⁻¹)		Total H ₂ consumption (mmol g ⁻¹)
	Surface oxygen	bulk	
5Ce(Imp)-ZSM5-HIE	0.002	0.003	0.005
5Ce(Exc)-ZSM5-HIE	0.002	0.003	0.005
CeO ₂	0.002	0.007	0.009

Apart from the characterization part, the influence of acidity and the chemical state of Ce for different support materials on the ethanol dehydration performance was studied. The reaction was performed in a fixed-bed reactor with various time-on-stream (TOS). The catalytic performance was investigated to adjust the content of the Ce species (Figure 3.15). The catalytic activity increases as the Ce content increases, but it decreases when further increasing the CeO₂ content over 5 wt.% of Ce species. Thus, the highest catalytic activity can be noted by employing 5 wt.% of Ce species.

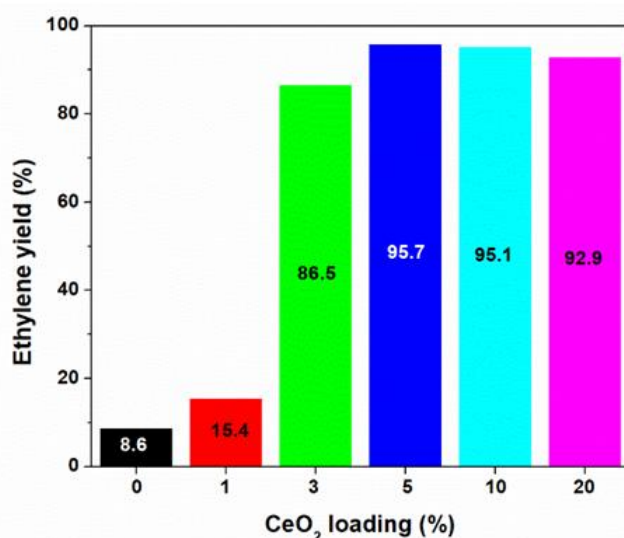


Figure 3.15 Catalytic activity in terms of ethylene yield for different CeO₂ loadings on ZSM5-HIE prepared by ion-exchange process: Reaction condition at 350°C after 12h of reaction time.

As mentioned above, the different types of support material act as another key factor for controlling the Ce chemical state and acidity, which also correlates with the catalytic activity. The catalytic performance of ethanol dehydration can be noticeably enhanced when employing the hierarchical ZSM-5 (ZSM5-HIE) compared to the hierarchical Silicalite-1 (Silicalite1-HIE) as shown in Figure 3.16 and Figure 3.17. Indeed, the same structure of the MFI framework can be observed over both Silicalite1-HIE and ZSM5-HIE, but they hold different Si/Al ratios. The ZSM5-HIE possesses Al sites in the structure with a Si/Al ratio of 60, while Silicalite1-HIE comprises only silica. Due to the fact that the presence of alumina in the solid support can improve the metal-support interaction, the improved catalytic performance of 5Ce(Imp)-ZSM5-HIE with respect to 5Ce(Imp)-Silicalite1-HIE (Figure 3.2, I and II) was achieved.[136]

Furthermore, the chemical state of Ce and acidity are also affected by the Ce insertion technique. A very high yield of ethylene, almost 100%, can be achieved over 5Ce(Exc)-ZSM5-HIE using an ion-exchange process. In fact, the catalytic performance of ethanol dehydration to ethylene is greatly impacted by the acidity of a catalyst.[15]

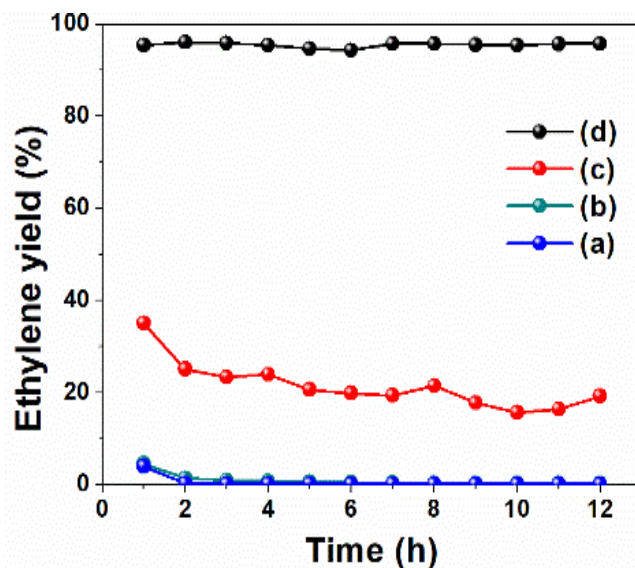


Figure 3.16 Catalytic performance of 5 wt.% of CeO₂ on different materials: (a) 5Ce(Imp)-Silicalite1-HIE, (b) 5Ce(Exc)-ZSM5-CON, (c) 5Ce(Imp)-ZSM5-HIE and (d) 5Ce(Exc)-ZSM5-HIE.

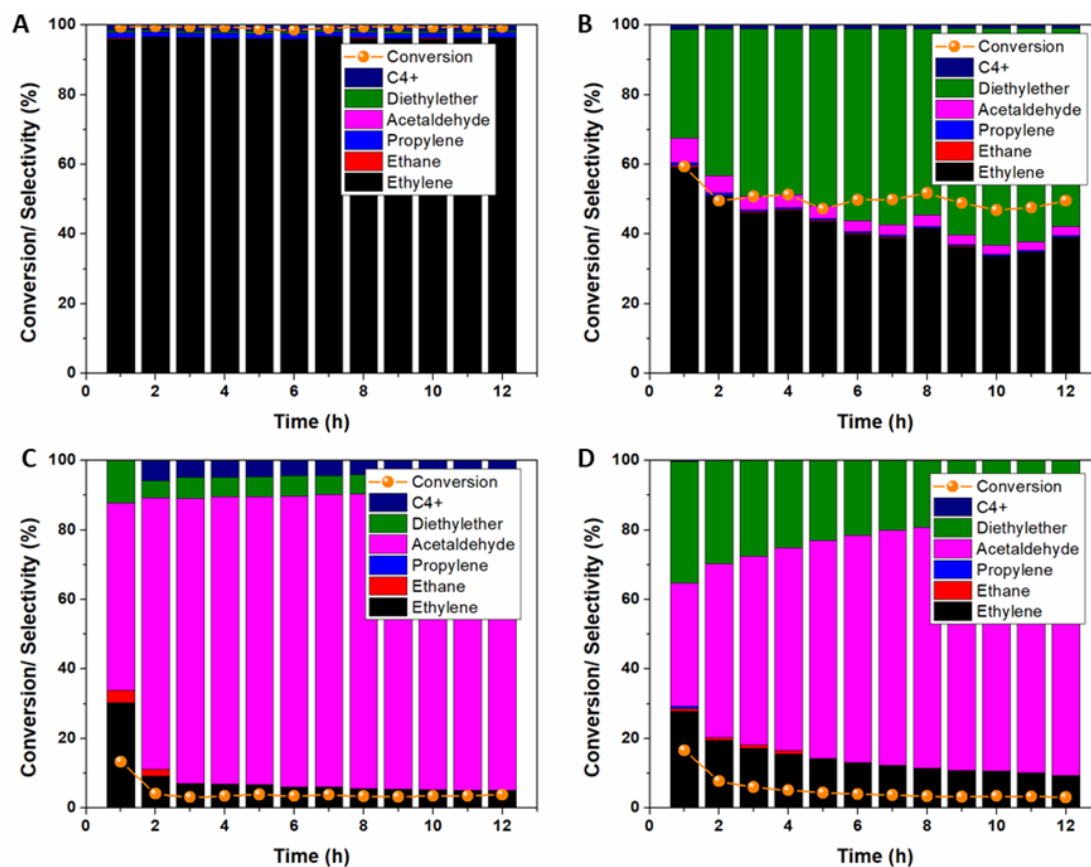


Figure 3.17 Catalytic activity including ethanol conversion and product selectivity over various catalysts: (A) 5Ce(Exc)-ZSM5-HIE, (B) 5Ce(Imp)-ZSM5-HIE. (C) 5Ce(Imp)-Silicalite1-HIE and (D) 5Ce(Exc)-ZSM5-CON.

In addition to the highest metal dispersion and acidity of 5Ce(Exc)-ZSM5-HIE, another reason is the hierarchical ZSM-5 structure, offering higher stabilized Ce active sites (Figure 3.2, III). An ion-exchange process can also provide easily localized metal oxides in zeolite structures.[137] It may then be easier to convert ethanol to ethoxy species using oxygen vacancies, and it is subsequently transformed to ethylene.[138]

Moreover, the catalytic performance of pure hierarchical zeolites is neglectable, as shown in Figure 3.18. Although ZSM5-HIE can produce ethylene in the first period due to the surface properties, its active sites are too small, and then its performance dramatically drops after 5 hours. It can be implied that the enhanced catalytic performance of the prepared catalysts mainly comes from the active Ce species.

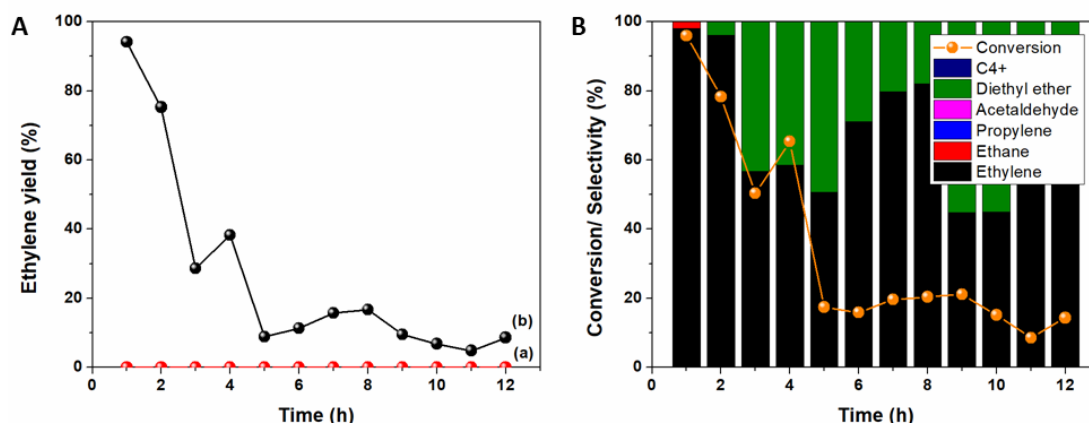


Figure 3.18 Catalytic activity including ethanol conversion and product selectivity over hierarchical zeolites: (A) Catalytic activity of (a) Silicalite1-HIE and (b) ZSM5-HIE and (B) Product distribution over ZSM5-HIE.

Commercial CeO_2 nanoparticles and other support materials, including ZSM5-CON, SiO_2 , and Al_2O_3 , were also tested for ethanol dehydration to confirm that the support material is also of great importance to the catalytic performance. As estimated, a very low conversion of ethanol and low selectivity for ethylene is detected (Figure 3.19 and Figure 3.20) and it is similar to what has been observed for the 5Ce(Exc)-ZSM5-CON. These results verify the formation of bulk CeO_2 when employing conventional ZSM-5 support (Figure 3.2, IV). Thus, the conclusion can be drawn that applying a hierarchical zeolite as a support material is crucial for improving catalyst efficiency for the dehydration of ethanol.

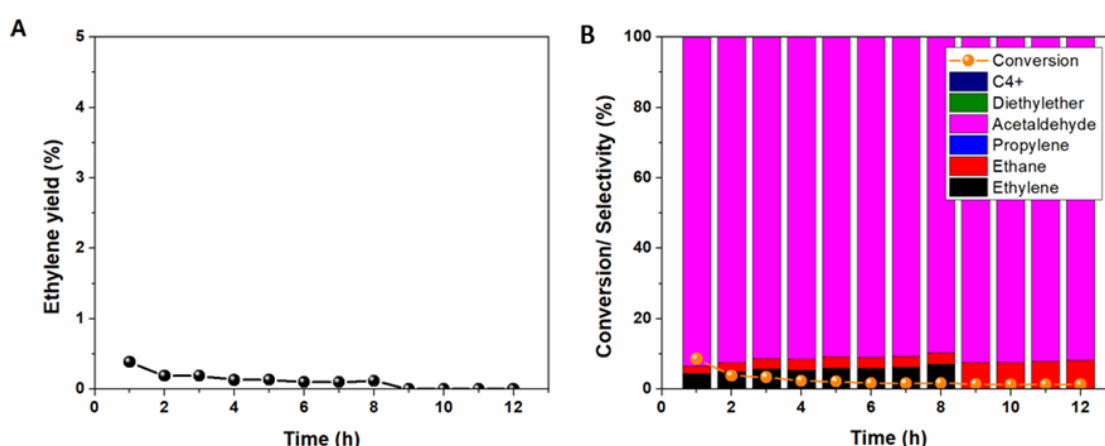


Figure 3.19 Catalytic activity including ethanol conversion and product selectivity of commercial CeO_2 nanoparticles: (A) Catalytic activity, and (B) Product distribution.

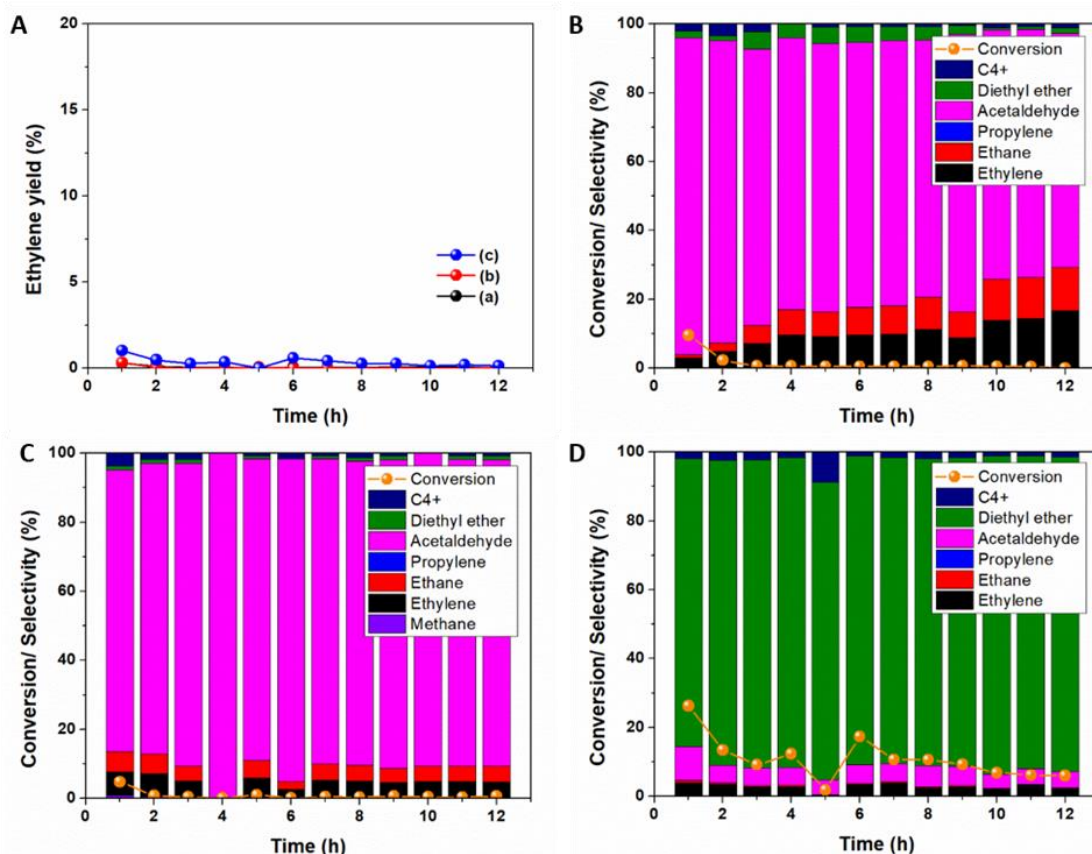


Figure 3.20 Catalytic activity including ethanol conversion and product selectivity: (A) Catalytic performance of (a) 5Ce(Imp)-ZSM5-CON, (b) 5Ce(Imp)-SiO₂ and (c) 5Ce(Imp)-Al₂O₃ and product distribution of (B) 5Ce(Imp)-ZSM5-CON, (C) 5Ce(Imp)-SiO₂ and (D) 5Ce(Imp)-Al₂O₃.

3.4 Conclusion

In summary, to develop the catalytic performance for dehydration of ethanol, the Ce properties, including acidity and chemical state, can be simply modified by employing hierarchical zeolite possessing the aluminum sites in the framework and fine-tuning the Ce insertion by means of an ion-exchange technique. All following parameters, including the acidity, Ce reducibility, and metal-support interaction, can strongly influence the dehydration of ethanol to ethylene. This study explores a new vision to develop ceria-modified hierarchical zeolite catalysts for practical applications of ethanol dehydration, which has not yet been stated before.

Chapter 4

Elaboration of nanoceria-platinum modified hierarchical zeolites for selective alcohol oxidation

4.1 Introduction

It is well-known that the selective oxidation of alcohols to aldehydes counts as one of the most essential processes to provide several intermediate compounds for modern organic synthesis.[139] In particular, the benzyl alcohol oxidation to benzaldehyde is an important challenge, because benzaldehyde is a vital compound, that can be converted to vanillin. It can be applied in various potential applications, such as for the synthesis of dyes, perfumes, food flavors, and industrial solvents. [140, 141] Typically, the partial oxidation of toluene or the hydrolysis of benzylidene chloride has been used for benzaldehyde production. [142] However, a low product yield and wastewater removal issues are the main drawbacks of these methods. [143] Therefore, the direct selective oxidation of benzyl alcohol, under moderate conditions at a mild reaction temperature, is an alternative approach for efficient benzaldehyde production. [144]

Numerous materials have been developed for the highly selective oxidation of alcohol, especially Pt, Pd, Au, and Cu, as key metal catalysts. [145-150] However, practical utilization is still limited by the high costs. To overcome this drawback, many groups have developed catalysts by decreasing the number of noble metals and diluting them with other materials. For example, the bimetallic hybridization between Au and CuO as core-shell nanoparticles was proposed by *Evangelisti et al.* [151] to improve the catalytic performance for alcohol oxidation due to a synergistic effect between Au and CuO nanostructures. Additionally, *Chen et al.* [152] explored the cooperative behavior of a bimetallic Au-Pd catalyst. They discovered that the different nature of Au-Pd interactions supported on ceria-zirconia, which is strongly influencing the catalytic activity, can be fine-tuned by applying different synthesis methods. Moreover, adding low-cost metal oxide materials, in particular, SiO₂, CeO₂, ZrO₂, and

TiO₂ [141, 153, 154] is another hopeful technique to cut the production cost and sustainably enhances the catalytic performance. Among them, one of the most attractive materials for the oxidation of alcohols is CeO₂ with incorporated noble metals. Their notable features include the redox properties of the Ce species, high amount of oxygen vacancies, and hydrocarbon poisoning resistance on metal surfaces. [155, 156] These features can considerably boost the catalytic activity compared to pure metals. Additionally, it has been noted that CeO₂ crystallites can be transformed by doping with silica or alumina, eventually resulting in shifting the oxidation state of ceria. [157]

As strategies mentioned above to develop efficient catalysts, several other solid supports, such as silica, [158] montmorillonite, [159] molecular sieves, [160], and medicinal stone [161], have been employed to stabilize metals in order to boost their catalytic performance for numerous essential processes. A large variety of catalysts for selective benzyl alcohol oxidation have been reported so far. Besides the accessibility of the reactants to the active sites, surface features, for example, the acid/base properties of the support surface can impact the catalytic performance for alcohol oxidation. [162-164] The surface properties of the support have been reported to enhance the active site dispersion, eventually stimulating alcohol activation. [165, 166] Therefore, significant progress in catalyst development can be achieved by using the tunability of solid support properties. In this context, zeolites, which are aluminosilicate compounds, are well-known as solid support used for metal oxides due to their distinctive properties, for instance, a high metal ion-exchange capability, high surface area, and high thermal/hydrothermal stability. [167] Nevertheless, the micropore structure in the zeolite framework causes intracrystalline-diffusion limitations, resulting in low active site utilization. To date, several studies on hierarchical zeolites containing at least two types of cavity systems, for example micropores combined with a meso- or/and macroporous network, [168, 169] have reported that this can enhance the accessibility and molecular transport of guest molecules into the porous structure. [34]

Theoretically, the metal dispersion might be improved by using hierarchical zeolites as promising solid supports for nano metal oxides, due to an extremely high surface area; however, the combination of nanoceria-modified platinum and

hierarchical zeolite has not yet been illustrated, even though it would provide many advantages with respect to the activity of the redox-active species.

In this chapter, the improvement of nanoceria-platinum modified hierarchical zeolites for the selective alcohol oxidation to aldehyde will be presented. A systematic investigation was performed to study the corresponding catalytic activity when using hierarchical zeolite with various alumina contents. Moreover, to characterize catalyst properties, crystalline structures, morphologies, metal size and dispersion, the ability of metal reduction, and the oxidation state of metal species have been demonstrated to obtain the structural detail of developed catalysts. It eventually resulted in understandings the mechanistic viewpoints of alcohol oxidation using different supports to stabilize redox species, which impacted the catalytic performance of selective alcohol oxidation.

4.2 Experimental section

4.2.1 Materials

The chemicals below with analytical grade were utilized without further purification. The main reagents to synthesize zeolites were aluminium isopropoxide (Sigma-Aldrich, $\geq 98.0\%$) and tetraethyl orthosilicate (TEOS, Sigma-Aldrich, $\geq 99.0\%$) as alumina and silica sources, respectively. The mineralizing agent was sodium hydroxide (NaOH, Carlo Erba, $\geq 98.0\%$). Different structure-directing agents (SDAs) were used. To synthesize conventional zeolites, tetrapropylammonium hydroxide (TPAOH, 1.0 M in H₂O) was employed. In contrast, tetrabutylphosphonium hydroxide (TBPOH, Sigma-Aldrich, 40% in H₂O) was utilized for hierarchical zeolite. Precursor materials include cerium acetate (TCI, $>98.0\%$) for cerium oxide and tetraamineplatinum (II) nitrate (Sigma-Aldrich, $\geq 50.0\%$ Pt basis) for active platinum sites. To test the catalytic performance, benzyl alcohol (Sigma-Aldrich, $\geq 99.0\%$) was used as a reactant together with toluene (Merck, $\geq 99.9\%$) and decane (Sigma-Aldrich, $\geq 99.0\%$) as a solvent, and an internal standard, respectively.

4.2.2 Catalyst preparation

4.2.2.1 Synthesis of conventional silicalite-1 zeolite (Silicalite1-CON)

In the typical synthesis procedure,[120] the conventional silicalite-1 zeolite was obtained with a molar synthesis composition of $10\text{SiO}_2: 1\text{TPAOH}: 1.03\text{NaOH}: 400\text{H}_2\text{O}$. Initially, the mixture between 7 g of TEOS and 3.42 g of TPAOH was used as a silica-SDA solution. Then a solution of 0.14 g of sodium hydroxide in DI water was gently poured into the silica-SDA solution and stirred at room temperature for 2 h, to allow the aging process to occur. After that, the synthesis gel was heated at 180 °C for 3 days in a lined hydrothermal synthesis container. The synthesized sample was subsequently washed with DI water, filtered, and dried at 110 °C overnight. Finally, to remove SDA and obtain the product, namely Silicalite1-CON, calcination at 650 °C was carried out for 8 h.

4.2.2.2 Synthesis of hierarchical ZSM-5 zeolite

The different Si/Al ratios (100 and 400) of hierarchical ZSM-5 zeolite (ZSM5-HIE) were obtained using a molar synthesis composition of $60\text{SiO}_2: x\text{Al}_2\text{O}_3: 18\text{TBPOH}: 0.75\text{NaOH}: 600\text{H}_2\text{O}$, where x was 0.075 and 0.3. The same procedure with the previous chapter to prepare hierarchical zeolite was taken. Briefly, the mixture of TEOS and aluminium isopropoxide was first used as a silica-alumina source. Another mixture, including 8.62 g of TBPOH, 0.02 g of sodium hydroxide, and DI water, were gradually poured into the silica-alumina source. Then the solution was blended at room temperature for 12 h, to allow aging. After that, the synthesis gel was heated at 130 °C for 2 days in a lined hydrothermal synthesis container. The synthesized sample was then washed with DI water, filtered, and dried at 110 °C overnight. Finally, to remove SDA and obtain the product, calcination at 650 °C was carried out for 8 h. Hierarchical Silicalite-1 possessing MFI structure with pure silica in the framework ($\text{Si}/\text{Al}=\infty$) denoted as Silicalite1-HIE was also generated.

4.2.2.3 Preparation of Pt/CeO₂ supported on zeolites

The desired amount of cerium acetate together with the prepared zeolites and DI water were mixed at room temperature for 24 h. Then the water was removed using a rotary evaporator and dried at 100 °C overnight. After that, calcination at 550 °C was performed for 6 h to obtain the product denoted as $y\text{CeO}_2\text{-Silicalite1-}$

HIE, $y\text{CeO}_2\text{-ZSM5-HIE}$, and $y\text{CeO}_2\text{-Silicalite1-CON}$ for employing the hierarchical silicalite-1, the hierarchical ZSM-5, and the conventional silicalite-1 as a support material, respectively (where $y = 0, 5, 10, 20$ and 30 wt% of CeO_2), as shown in Figure 4.1. Afterwards, the same sequence was followed for the platinum loading process. The platinum precursor and ceria-modified zeolite involving $y\text{CeO}_2\text{-Silicalite1-HIE}$, $y\text{CeO}_2\text{-ZSM5-HIE}$, and $y\text{CeO}_2\text{-Silicalite1-CON}$ were mixed at room temperature for 24 h, and then evaporated with a rotary evaporator and dried at 100°C overnight. Finally, calcination at 550°C for 6 h allowed obtaining the final product denoted as $z\text{Pt}/y\text{CeO}_2\text{-Silicalite1-HIE}$, $z\text{Pt}/y\text{CeO}_2\text{-ZSM5-HIE}$, $z\text{Pt}/y\text{CeO}_2\text{-Silicalite1-CON}$, respectively (where $z = 0, 0.5, 1$ and 2 wt% of Pt).

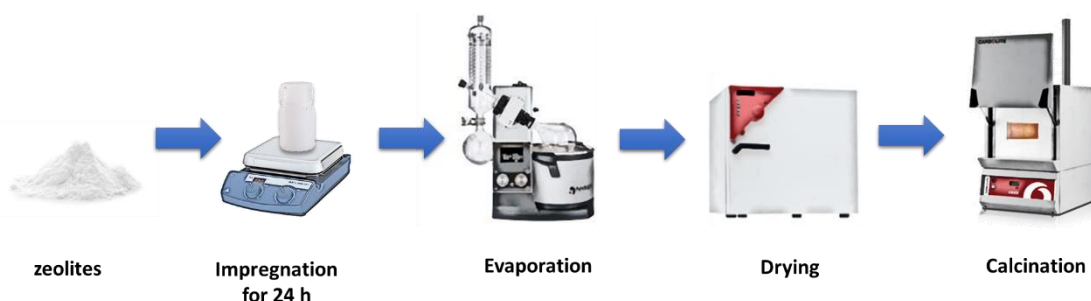


Figure 4.1 Schematic illustration of impregnation method.

4.2.3 Characterization

The crystallographic structure of the materials was investigated from XRD patterns obtained using a Bruker D8 ADVANCE machine with $\text{CuK}\alpha$ radiation (40 kV, 40 mA) in the 2θ ranging from 5° to 60° with 0.02° step size and 1°min^{-1} scan rate. The SEM and TEM images were taken with a JEOL JSM-7610F microscope and JEOL JEM-ARM200F microscope at 200 kV, respectively, to investigate the morphology of the catalysts. To determine the textural properties, N_2 adsorption-desorption measurements at -196°C obtained with a MicrotracBEL, BELSORP-max model was used. Before the measurement, all the analyzed samples were first degassed at 350°C for 24 h. The specific surface area (S_{BET}) was evaluated by the Brunauer–Emmett–Teller (BET) method, associated with quantifying the amount of physical adsorption of N_2 probing gas by van der Waals forces.[170] The micropore surface area and pore volume were determined by the t-plot method based on plotting the adsorbed volume at a given pressure against the average thickness of the adsorbate film obtained at the same pressure for the non-porous reference material. [171, 172] Moreover, to

analyze the elemental composition, wavelength-dispersive X-ray fluorescence spectrometry (WDXRF) was used on a Bruker S8 TIGER ECO machine. The reducibility of the prepared catalysts was checked from the H₂-TPR measurements using a BELCAT II machine equipped with thermal conductivity detectors (TCD). Normally, 0.05 g of analyzed samples were pretreated under a flow of Ar at 300°C for 1 h with 10°C min⁻¹ heating rate and then cooled down to 50°C. Afterwards, the samples were measured at temperatures ranging from 50°C to 900°C with 5°C min⁻¹ heating rate under a 50 ml min⁻¹ flow of 2 v/v% of H₂ in Ar. The BELCAT II equipped with TCD was also used to investigate the metal dispersion by using the H₂-pulse technique. First, the catalysts were treated under air flow at 350 °C for 30 min, followed by Ar purging for 15 min, and then pretreated under H₂ flow at 350 °C for 20 min followed by Ar purging for 20 min to detach weakly adsorbed H₂. Finally, the catalysts were cooled down to room temperature under Ar flow, and a series of H₂ pulses was introduced until reaching a steady state. The metal dispersion (MD) and the average diameter of particles (*D_a* presuming metal particles are spherical) were estimated from theoretical aspects [173] by applying the following equations:

$$MD(\%) = \frac{V_m \times MW \times 10^4}{W\% \times SF}$$

$$D_a(nm) = \frac{6 \times 10^3}{MS \times \rho}$$

where *V_m* is a monolayer volume (mol g⁻¹), *MW* is metal atomic weight (g mol⁻¹), *W%* is the metal percentage in the sample, *SF* is a stoichiometric factor (molecule of gas per metal atom), *MS* is the metal surface area (m² g⁻¹) and *ρ* the metal density (g cm⁻³), respectively. Furthermore, to study the Ce oxidation state, X-ray absorption near-edge structure (XANES) was used to carefully determine the Ce L3-edge XANES spectra by using the transmission mode at the BL5.2 station at Siam Photon Laboratory (Synchrotron Light Research Institute (Public Organization), SLRI), Thailand.

4.2.4 Catalytic activity test

The oxidation of benzyl alcohol was conducted in a batch reactor involving a two-neck round-bottom flask equipped with a condenser column. After pretreatment of the prepared catalysts at 350 °C under 5 ml min⁻¹ of H₂ flow for 2 h,

0.08 g of activated catalyst was moved to a batch reactor. After that, a mixture of 6 ml of toluene as a solvent and decane as an internal standard was added. The flask was closed and heated to 80 °C under vigorous stirring. Benzyl alcohol (50 µl) was inserted into the flask. A balloon of air was used to introduce air into the reactor under atmospheric pressure. The internal calibration analysis method was used to quantify the products. The samples were examined by a gas chromatograph (GC, Agilent 7890B) equipped with a flame ionization detector (FID) and PoraBOND Q capillary column (25 m x 0.32 mm). Finally, the conversion of benzyl alcohol ($X_{Benzyl\ alcohol}$), and the selectivity of benzaldehyde ($S_{Benzaldehyde}$), were determined by the following calculations:

$$X_{Benzyl\ alcohol}(\%) = \frac{n_0 - n_t}{n_0} \times 100\%$$

$$S_{Benzaldehyde} = \frac{n_{Benzaldehyde}}{n_0 - n_t} \times 100\%$$

Where n_0 and n_t are the amount of initial and remaining benzyl alcohol, respectively.

4.3 Results and discussion

X-ray powder diffraction (XRD) was used to obtain the structures of the crystalline phase of nanoceria-platinum modified hierarchical silicalite-1 (Silicalite-1-HIE) with different amounts of metal to confirm the effect of metal contents on the physicochemical features of the catalyst. For Silicalite-1-HIE, XRD patterns of the controlled 1 %wt of Pt contents with varying amounts of CeO₂ are shown in Figure 4.2A. In comparison, various quantities of Pt with a constant 20 %wt of CeO₂ can be seen in Figure 4.2B. As expected, the characteristic peaks for CeO₂ at 2θ of 28, 33, 48, and 56 degrees and Pt at 40 degrees [123] were observed as the number of loading increases for both cases. On the other hand, the silicalite-1 framework crystallinity related to the MFI network topology of zeolite support considerably diminishes as the CeO₂ loading increases (see Figure 4.2A). All prepared catalysts are used later for further catalytic testing to fine-tune the optimized ratio between Pt and CeO₂ contents.

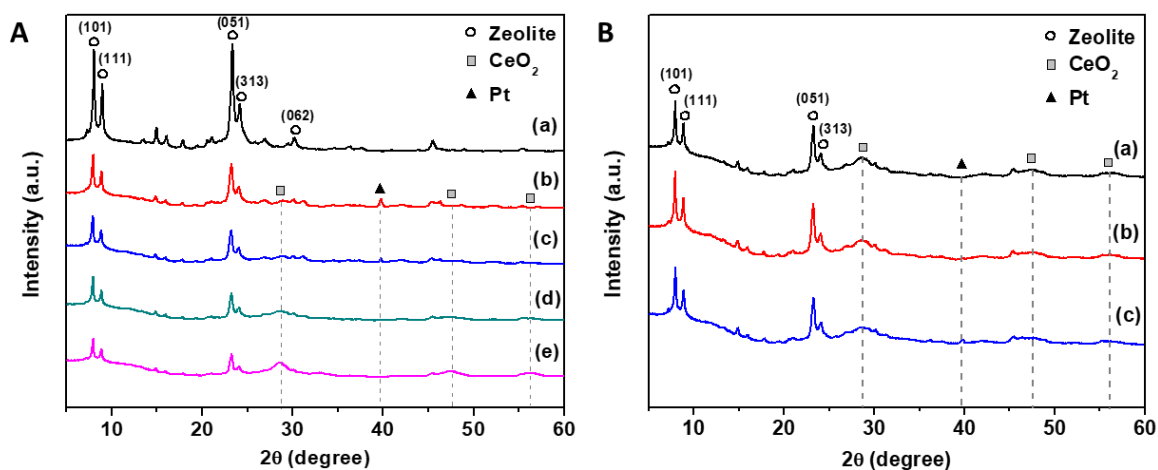


Figure 4.2 A) XRD patterns of Pt/CeO₂ on hierarchical zeolites with different CeO₂ contents: (a) Silicalite1-HIE; (b) 1Pt/5CeO₂-Silicalite1-HIE; (c) 1Pt/10CeO₂-Silicalite1-HIE; (d) 1Pt/20CeO₂-Silicalite1-HIE; (e) 1Pt/30CeO₂-Silicalite1-HIE and B) XRD patterns of Pt/CeO₂ on hierarchical zeolites with different Pt contents: (a) 0.5Pt/20CeO₂-Silicalite1-HIE; (b) 1Pt/20CeO₂-Silicalite1-HIE; (c) 2Pt/20CeO₂-Silicalite1-HIE.

In the case of other support materials, including the conventional silicalite-1 (Silicalite1-CON), hierarchical ZSM-5 (ZSM5-HIE), and commercial CeO₂ nanoparticles, XRD results indicate that the platinum-ceria (1 wt% of Pt and 20 wt% of CeO₂) modified conventional silicalite-1 (1Pt/20CeO₂-Silicalite1-CON) comprises the characteristic CeO₂ peaks. They are comparable to the pattern of 1 %wt of Pt loaded on commercial CeO₂ nanoparticles (1Pt/CeO₂), while the analog peaks are almost invisible for hierarchical supports (1Pt/20CeO₂-Silicalite1-HIE and 1Pt/20CeO₂-ZSM5-HIE) (Figure 4.3). It is reasonable to assume that rather small platinum-ceria nanoparticles can be generated on hierarchical zeolite surfaces. This illustrates well-dispersed CeO₂ and Pt nanoparticles on the 1Pt/20CeO₂-Silicalite1-HIE and 1Pt/20CeO₂-ZSM5-HIE, whereas a large number of agglomerated particles are probably accumulated on the outmost surfaces of Silicalite1-CON.

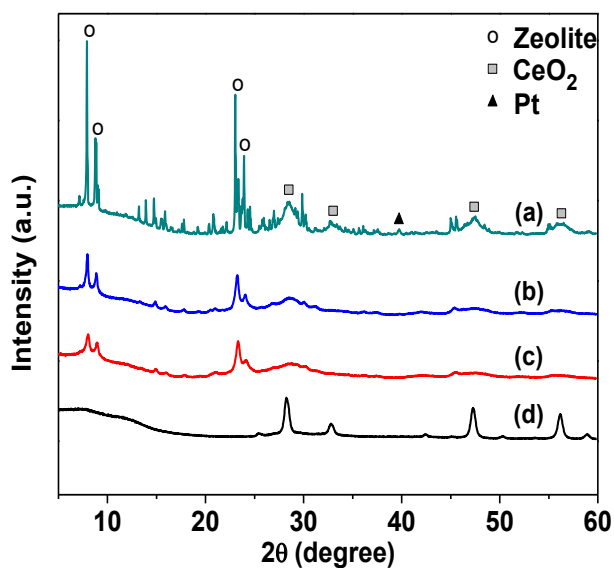


Figure 4.3 Structural information of prepared catalysts from XRD results of different nanoceria-platinum modified supports including (a) 1Pt/20CeO₂-Silicalite1-CON, (b) 1Pt/20CeO₂-Silicalite1-HIE, (c) 1Pt/20CeO₂-ZSM5-HIE, and (d) 1Pt/CeO₂.

To determine the morphologies of the prepared catalysts, scanning electron microscope (SEM) images are shown in Figure 4.4, verifying that the zeolite structure is not affected by the metal insertion. Hierarchical supports exhibit smaller particles generated from self-assembled nanolayers with a size ranging from 150 to 250 nm, while for Silicalite1-CON one can observe large cubic particles as illustrated by the particle size distribution in Figure 4.5.

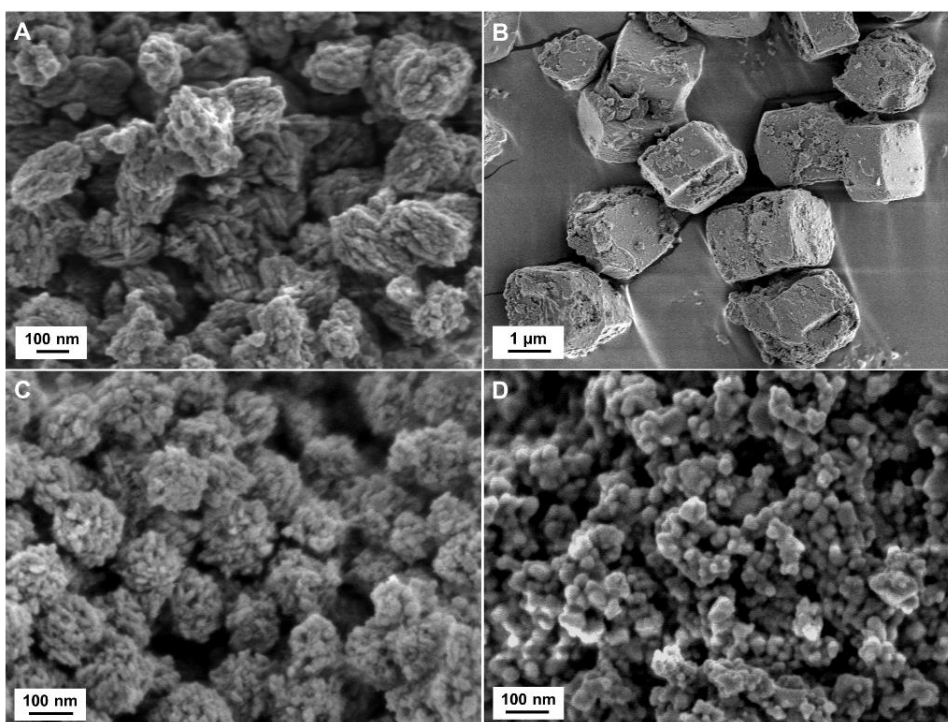


Figure 4.4 SEM images of (A) 1Pt/20CeO₂-Silicalite1-HIE; (B) 1Pt/20CeO₂-Silicalite1-CON; (C) 1Pt/20CeO₂-ZSM5-HIE; (D) 1Pt/CeO₂.

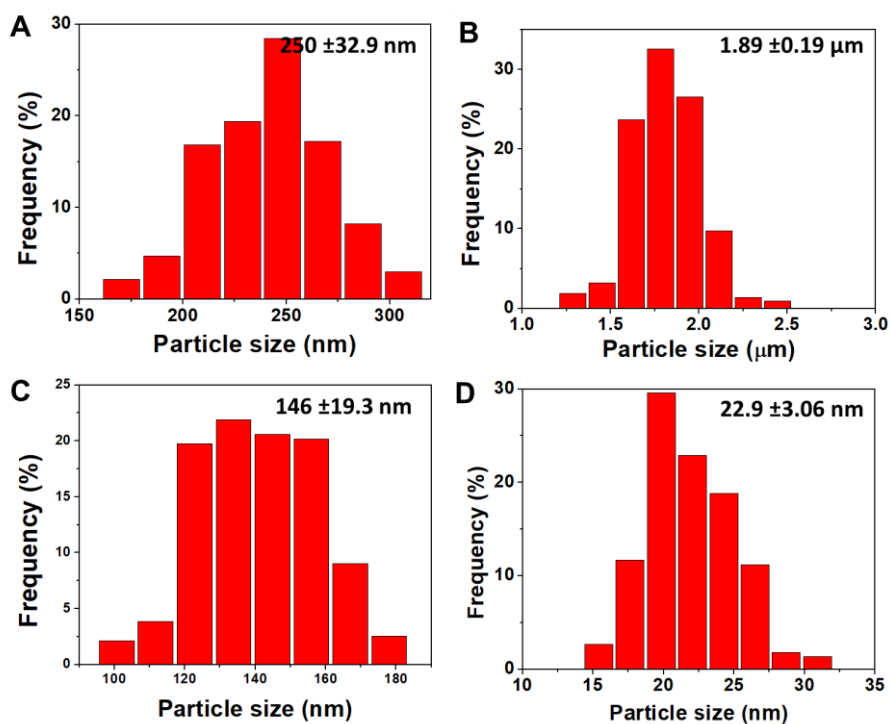


Figure 4.5 Particle size distribution obtained from SEM images of (A) 1Pt/20CeO₂-Silicalite1-HIE; (B) 1Pt/20CeO₂-Silicalite1-CON; (C) 1Pt/20CeO₂-ZSM5-HIE; (D) 1Pt/CeO₂.

To observe the size of metal nanoparticles on supports, 1 wt% of Pt combined with 20 wt% of CeO₂ on different supports, including 1Pt/20CeO₂-Silicalite1-HIE, and 1Pt/20CeO₂-Silicalite1-CON are investigated by transmission electron microscopy (TEM) in Figure 4.6. Metal aggregation occurs on the conventional zeolite, while Silicalite1-HIE can significantly improve the metal distribution. Moreover, well-dispersed Pt and CeO₂ nanoparticles over the hierarchical sample are also revealed by TEM-EDS, as shown in Figure 4.7. Although the particle size of CeO₂ on the conventional support is only twice the one deposited on hierarchical material, a packing of nanoparticles into agglomerates is visible for 1Pt/20CeO₂-Silicalite1-CON. This behavior could be related to the fact that the much smaller size coupled with hierarchical zeolite surface roughness can provide a higher surface area to accommodate CeO₂ nanoparticles, leading to a higher dispersion.

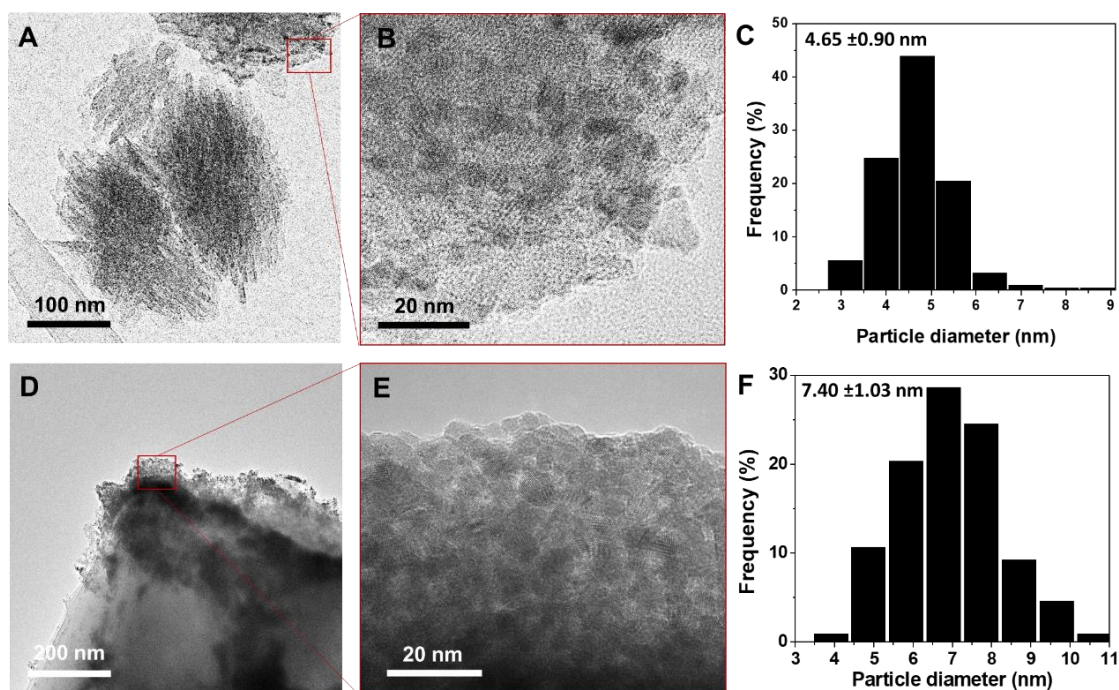


Figure 4.6 TEM images and the particle size distribution of (A-C) 1Pt/20CeO₂-Silicalite1-HIE; (D-F) 1Pt/20CeO₂-Silicalite1-CON.

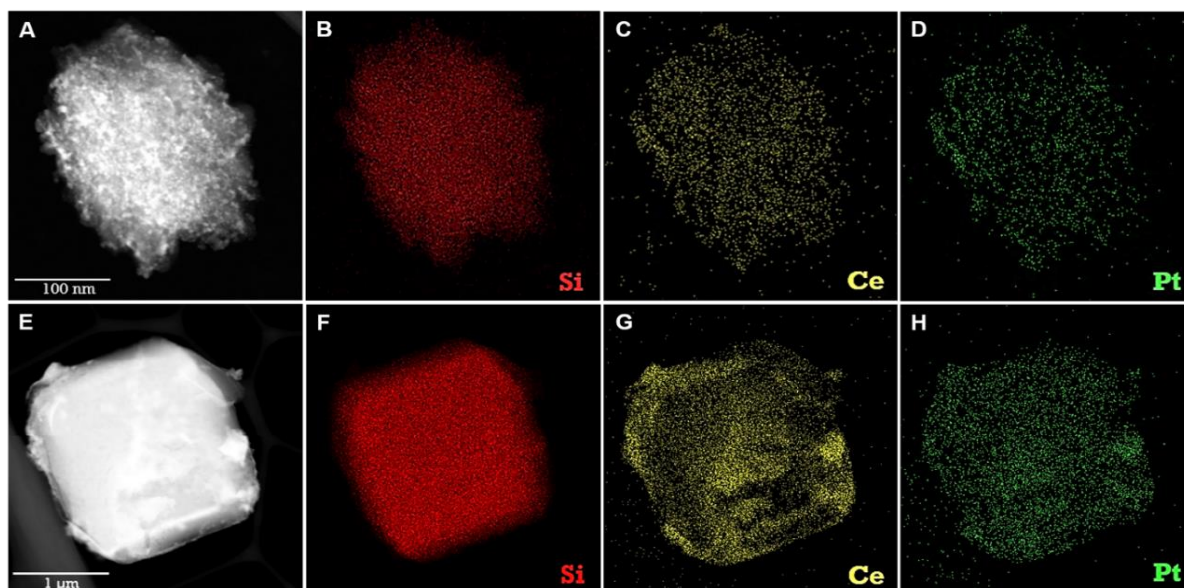


Figure 4.7 TEM-EDS images of (A-D) 1Pt/20CeO₂-Silicalite1-HIE; (E-H) 1Pt/20CeO₂-Silicalite1-CON.

Moreover, the textural properties are determined by N₂ physisorption isotherms in Figure 4.8 and summarized in Table 4.1. N₂ adsorption is generally used to determine the surface area and pore size distribution of various porous materials. The N₂ isotherm analysis allows identifying physisorption mechanisms: monolayer-multilayer adsorption, capillary condensation, or micropore filling.[174] The type I isotherm corresponding to a sole microporous structure is normally obtained for a conventional zeolite, which can be detected in the case of 1Pt/20CeO₂-Silicalite1-CON (Figure 4.8(c)). On the other hand, mixed isotherms between type I, related to the micropore filling at low relative pressure, and type IV at higher relative pressure together with a hysteresis loop ascribed to a capillary condensation inside mesopores and macropores [120] are obtained for hierarchical zeolites (Figure 4.8(a-b)). Moreover, the isotherm is completely different in the case of 1Pt/CeO₂. Almost no adsorption ability at low relative pressure and a small hysteresis loop at high relative pressure can be described as non-porous structures with an interparticle void, as shown in Figure 4.8(d).[175] These explanations obviously indicate that a higher specific surface area can be obtained for hierarchical zeolites, which could offer superior metal dispersion, eventually resulting in better catalytic activity. Besides, even though the SEM image of the 1Pt/CeO₂ (Figure 4.4D) illustrates a small particle size, it possesses a very low surface area due to the CeO₂ aggregation.

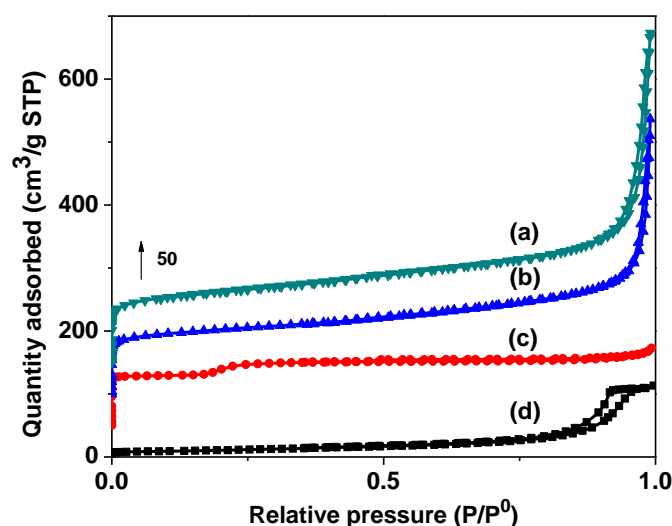


Figure 4.8 N₂ adsorption/desorption isotherms of (a) 1Pt/20CeO₂-ZSM5-HIE; (b) 1Pt/20CeO₂-Silicalite1-HIE; (c) 1Pt/20CeO₂-Silicalite1-CON; (d) 1Pt/CeO₂.

Table 4.1 Textural properties.

Catalyst	S _{BET} ^a (m ² g ⁻¹)	S _{ext} ^b (m ² g ⁻¹)	S _{micro} ^c (m ² g ⁻¹)	V _{total} ^d (cm ³ g ⁻¹)	V _{micro} ^e (cm ³ g ⁻¹)	V _{ext} ^f (cm ³ g ⁻¹)
1Pt/20CeO ₂ -ZSM5-HIE	404.86	225.48	179.38	0.80	0.003	0.80
1Pt/20CeO ₂ -Silicalite1-HIE	375.69	164.35	211.34	0.66	0.03	0.63
1Pt/20CeO ₂ -Silicalite1-CON	331.45	13.98	317.47	0.19	0.15	0.04
1Pt/CeO ₂	38.58	6.03	32.55	0.17	0.16	0.02

^a S_{BET}: Specific surface area (m²g⁻¹) determined by BET method; ^b S_{ext}: External surface area (m²g⁻¹); ^c S_{micro}: micropore surface area (m²g⁻¹), determined by t-plot method; ^d V_{total}: total pore volume (cm³g⁻¹) obtained at P/P₀=0.90; ^e V_{micro}: micropore volume (cm³g⁻¹), determined by t-plot method; ^f V_{ext}: external pore volume (cm³g⁻¹), V_{ext}=V_{total}-V_{micro}.

Additionally, to further verify the metal dispersion ability, different supports modified by nanoceria-platinum were also characterized by H₂ pulse chemisorption measurements. The number of exposed active Pt surfaces analyzed by chemisorption measurements is based on the amount of adsorbed H₂ gas during the investigative

cycle. It has been suggested to perform H₂ chemisorption at a lower temperature to prevent hydrogen spillover.[176] The metal dispersion, which represents the number of metal particles available on the support surface to participate in a reaction, corresponds to the calculation of the adsorbed H₂ quantities.[173] As can be seen in Table 4.2, the metal dispersion of hierarchical samples is remarkably higher than that of the conventional sample. Therefore, these results again corroborate the dispersion improvement of Pt on CeO₂ modified hierarchical zeolites, meaning that the prepared hierarchical catalysts can provide more exposed Pt sites for the reaction. However, it should be noted that the highest dispersion in the case of 1Pt/CeO₂ can be attributed to the small size of CeO₂ nanoparticles used to support Pt due to platinum-ceria interactions leading to well-spread Pt sites.

Table 4.2 Metal dispersion properties.

Catalyst	Si/Al ratio^a	Pt dispersion^b (%)	Particle size^b (nm)
1Pt/20CeO ₂ - ZSM5-HIE	110.2	37.89	2.99
1Pt/20CeO ₂ - Silicalite1-HIE	∞	29.57	3.83
1Pt/20CeO ₂ - Silicalite1-CON	∞	17.65	6.41
1Pt/CeO ₂	-	64.93	1.74

^a Si/Al determined by wavelength dispersive x-ray fluorescence; ^b Pt dispersion and average particle size were determined by H₂-pulse method.

Temperature-programmed reduction with hydrogen (H₂-TPR) profiles was used to consider the redox properties of active sites. It indicates that both 1Pt/20CeO₂-Silicalite1-CON and 1Pt/20CeO₂-Silicalite1-HIE in Figure 4.9A have three main peaks at 200-350, 340-550, and 540-800 °C attributed to the reduction of PtO_x, the surface-active oxygen adjacent to the Pt– CeO₂ interface and the bulk ceria, respectively. [177] It is noteworthy that an important factor for an oxidation reaction is the PtO_x reducibility at the Pt-CeO₂ interface. H₂ consumption was detected at a lower temperature in the case of 1Pt/20CeO₂-Silicalite1-HIE compared to 1Pt/20CeO₂-Silicalite1-CON, meaning that the hierarchical support can well distribute Pt atoms. These behaviors

are also in agreement with the results of XRD and TEM. Therefore, it can be assumed that extremely efficient active sites to stimulate the interfacial lattice oxygen could be favored by the hierarchical zeolite. This should boost the catalytic performance of the oxidation reaction. Furthermore, the reducibility of PtO_x species of a 1Pt/20CeO₂-ZSM5-HIE catalyst is comparable to the case of 1Pt/20CeO₂-Silicalite1-HIE. In the meantime, the sample of 1Pt/CeO₂ shows more distinctive peaks at 400 and 800 °C in Figure 4.9B, owing to the reduction of the ceria surface and bulk ceria, respectively. [68]

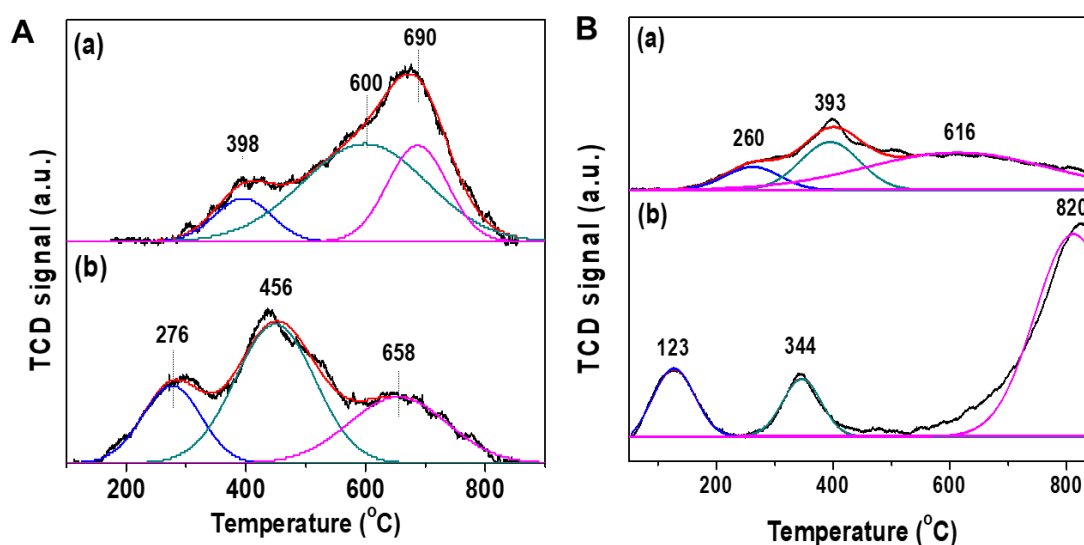


Figure 4.9 (A) H₂-Temperature programmed reduction (H₂-TPR) profiles of (a) 1Pt/20CeO₂-Silicalite1-CON and (b) 1Pt/20CeO₂-Silicalite1-HIE, and (B) H₂-TPR profiles of (a) 1Pt/20CeO₂-ZSM5-HIE and (b) 1Pt/CeO₂.

Apart from characterization experiments, the catalytic activity of the prepared catalysts was investigated using selective benzyl alcohol oxidation to benzaldehyde as a model reaction. As can be seen in Figure 4.10, the oxidation reaction requires some oxidants to carry out the process. This work was performed under the aerobic condition using a saturated air system offering a clean process to produce benzaldehyde from benzyl alcohol oxidation.

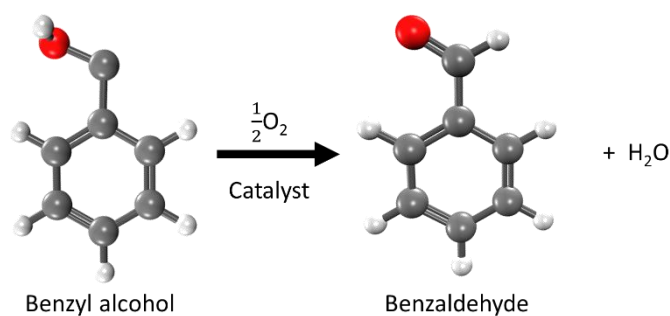


Figure 4.10 Schematic illustration of benzyl alcohol oxidation to benzaldehyde.

The catalysts with different amounts of Pt and CeO₂ supported on hierarchical silicalite-1 (Silicalite1-HIE) were tested with respect to their catalytic performance, as shown in Figure 4.11. A positive impact of hierarchical zeolite modified with nanoceria-platinum on the selective benzyl alcohol oxidation to benzaldehyde was observed. Notably, both isolated Pt and CeO₂ can slightly catalyze the benzyl alcohol oxidation to benzaldehyde. Nevertheless, a combination of Pt and CeO₂ catalyst can significantly improve the catalytic performance by up to 76.4 %, obtained for 1 wt% of Pt combined with 20 wt% of CeO₂ supported on hierarchical silicalite-1 (1Pt/20CeO₂-Silicalite1-HIE).

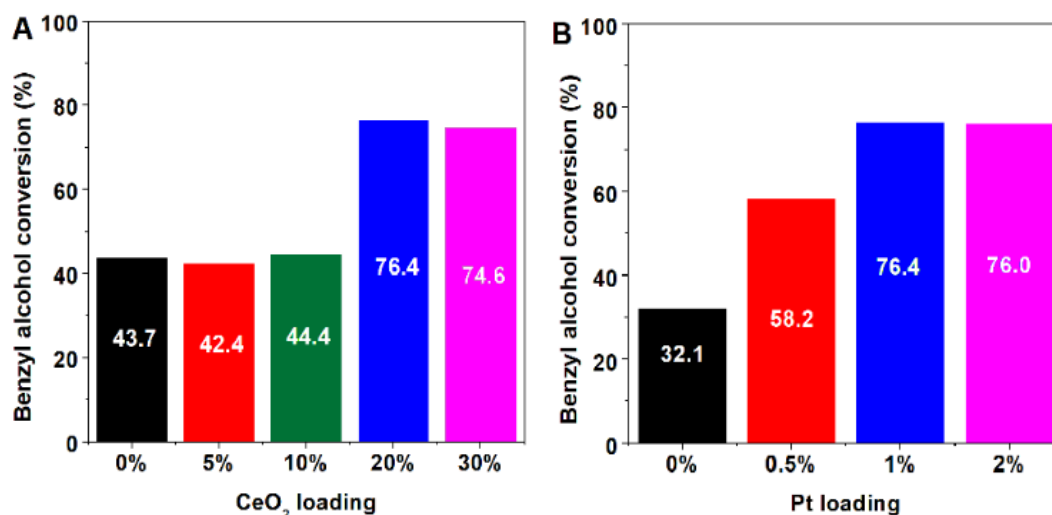


Figure 4.11 Catalytic activity for the selective benzyl alcohol oxidation to benzaldehyde (selectivity=100%) at 24 h of reaction time using a batch reactor at 80°C over (A) 1 wt% of Pt supported on Silicalite1-HIE combined with different CeO₂ contents and (B) 20 wt% of CeO₂ supported on Silicalite1-HIE combined with different Pt contents.

The support materials also play an important role in the catalytic activity, as can be seen in Figure 4.12 and Figure 4.13. The catalytic performance of 1Pt/20CeO₂-Silicalite1-HIE is clearly superior with respect to 1Pt/20CeO₂-Silicalite1-CON. Obviously, 1Pt/20CeO₂-ZSM5-HIE provides the highest yield of benzaldehyde. In this case, the framework of ZSM5-HIE and Silicalite1-HIE is the same, but ZSM5-HIE contains the Al sites in the structure, while the Silicalite1-HIE is only a pure silica (Table 4.1). The higher catalytic performance of 1Pt/20CeO₂-ZSM5-HIE compared to 1Pt/20CeO₂-Silicalite1-HIE correlates to the fact that the metal-support interaction can be improved by the existence of alumina in the solid support.[136] However, for 1Pt/CeO₂, a considerably lower catalytic performance is observed compared to that of the hierarchical ones even though it has highly dispersed active sites (Table 4.2).

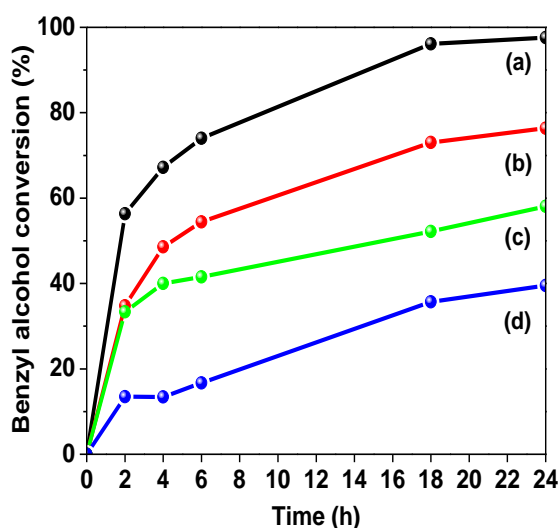


Figure 4.12 Catalytic performance of different support catalysts: (a) 1Pt/20CeO₂-ZSM5-HIE, (b) 1Pt/20CeO₂-Silicalite1-HIE, (c) 1Pt/CeO₂ and (d) 1Pt/20CeO₂-Silicalite1-CON (100% selectivity towards benzaldehyde).

Another factor that influences the catalytic performance is the Si/Al ratio of hierarchical zeolites. From Figure 4.13, an improvement of the catalytic activity can be deduced for the lower Si/Al, containing a higher amount of Al atoms in the structure. Additional Al sites in the ZSM-5 framework provide Bronsted acid sites, which generally interact with the active metal phase.[178] Therefore, the active sites can be stabilized on the zeolite support, enhancing metal dispersion further, eventually improving the catalytic performance.[179]

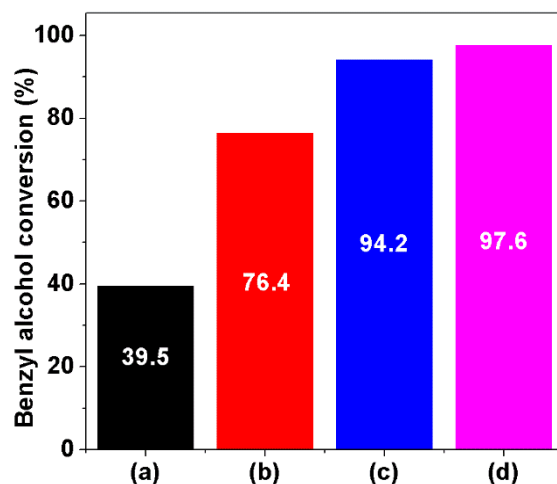


Figure 4.13 Catalytic performance for the selective benzyl alcohol oxidation to benzaldehyde (selectivity=100%) in a batch reactor at 80°C for 24 h of reaction time over 1 wt% of Pt combined with 20 wt% of CeO₂ supported on different materials: (a) 1Pt/20CeO₂-Silicalite1-CON; (b) 1Pt/20CeO₂-Silicalite1-HIE; (c) 1Pt/20CeO₂-ZSM5(Si/Al=400)-HIE; (d) 1Pt/20CeO₂-ZSM5(Si/Al=100)-HIE.

To understand in more detail the active site structures, the Ce oxidation state of the prepared catalysts was examined by using X-ray absorption near-edge spectroscopy (XANES) measurement. Figure 4.14 demonstrates the spectra of Ce L₃ edge XANES measurements of Pt combined with CeO₂ on different supports and two reference standards, which are Ce(NO₃)₃·6H₂O and CeO₂ representing Ce³⁺ and Ce⁴⁺ references, respectively. The absorption into the 5d level with the 4f occupancy in the initial state is assigned to peak I, and it reasonably implies Ce³⁺ existence in the sample. The occupancy of the 4f level in the final state, and the absorption into the 5d level with no occupancy in the 4f level in either the initial or final state are related to the double peaks (peak II and III, respectively). Therefore, these peaks are expected when Ce⁴⁺ appears.[180]

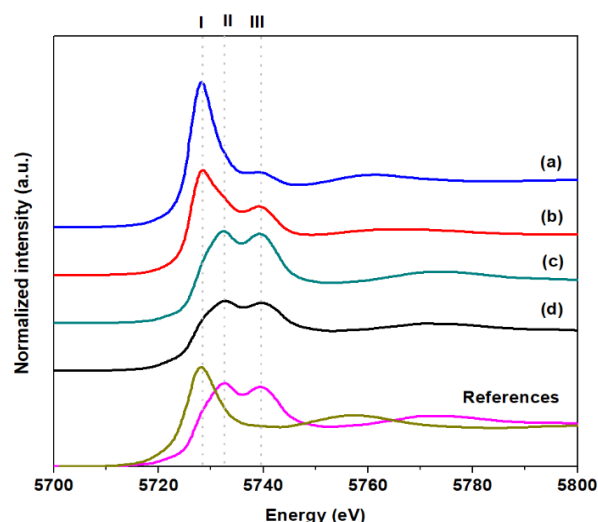


Figure 4.14 Normalized Ce L₃ edge XANES spectra of different prepared catalysts: (a) 1Pt/20CeO₂-ZSM5-HIE, (b) 1Pt/20CeO₂-Silicalite1-HIE, (c) 1Pt/20CeO₂-Silicalite1-CON, (d) 1Pt/CeO₂ and Ce³⁺ (yellow) and Ce⁴⁺ (pink) standard references.

It can be observed that Ce⁴⁺ peaks can completely fit for 1Pt/CeO₂ and 1Pt/20CeO₂-Silicalite1-CON. While 1Pt/20CeO₂-Silicalite1-HIE and 1Pt/20CeO₂-ZSM5-HIE display a combined feature of two Ce species with a major Ce³⁺ fraction. These observations suggest that the support material influences the Ce oxidation state, leading to different catalytic performances. For further clarification, smaller particles of ceria, which are well-dispersed on solid supports, typically provide a higher amount of Ce³⁺ and oxygen vacancy.[181] Compared to a conventional catalyst, hierarchical catalysts can offer higher catalytic activity owing to higher oxygen vacancy, facilitating lattice oxygen mobility. Thus, the better CeO₂ dispersion can provide a higher fraction of Ce³⁺ resulting from the type of support materials. Additionally, Al sites in the ZSM-5 framework can further influence the metal dispersion more than Silicalite1-HIE, as illustrated in Figure 4.15. The Ce L₃ edge XANES spectra were fitted as shown in Figure 4.16 by arranging an arctan function to imitate the edge jump and fit three Gaussian functions (I, II, III).[182] The quantitative summary of the Ce oxidation state from XANES was analyzed in Table 4.3.

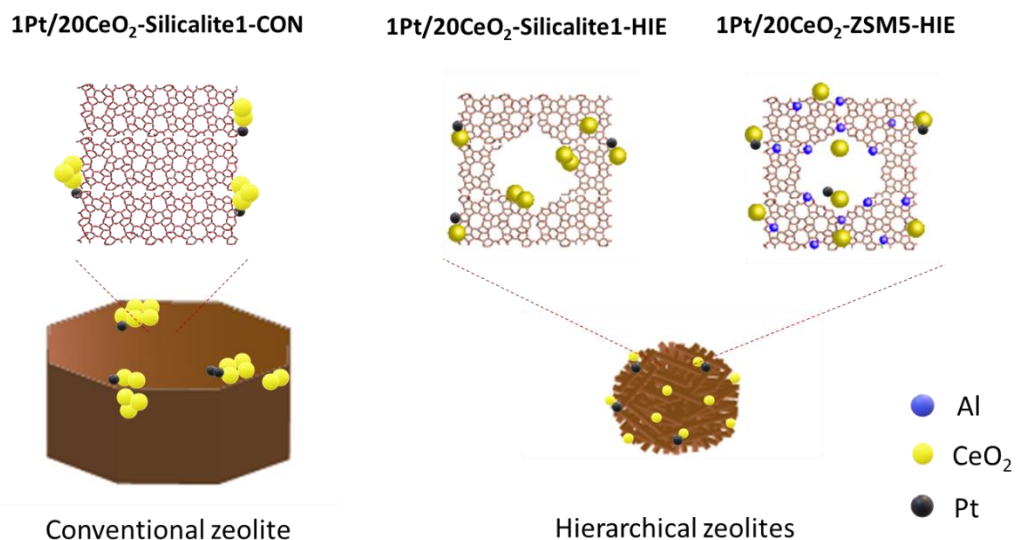


Figure 4.15 Schematic illustration of the proposed structures of the prepared catalysts.

Nevertheless, the highly dispersed active sites of 1Pt/CeO₂ exhibit a lower catalytic performance, probably due to a higher Ce⁴⁺ content compared with hierarchical supports. Besides, the reaction testing cannot change the Ce oxidation state (Table 4.3). Thus, it can be concluded that the prepared catalysts provide recyclable active sites for selective benzyl alcohol oxidation.

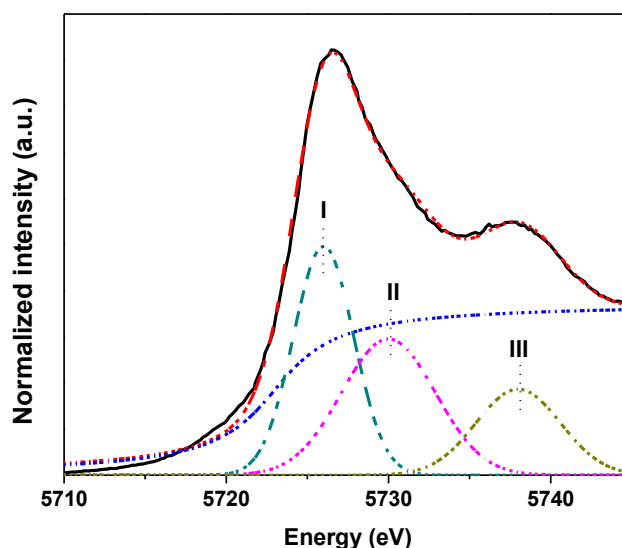


Figure 4.16 Fitting curves of XANES spectra of the Ce L₃ edge for 1Pt/20CeO₂-ZSM5-HIE.

Table 4.3 Quantitative analysis of Ce oxidation obtained from XANES for fresh and used catalysts [182, 183].

Catalysts	I ^I	I ^{II}	I ^{III}	%Ce ³⁺
1Pt/20CeO ₂ -ZSM5-HIE-Fresh	5.79	5.353	3.044	65.5
1Pt/20CeO ₂ -ZSM5-HIE-Used	7.904	4.132	3.197	71.2
1Pt/20CeO ₂ -Silicalite1-HIE-Fresh	5.166	6.156	3.175	61.9
1Pt/20CeO ₂ -Silicalite1-HIE-Used	5.451	5.66	3.309	62.2
1Pt/20CeO ₂ -Silicalite1-CON-Fresh	0.69	5.853	7.714	8.2
1Pt/20CeO ₂ -Silicalite1-CON-Used	0.225	4.132	4.458	4.8
1Pt/CeO ₂ -Fresh	1.642	5.651	9.683	14.5
1Pt/CeO ₂ -Used	1.426	1.898	5.815	19.7

* Fittings of the Ce L₃ edge XANES spectra of the synthesized samples and the estimation of Ce³⁺ concentration in the sample is calculated as follows: %Ce³⁺ = I^I/(I^I+I^{II}+I^{III}), where I^I, I^{II} and I^{III} are the intensities of the different peaks.

To understand the corresponding mechanistic aspects, the schematic illustration in Figure 4.17 shows the proposed reaction mechanism of alcohol oxidation over Pt/CeO₂ supported on hierarchical catalysts, including the subsequent three major steps: (i) a transfer of an electron from the reduced Ce³⁺ to O₂, then generating Ce⁴⁺ and surface-active oxygen species (O²⁻)[184]; (ii) the formation of a Pt-hydride by H atom adsorption from benzyl alcohol, which joins O²⁻ to create H₂O and an O vacancy; (iii) an O vacancy comprising electron transfers to Ce⁴⁺, regaining fresh active sites of Pt⁰ and Ce³⁺ for the next catalytic cycle. [185] Hence, this behavior can be defined as an electron bridge to facilitate the relocation of electrons from reductants to oxidants in the catalytic oxidation system.

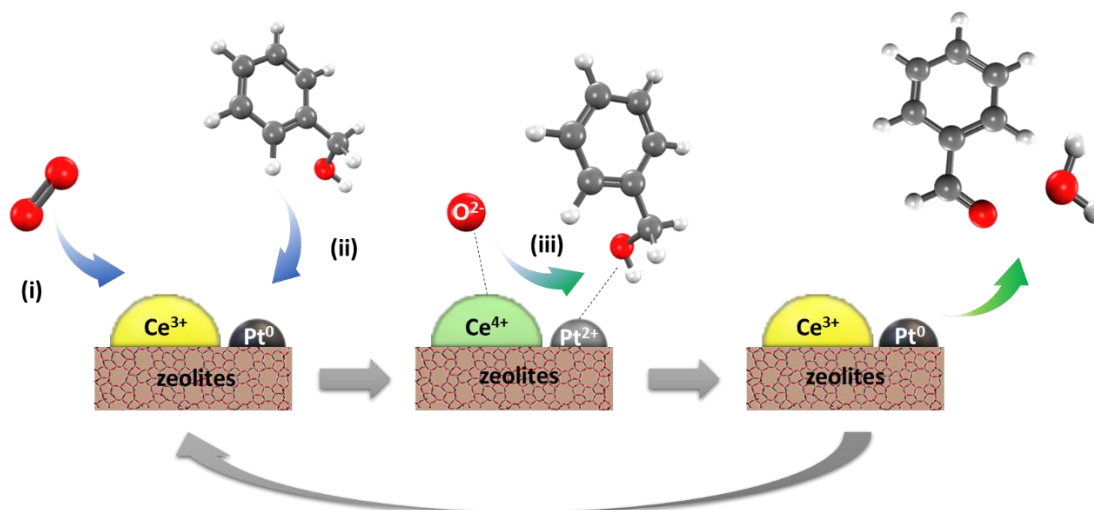


Figure 4.17 Schematic illustration of catalytic reaction mechanism of alcohol oxidation on Pt/CeO₂ supported on hierarchical zeolite surfaces.

4.4 Conclusion

In summary, the selective benzyl alcohol oxidation to benzaldehyde as a model reaction was developed over the Pt-CeO₂ supported hierarchical zeolite catalysts. The catalytic performance can be greatly enhanced by the synergic effect of Pt, CeO₂, and hierarchical zeolites not only due to an improvement of the dispersion of metal but also boosting the Ce³⁺ portion with respect to inactive Ce⁴⁺ species compared to when using a conventional zeolite as solid support. Additionally, a very high yield of benzaldehyde can be reached when using the combination of 1 wt% of Pt together with 20 wt% of CeO₂ modified hierarchical ZSM-5 having a low Si/Al ratio. This indicates an advantageous catalyst with lowering the noble metal content, which satisfies cost-effective and environmentally friendly concerns, eventually improving potentially practical procedures for the sustainable production of fine chemicals

Chapter 5

Electrochemical activity mapping of Pt-CeO₂ gradient films prepared by bipolar electrochemistry

5.1 Introduction

Many organic chemistry syntheses involve electron transfer. In a classical redox reaction, the electron transfer takes place between two chemical species. When a dangerous and polluting reducing (or oxidizing) reagent is employed, it is possible to substitute it with an electric current coming directly from electrodes. This process is known as electrosynthesis. Due to its high versatility, simplicity, ease to scale up, and low-cost process, electroorganic synthesis has attracted much attention. Moreover, this method can deliver a cleaner process because it can avoid conventional chemical reagents that need to be well managed.[186] Aromatic aldehydes are crucial intermediates for large industries of fine chemicals.[139] Particularly, the oxidation of benzyl alcohol to benzaldehyde is a representative and attractive process because aromatic aldehydes can be used in various systems such as industrial solvents, plastic additives, and perfumes.[140] The method usually used to synthesize benzaldehyde suffers from low yield and generates a problem in wastewater management.[143, 144] Therefore, the direct selective oxidation of liquid benzyl alcohol is considered a credible option to generate benzaldehyde efficiently under mild conditions.

Recently, many catalysts have been used for selective oxidation, especially noble metals such as Pt, Pd, and Au.[148-150] Although they play a key role as useful metal catalysts, they still suffer from their lack of cost-effectiveness. Various studies have established new candidates to overcome this limitation by reducing the noble metal content via mixing with other materials. This promising approach, allowing to reduce the cost of catalyst and improve the catalytic performance in a sustainable way, uses metal oxide such as CeO₂, TiO₂, Fe₃O₄, and Al₂O₃. [154, 187-189] Among them, CeO₂ is one of the most attractive materials for alcohol oxidation owing to its remarkable properties, such as the redox properties between Ce³⁺ and Ce⁴⁺ species,

high oxygen vacancy capacity, and poisoning tolerance of hydrocarbons on metal surfaces. [190, 191]. Its use combined with noble metals can considerably improve their catalytic activity.[119]

Bipolar electrochemistry (BPE) is a powerful method to generate gradients on conductive substrates. In BPE, a conducting object is placed inside an electrolyte solution, between the anode and the cathode. There is no direct contact between the conducting object and these two electrodes. [86, 90] Thanks to the electric field applied between the two electrodes, a potential drop exists along the bipolar electrode generating an oxidation reaction at one side of the conducting object and a reduction reaction on the opposite side. This object is called a bipolar electrode because it has anodic and cathodic sides.[192] The key point is that the potential varies along the bipolar electrode generating different deposition rates. The electrochemical reaction rate depends on the local polarization, a gradient of composition, thickness, morphology, and other physicochemical parameters can be easily generated. Several compositional gradient films have been reported. For example, the synthesis of a CdS gradient was performed on a gold electrode.[193] An Ag-Au alloy gradient has been deposited on a stainless steel bipolar electrode, and also a Ni-Cu alloy gradient has been prepared in one step by BPE. A gradient in size and spatial distribution of gold and silver nanoparticles were reported.[194, 195] Interestingly, up to three different materials were used to fabricate the gradient film containing Cu, Ni, and Zn in a single experiment using bipolar electrodeposition.[90]

Scanning electrochemical microscopy (SECM) utilized a microelectrode to investigate the local electrochemical performance of surfaces. The SECM is distinctive among scanning probe techniques because it can image the electrochemical activity to analyze inhomogeneous surfaces.[92, 93] This technique introduces the concept of chemical imaging, which can be obtained by using a mobile ultramicroelectrode (UME). The tip is scanned at a very close distance (a few μm) above the sample surface, and its current response is simultaneously monitored as a function of the tip position. SECM imaging is highly dependent on the tip-sample distance and the nature of the sample surface with respect to its electrochemical activity/conductivity.[95] Hence, SECM is a powerful tool to analyze the gradient of electrocatalyst materials generated by BPE. This type of study has been done by *Beugré et al.*[196], more

precisely, they used scanning electrochemical cell microscopy (SECCM) to study the activity of nickel (oxy)hydroxide gradient.

In this chapter, Pt-CeO₂ films were prepared by electrodeposition on a glassy carbon electrode. Its electrochemical activity of benzyl alcohol oxidation to benzaldehyde was characterized by cyclic voltammetry (CV). After this first study, a Pt-CeO₂ gradient film was made by BPE. These surfaces were characterized by Scanning electron microscopy (SEM), energy dispersive X-ray (EDS) analysis, X-ray photoelectron spectroscopy (XPS), and Raman spectroscopy (RAMAN) to elucidate the nature and chemical state of the deposited catalyst films on a glassy carbon electrode. Finally, SECM was employed to investigate the local catalytic activity of the gradient in benzyl alcohol electrooxidation using the redox competition mode of SECM.[197] Therefore, this work builds on the previous chapter to further explore the different conditions for the preparation of cerium oxide combined with platinum particles in order to study the catalytic performance.

5.2 Experimental section

5.2.1 Materials

All chemicals were of analytical grade and used as received. Cerium(III) nitrate hexahydrate (Ce(NO₃)₃, >99%, Sigma-Aldrich) and potassium hexachloroplatinate(IV) (K₂PtCl₆, >99.9%, Sigma-Aldrich) were used as CeO₂ and Pt precursor, respectively. Potassium nitrate (KNO₃, >97%, Merck) was used as an electrolyte in the electrodeposition system. The glassy carbon plates (13x13x1 mm, TW Hochtemperatur-Werkstoffe GmbH) were used as substrate. To investigate the electrocatalytic performance, potassium hydroxide (KOH, >85%, Sigma-Aldrich) was used as an electrolyte. Benzyl alcohol (BnOH, 99%, Sigma-Aldrich) and ferrocenedimethanol (>97%, Sigma-Aldrich) were used to test the performance of the films. Milli-Q water (resistivity = 18.2 MΩ cm) was used for all experiments.

5.2.2 Film preparation

The homogeneous film and electrochemical properties of the sample electrode were measured on an electrochemical workstation (CHI900) with a conventional three-electrode system. The glassy carbon, Pt wire, and Ag/AgCl were

used as working, counter, and reference electrodes, respectively. The KNO_3 0.1 M solution containing K_2PtCl_6 1 mM, and $\text{Ce}(\text{NO}_3)_3$ 1 mM, was used as Pt and CeO_2 precursors. The electrodeposition was performed by chronoamperometry at -0.6 V for 1 min. Finally, the obtained film was rinsed with Milli-Q water and then gently dried under air flow. Moreover, the gradient was fabricated by bipolar electrodeposition, and the electric field was applied with a high-power supply from Heinzinger (PNC 600-1000) in a homemade cell. The GC plate was used as a bipolar electrode. It was located between the feeder electrodes, which were separated by 55 mm, in a solution of Pt and CeO_2 precursor (see Figure 5.9). Two glassy carbon plates were used as feeder electrodes. Teflon membranes were used to separate the anodic and the cathodic compartment from the bipolar electrode. A potential of 10.6 V was applied for 1 min in order to fabricate Pt- CeO_2 gradient films. Then, it was followed by washing with Milli-Q water several times and gently drying under air flow.

5.2.3 Electrochemical System and Instrumentation

All the electrochemical performance tests for benzyl alcohol electrooxidation were carried out at room temperature conditions (25 °C) using KOH 0.1 M solution with the presence of 0.2 M benzyl alcohol. SECM experiments were performed with the CHI920C (CH Instruments Inc., the USA). Scanning electron microscopy (SEM) images were acquired with Hitachi Tabletop Microscope TM-1000. High-resolution SEM images were recorded with a TESCAN VEGA3 SBH instrument. Optical profilometry was performed with the KLA-Tencor Alpha-step profilometer. The glassy carbon electrode ($d = 3$ mm), Pt wire, and Ag/AgCl (NaCl 3 M) were used as working, counter, and reference electrodes, respectively. Prior to the electrodeposition, the glassy carbon electrodes were polished with alumina (0.05 μm) and subsequently cleaned by ultrasonication for 15 min in ethanol and Milli-Q water and then dried under air flow. For the SECM experiments, a homemade cell was used to analyze the GC plate. The tip was a homemade Pt disk UME with a diameter of 25 μm and an $\text{RG} \approx 7$. RG is the ratio between the radius of the insulating sheath (r_g) and the radius of the conductive disk (a) (i.e., $\text{RG} = r_g/a$). Scanning electron microscopy (SEM) images were acquired with a Hitachi Tabletop Microscope TM-1000. High-resolution SEM images were recorded with a TESCAN VEGA3 SBH instrument. Performance tests for the electrooxidation of benzyl alcohol were carried out at room temperature (25 °C) using a 0.1 M KOH solution with the presence of 0.2 M benzyl

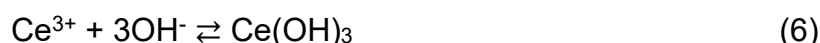
alcohol. Cyclic voltammetry was measured to determine the global performance of homogeneous film for electrooxidation of benzyl alcohol at a scan rate of 50 mV s⁻¹. In contrast, the local electrochemical performance of gradient film was investigated by SECM.

5.3 Results and discussion

The interest in the electrodeposition of catalysts over other deposition techniques lies in a variety of reasons, such as low cost of equipment, control of deposition thickness and uniformity, and the ability to form films on substrates with a complex shape.[198] The electrolytic deposition of CeO₂ is based on the local increase of pH in the cathodic region. In this work, the homogeneous layers were fabricated using a constant potential of -0.6 V for 1 min, which is the optimized condition edited from the study by *F. Kitamura et al.*[199], in the presence of Ce(NO₃)₃ 1 mM, K₂PtCl₆ 1 mM, and KNO₃ 0.1 M. The mechanism of the cathodic electrodeposition of CeO₂ film is quite complex. It can be divided into three parts.[200-202] Firstly, hydroxyl ions, OH⁻, are generated at the cathodic pole by the reduction of O₂ and H₂O, as shown in the following equations.



Secondly, the Ce ions react with the hydroxyl ions.



Finally, Ce(OH)₃ and CeO₂ precipitate at the surface of the electrode.





Cyclic voltammograms (CVs) indicate the appropriate potential to fabricate the film using $\text{Ce(NO}_3)_3$ in KNO_3 0.1 M as the precursor of CeO_2 as shown in Figure 5.1. From the mechanisms (Eq. 1-8), hydroxyl molecules, OH^- , play an essential role in the formation of CeO_2 . Thus, the potential at which the formation of CeO_2 films can take place is around -0.6 V using the OH^- produced by the reduction of O_2 as shown in the red line.

In the case of Pt deposition, the blue line in Figure 5.1 indicates the film generated from the reduction of Pt^{4+} to Pt^{2+} , then Pt^{2+} to Pt metallic form assigned to the cathodic reduction at -0.35 and -0.6 V, respectively. Therefore, Pt film can be fabricated from cathodic electrodeposition as indicated in the following mechanisms (Eq. 9-10).[199]



In addition, to further enhance the film performance, Pt combined CeO_2 film (Pt- CeO_2) was investigated. The pink line in Figure 5.1 demonstrates the two Pt reduction peaks coupled with another cathodic peak at -0.9 V and the anodic peak at -0.6 V. These last two peaks were assigned to water splitting and reoxidation of Pt sites, respectively. It is in agreement with the film formation in phosphate solution.[203] As discussed before, CeO_2 film can be formed by using OH^- , which can be generated from O_2 reduction at -0.6 V, which is also suitable for Pt deposition. Then, the facile electrodeposition for Pt- CeO_2 electrocatalyst was performed on a glassy carbon electrode (GC) at -0.6 V for 1 min.

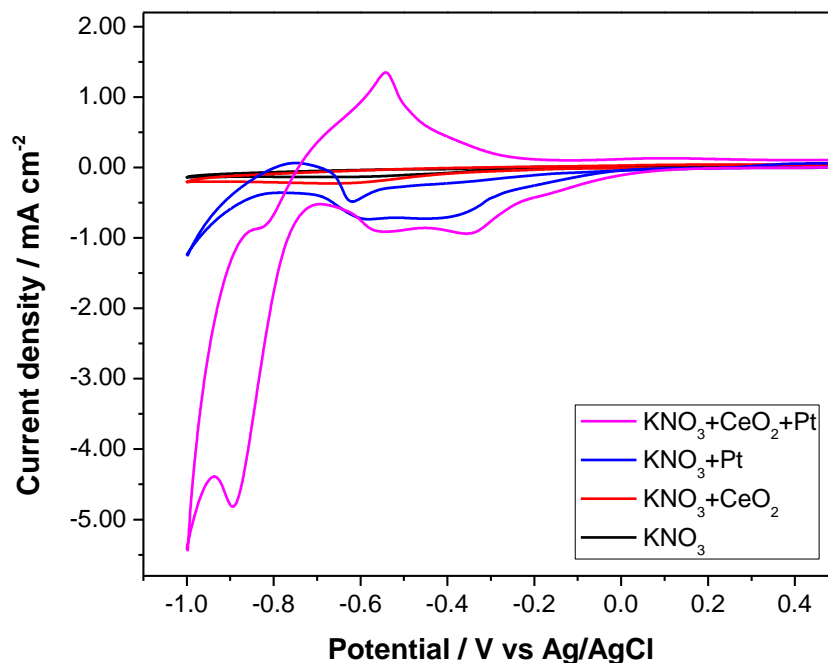


Figure 5.1 CV at a glassy carbon electrode in KNO_3 0.1 M solution (black line) containing 1 mM of CeO_2 precursor (red line), 1 mM of Pt precursor (blue line), and both of them (pink line) with the scan rate of 50 mV s^{-1} .

Scanning electron microscopy (SEM) was used to observe the structure of homogeneous films prepared by conventional electrodeposition. All the surface presents a homogeneous morphology, as shown in Figure 5.2. The particles in Figure 5.2(b) and (c) are uniformly distributed over the entire surface. The clear particles can be observed in the case of Pt ($90 \pm 23 \text{ nm}$) and Pt- CeO_2 film ($54 \pm 14 \text{ nm}$). Interestingly, the case of the Pt- CeO_2 combination provides significantly smaller particles and higher density leading to a higher electroactive surface area.

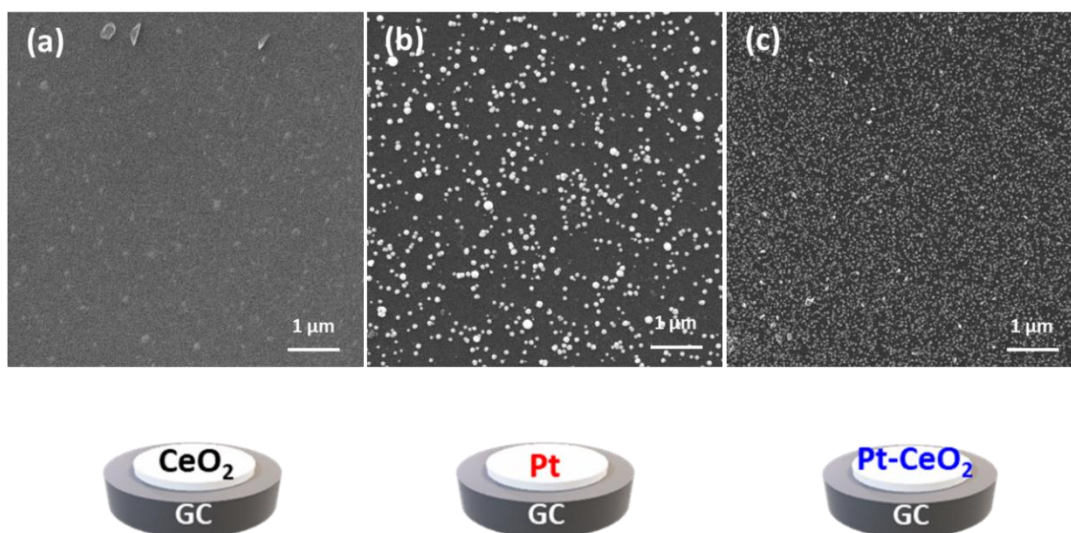


Figure 5.2 SEM images of the homogeneous (a) CeO₂ film, (b) Pt film and (c) Pt-CeO₂ film fabricated on GC electrode at -0.6 V for 1 min.

Moreover, X-ray photoelectron spectroscopy (XPS) was then employed to investigate the chemical composition of Pt-CeO₂ and the oxidation states of elements. XPS analysis of Ce 3d and Pt 4f binding energy regions for Pt-CeO₂ can be seen in Figure 5.3. XPS Ce 3d spectrum analysis suggests the presence of Ce³⁺ and Ce⁴⁺ species. Four peaks of Ce³⁺, including 904.0, 900.4, 885.9, and 881.8, together with six peaks of Ce⁴⁺ at 917.0, 907.8, 901.3, 898.6, 889.4, and 882.8, respectively, [204] can be observed in Figure 5.3(a). It implies that Pt-CeO₂ film is a mixture of Ce³⁺ and Ce⁴⁺ species with a major fraction of Ce⁴⁺ (58%). It confirms the proposed mechanism that the film can be composed of both CeO₂ and Ce(OH)₃. [205] The Pt 4f spectrum fitting indicates that the Pt NPs were composed of Pt²⁺ and Pt⁰ species, as illustrated by the peaks at 72.8 and 71.2 eV binding energies, respectively, [206, 207] suggesting a significant portion of Pt⁰ states (see Figure 5.3(b)). Moreover, the elemental analysis was determined as a function of the etching time. As shown in Figure 5.3(c), the amount of Pt and Ce elements decreases as the etching time increases. This allows to roughly estimate the thickness of Pt-CeO₂ film. A thickness of about 78 nm was determined depended on the etching rates based on a silica substrate. Additionally, the existence of Pt and Ce can be proved by Raman spectra (Figure 5.3(d)). The characteristic peaks of CeO₂ and PtO_x are observed at 453 and 593 cm⁻¹, respectively. [208, 209] These results can again verify the existence of Pt and CeO₂ over the successfully prepared Pt-CeO₂ homogeneous film.

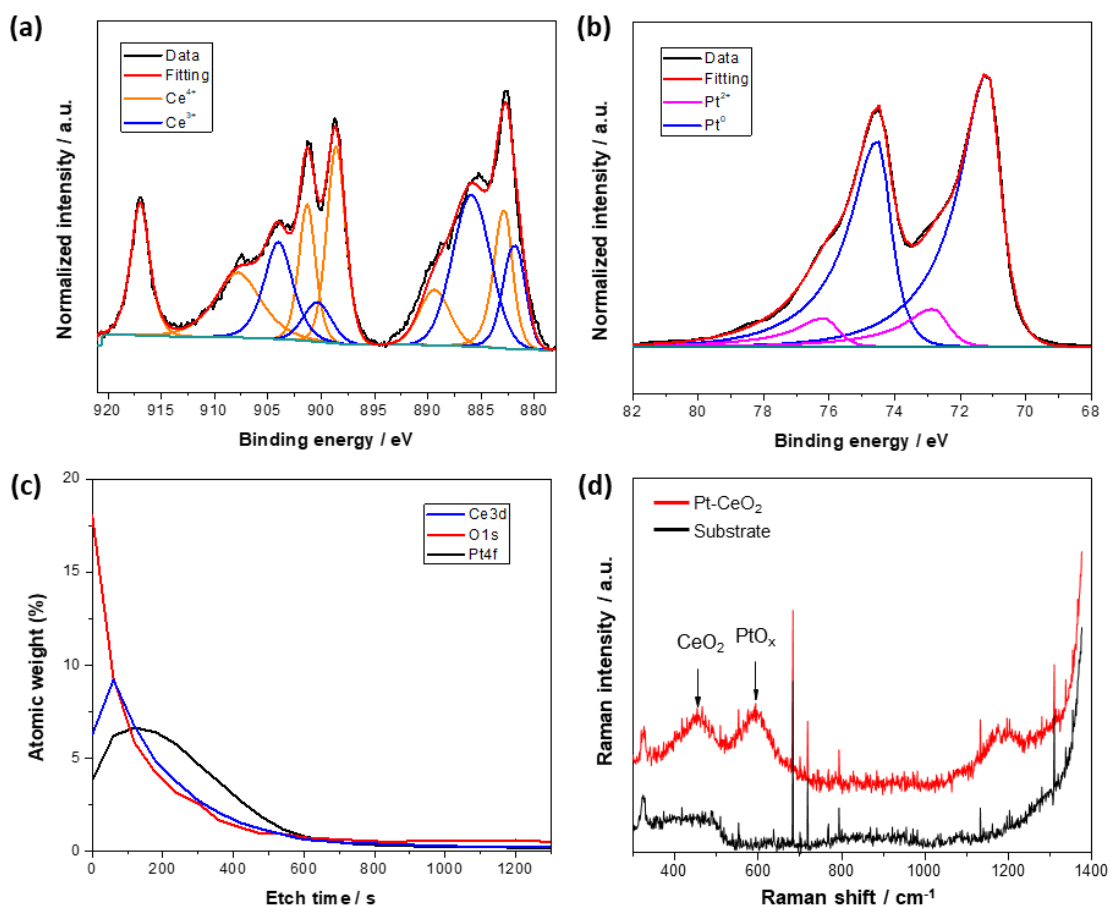


Figure 5.3 X-ray photoelectron spectra fitting of Pt-CeO₂ homogeneous film for (a) Ce 3d and (b) Pt 4f binding energy regions at 0 s, (c) Elemental analysis along the different etching time and (d) Raman spectra of Pt-CeO₂ homogeneous film.

Following the film physical characterization, the electrochemical activity of benzyl alcohol (BnOH) oxidation was investigated by cyclic voltammetry. This reaction was performed on three different homogeneous electrodes, including CeO₂, Pt and Pt-CeO₂. To normalize the electrodes, the electrochemical active surface area (EAS) measurement was enclosed. The average Coulombic charge of hydrogen adsorption and desorption (Q_H) was used to calculate the EAS of the electrodes, as illustrated in Figure 5.4.

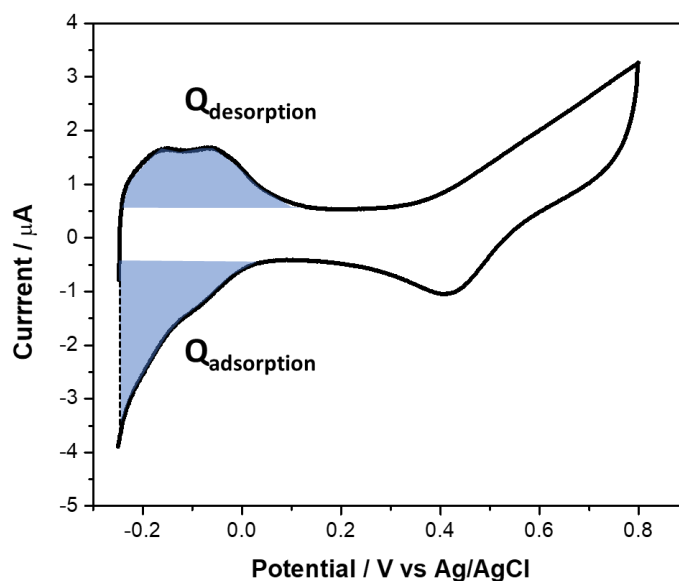


Figure 5.4 Cyclic voltammogram of the prepared electrode in H_2SO_4 0.5 M at scan rate 20 mV s^{-1} .

For the calculation, the EAS can be obtained by the following equation[210]:

$$\text{EAS} = Q_{\text{H}}(\text{Pt}) \times 0.21 \quad (11)$$

where Q_{H} is the average charge for hydrogen adsorption/desorption (mC cm^{-2}), (Pt) denotes the platinum loading (mg cm^{-2}) at the surface of the electrode, and 0.21 corresponds to the charge required to oxidize a monolayer of H_2 on Pt.

The BnOH oxidation (see Figure 5.5) was performed in KOH solution 0.1 M following the study of Y. Yang.[211] As illustrated in Figure 5.6, the CeO_2 film on GC electrode does not exhibit any obvious peak corresponding to the benzyl alcohol oxidation. This indicates that benzyl alcohol oxidation is kinetically slow at the surface of CeO_2 . While on the Pt film, two oxidation peaks appear. These peaks correspond to benzyl alcohol and benzaldehyde oxidation at -0.1 V and 0.2 V, respectively. Interestingly, the peak current density for BnOH oxidation is much higher on Pt combined with CeO_2 film (Pt- CeO_2). This can be explained by enhancing the electrocatalytic performance correlating to oxygen vacancies in CeO_2 that can facilitate the oxidation reaction in accordance with previous work.[119] The synergistic effect between Pt and CeO_2 can be described as a correlated feature of these two materials. CeO_2 can facilitate the regenerated active Pt^0 from Pt-hydride, formed by adsorption of H atom of benzyl alcohol, eventually producing benzaldehyde and H_2O .

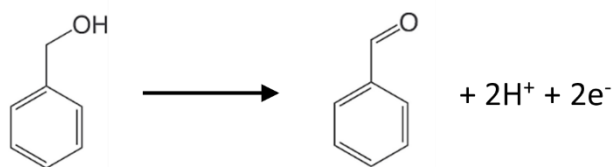


Figure 5.5 Schematic illustration of benzyl alcohol electrooxidation to benzaldehyde.

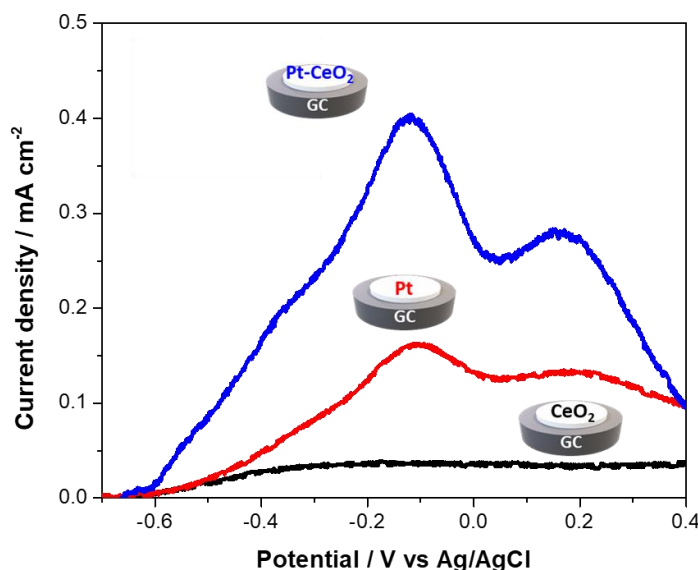


Figure 5.6 Benzyl alcohol electrooxidation at the homogeneous films: CeO₂ (black line), Pt (red line) and Pt-CeO₂ (blue line), in KOH 0.1 M solution containing benzyl alcohol 0.2 M under room temperature at $v = 50 \text{ mV s}^{-1}$.

However, when the deposition was made in two steps, a lower performance was observed. The two-step Pt-CeO₂ film was prepared by the electrodeposition at -0.6 V for 1 min at each step, as shown in Figure 5.7. A deposition of CeO₂ first, then followed by the electrodeposition of Pt was denoted as Pt/CeO₂ while an inverse sequence was assigned to CeO₂/Pt. As presented in Figure 5.8, compared to the Pt-CeO₂ film prepared in one step, the performance of the film prepared in two-step is considerably lower. This behaviour can emphasize the benefit of a single step deposition which is not only easier, faster but also achieves better performance due to the synergistic effect of metal-metal oxide interaction at the interface resulting in more charge transfer and better stability.[212]

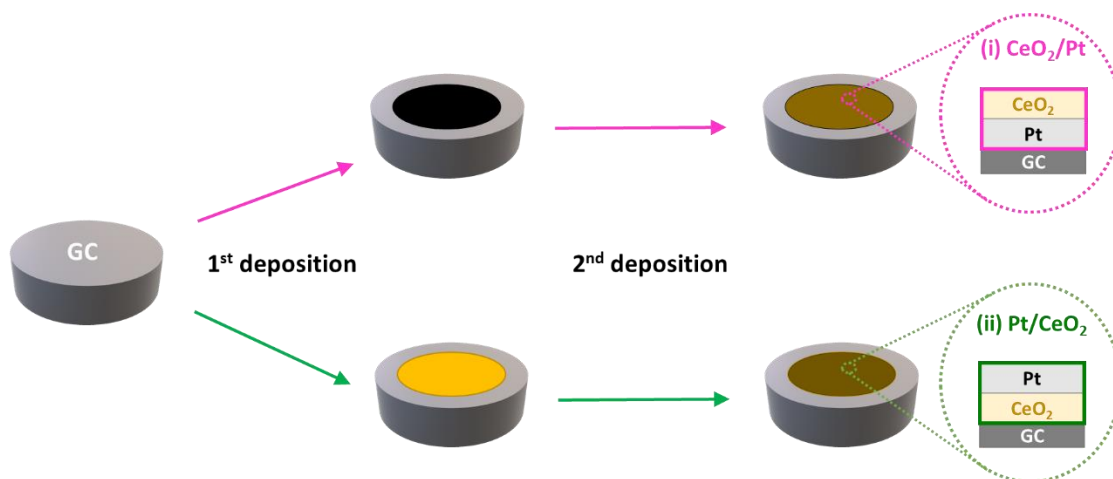


Figure 5.7 Schematic illustration of a two-step deposition on a glassy carbon electrode at -0.6 V for 1 min in each step to prepare two layers of Pt and CeO_2 film: (i) CeO_2/Pt for Pt deposition first, then coated with CeO_2 film and (ii) Pt/CeO_2 for CeO_2 deposition first, then coated with Pt film.

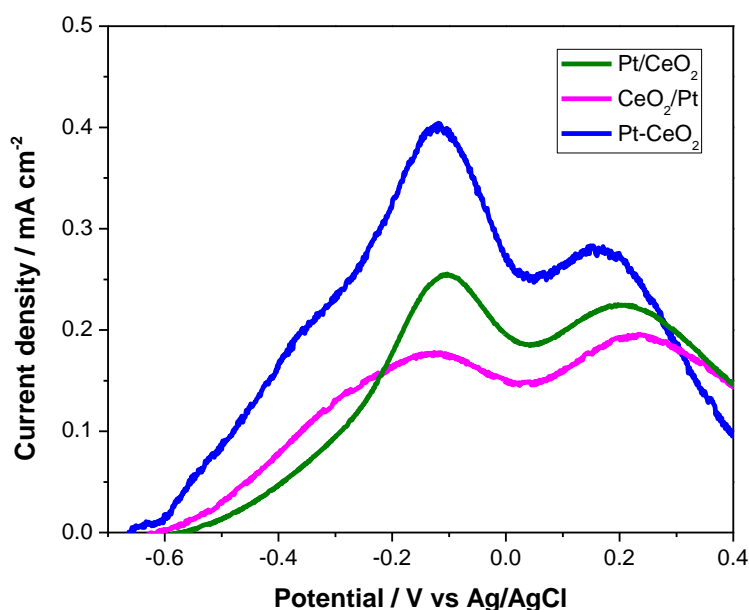


Figure 5.8 Benzyl alcohol electrooxidation at the homogeneous films: Pt- CeO_2 (blue line), Pt/ CeO_2 (green line) and CeO_2/Pt (pink line), in KOH 0.1 M solution containing benzyl alcohol 0.2 M under room temperature with the potential scan rate = 50 mV s^{-1} .

Based on the electrocatalytic performance of the homogeneous films, we have shown that the combination of Pt and CeO_2 can significantly improve the film performance. However, only one potential value (-0.6 V) has been employed to

prepare the films. Because the potential is a key parameter for preparing the film, it is important to test different values. That is why we decided to use bipolar electrochemistry (BPE) to prepare Pt-CeO₂ gradient film and to investigate the local electrochemical properties obtained thanks to the linear variation of the electrochemical driving force alongside the bipolar electrode.[90] Thanks to BPE, the electrodeposition Pt-CeO₂ was made at different potentials by using only one experiment. The bipolar electrodeposition experiment was set up as shown in Figure 5.9. The potential drop across the BPE, ΔE , can be approximated using the following equation[196]:

$$\Delta E = E_{tot}(l_{BPE}/d) \quad (12)$$

where E_{tot} is the potential difference between the feeder electrodes, l_{BPE} is the length of the bipolar electrode, and d is the distance between the feeder electrodes. In this work, $E_{tot} = 10$ V, $l_{BPE} = 13$ mm, and $d = 55$ mm resulting in a potential drop of ca. 2.5 V across the BPE. The potential variation is high enough in this condition to allow the hydroxyl ion formation at the cathodic pole of the BPE (δ^-). Due to the electric field across the electrolytic solution, different potential distributions generated different hydroxyl ion concentrations, which is the key factor for the CeO₂ formation.

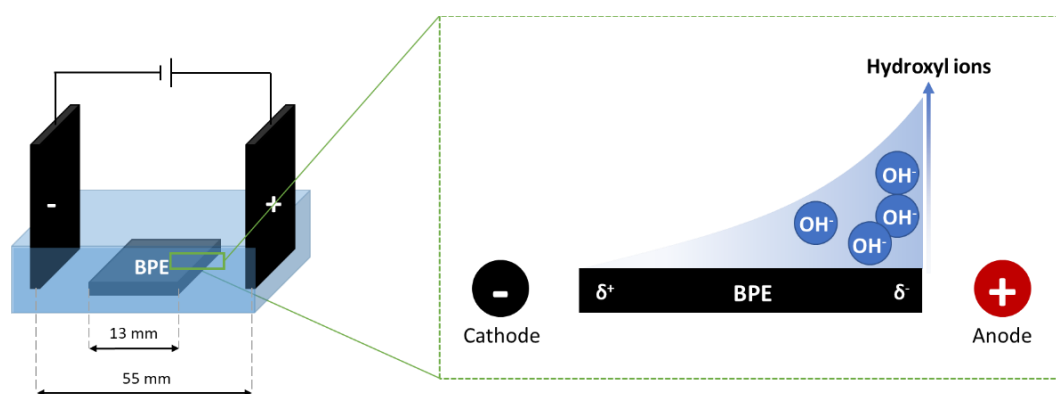


Figure 5.9 Schematic illustration of bipolar electrodeposition experiment.

As discussed before, the combination of Pt and CeO₂ can significantly enhance film performance. The morphology of Pt-CeO₂ film fabricated at 1.93 V cm⁻¹ for 1 min using Ce(NO₃)₃ 1 mM, K₂PtCl₆ 1 mM, and KNO₃ 0.1 M can be seen in Figure 5.10. The different morphology can be observed along the bipolar electrode due to potential distribution along the electrode. Figure 5.10(b-d) shows the higher magnification of

different areas of the Pt-CeO₂ gradient film. It indicates that the aggregated nanoparticles, diameter around 200 nm, can be observed on the area (b) and (d) while tiny and uniform size (~50 nm) is obtained over the area (c), which is located at 1-2 mm from the electrode edge. Moreover, it can be seen that the deposited film width is around 3 mm from the edge of the electrode. SEM-EDS line scan profiles further verify that the Pt-CeO₂ gradient film is successfully fabricated on a glassy carbon electrode using bipolar electrodeposition.

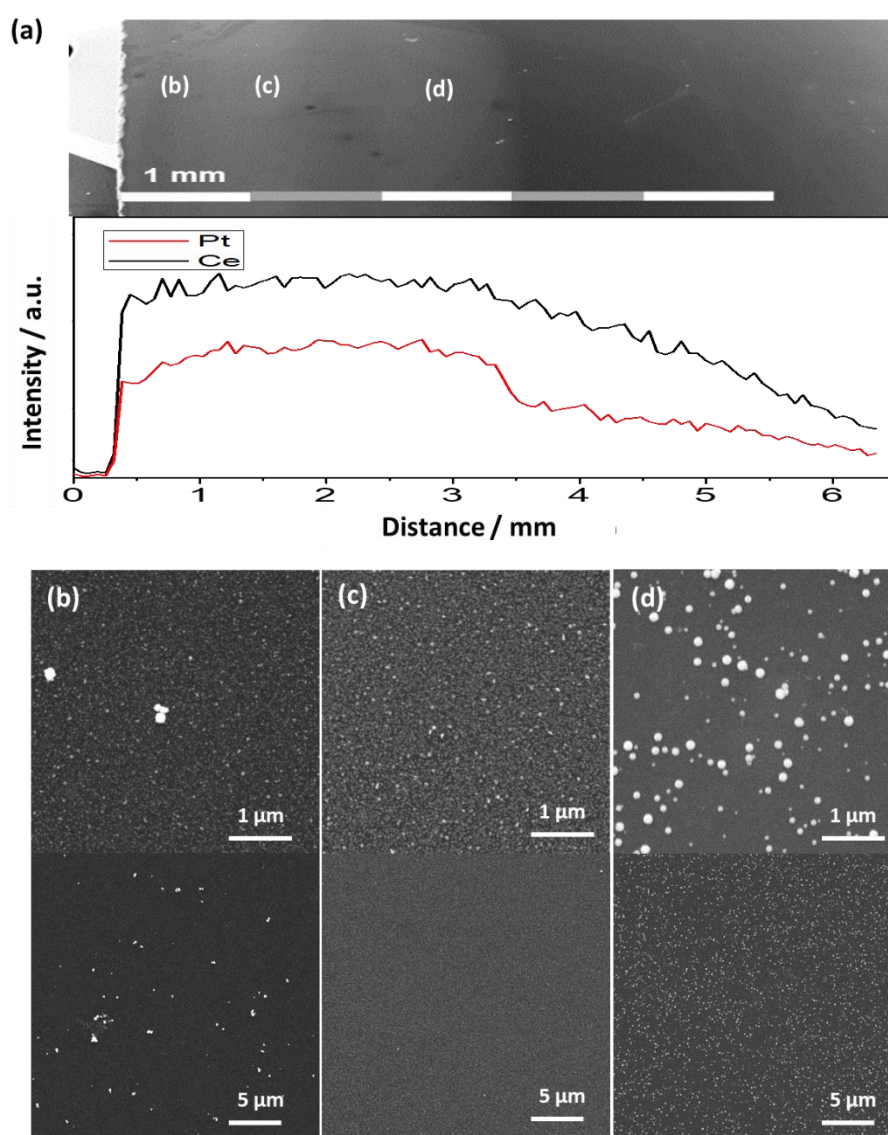


Figure 5.10 (a) SEM image and SEM-EDS line scan profiles of the Pt-CeO₂ film fabricated by using Ce(NO₃)₃ 1 mM, K₂PtCl₆ 1 mM and KNO₃ 0.1 M at applied potential 1.93 V cm⁻² for 1 min and (b-d) a higher magnification of each area of film.

In addition, the elemental composition analysis of the Pt-CeO₂ gradient film was also obtained by XPS measurement as shown in Figure 5.11(a). It demonstrates the decreasing trend of Pt content as the distance from the edge of the electrode increases. In contrast, the amount of Ce element is very low along the gradient film. However, it is worth noting that the Ce trend increases until 2 mm of distance from the electrode edge and dramatically decreases after that. These trends mean that the optimized region of the Pt combined CeO₂ should be located around 1-2 mm from the edge of the GC plate. Moreover, surface-enhanced Raman scattering (SERS) was used to analyze the Pt-CeO₂ gradient film. The SERS spectra in Figure 5.11(b) explore the Pt-CeO₂ gradient at different positions, the starting being on the edge of the electrode (Position 1) toward the middle of the electrode. The characteristic peak of CeO₂ cannot be distinguished compared to the spectra of the substrate, which is located outside of the gradient region. It might be due to the tiny amount of CeO₂ overall positions. While the characteristic peak of PtO_x is illustrated at 590 cm⁻¹. [209] The reduction trend of the PtO_x region can be noticed relating to the decrease of the number of Pt nanoparticles or the decreasing size of Pt nanoparticles along the increasing distance from the edge of the Pt-CeO₂ gradient film corresponding to SEM and XPS results. The amount of Pt seems larger compared to CeO₂ on the gradient. This can easily be explained by the fact that the reduction of Pt needs less overpotential than the water and O₂ reduction that generate the hydroxyl ions required to start the formation of CeO₂.

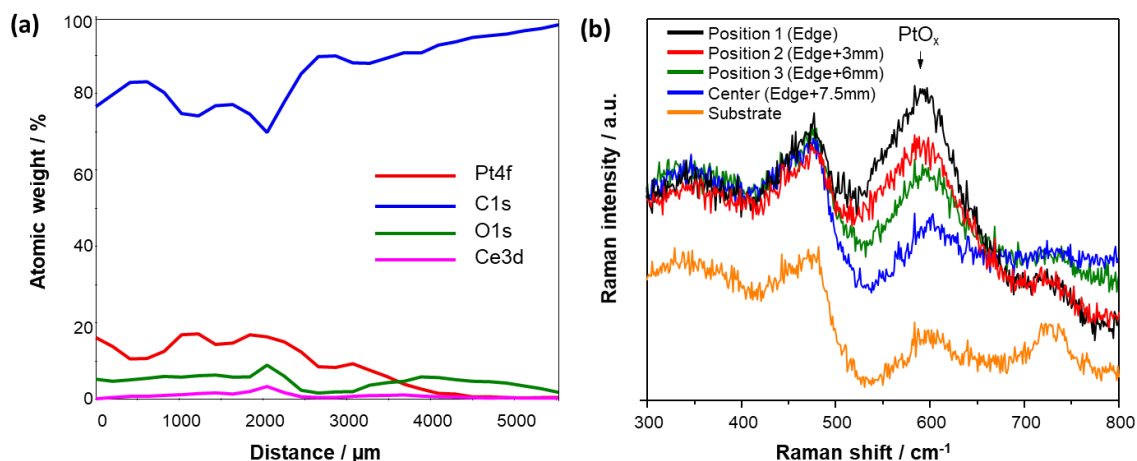


Figure 5.11 (a) Elemental analysis from XPS of the Pt-CeO₂ gradient film at different positions starting from the edge of the electrode and (b) Surface-enhanced Raman scattering (SERS) spectra of Pt-CeO₂ gradient film at different positions.

To verify the local electrochemical performance of Pt-CeO₂ gradient film, scanning electrochemical microscopy (SECM) was used in redox competition mode. In the redox competition mode, a constant potential of -0.4 V was applied to ultramicroelectrode (UME) to reduce the oxygen. Simultaneously a potential at -0.1 V was applied on the bipolar electrode to trigger the benzyl alcohol oxidation in order to consume the oxygen within the gap between UME and the substrate, as shown in Figure 5.12 SECM imaging in the redox competition mode was scanned from the electrode border ($x=0$) toward the middle of the electrode ($x=4000$) in the x -axis direction with a scan rate $50 \mu\text{m s}^{-1}$ in KOH 0.1 M solution containing BnOH 50 mM. In this particular mode, the tip and the sample compete for the same analyte. As it can be seen in Figure 5.12(b), the lower current response corresponds to the higher density of Pt combined with CeO₂ film. The active area width is around 3 mm, which is in accordance with SEM and SEM-EDS profiles. The most active area was obtained around 1-2 mm from the electrode border, implying that Pt-CeO₂ density at that position is highest according to the XPS result.

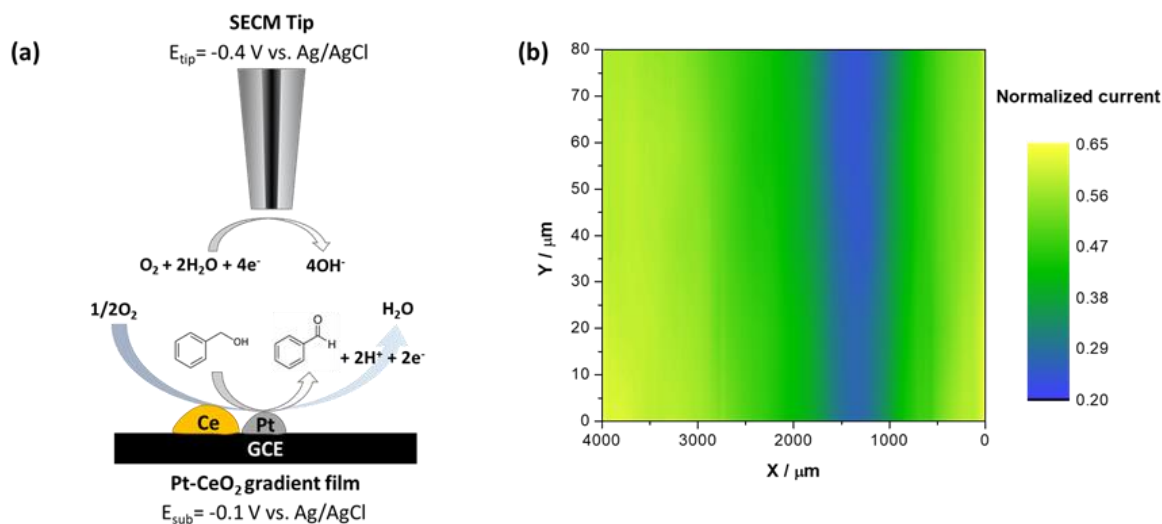


Figure 5.12 Schematic illustration of SECM measurement of Pt-CeO₂ film fabricated by using Ce(NO₃)₃ 1 mM, K₂PtCl₆ 1 mM and KNO₃ 0.1 M at applied potential 1.93 V cm⁻² for 1 min from the edge (x=0) toward the middle of the electrode (x=4000) using applied potential -0.4 V at the UME and -0.1 V at the substrate with scan rate 50 μm/s in a solution containing BnOH 50 mM and KOH 0.1 M

Further SECM investigation, the bipolar film determination was carried out using noncatalytic redox material, ferrocenedimethanol. The feedback mode was applied for SECM measurement to study the film. The potential 0.5 V was applied to the UME and 0 V on a substrate to create a redox cycle in the gap between UME and substrate. The higher current response depends on the conductive area. As can be seen in Figure 5.13, an almost homogeneous current response can be obtained, implying that every area can deliver the same performance along the Pt-CeO₂ bipolar film in the redox reaction of ferrocenedimethanol. However, a slightly different response between the electrode edge and the area inside the electrode should be influenced by the film thickness offering the difference of tip-to-sample distance. It corresponds to the film thickness obtained from the optical profilometer in Figure 5.13(c), indicating that 0.5 μm of the film thickness gradually decreases from the edge (x = 0 μm) towards the middle of the electrode until 2000 μm. The different trends of SECM mapping between electrocatalytic oxidation of benzyl alcohol and the noncatalytic reaction of ferrocenedimethanol can emphasize that Pt-CeO₂ density is the key factor for improving benzyl alcohol electrooxidation, which is not the effect of the

film thickness. Therefore, it can be noted that the different densities of Pt combined with CeO_2 film alongside the Pt- CeO_2 gradient film affect electrocatalytic performances. The SECM mapping provides the local electrochemical performance along with the gradient film delivering the optimized Pt- CeO_2 film region to verify the most active area for benzyl alcohol electrooxidation.

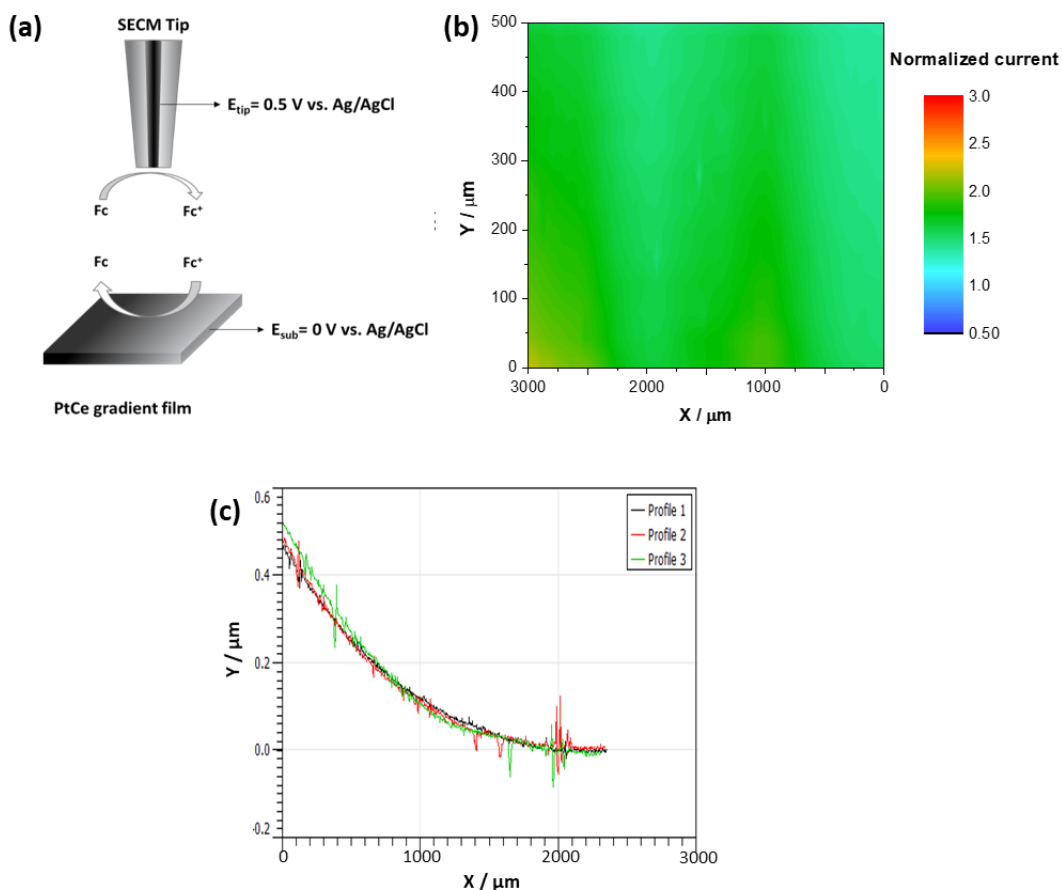


Figure 5.13 Schematic illustration of SECM measurement of the Pt- CeO_2 film fabricated by using $\text{Ce}(\text{NO}_3)_3$ 1 mM, K_2PtCl_6 1 mM and KNO_3 0.1 M at applied potential 1.93 V cm^{-2} for 1 min from the edge ($x=0$) toward the middle of the electrode ($x=3000$) using apply a potential of 0.5 V at the UME and 0 V at the substrate with scan rate $50 \mu\text{m s}^{-1}$ in solution containing ferrocenedimethanol 1 mM and KNO_3 0.1 M, and (c) Surface profiles of Pt- CeO_2 gradient film determined by optical profilometer.

5.4 Conclusion

The simultaneous cathodic electrodeposition of Pt and CeO₂ in a homogeneous film on glassy carbon electrodes was successfully performed. The electrooxidation of benzyl alcohol was realized to evaluate the electrocatalytic performance of the Pt-CeO₂ film. The homogeneous Pt-CeO₂ film demonstrates a better performance for the electrooxidation of benzyl alcohol than the films containing either CeO₂ or Pt. It also delivers better activity than the film prepared by successive electrodeposition of both compounds. This proved the existence of a synergy between two materials, indicating that the combination of the two materials can enhance the film activity in the one-step preparation of the Pt-CeO₂ film. We also successfully prepared a gradient of Pt-CeO₂ by bipolar electrochemistry. The different morphology and density due to the potential distribution along the bipolar electrode impact the film properties, leading to different local electrochemical performance. The SECM in redox competition mode allowed us to characterize the local electrochemical performance by mapping the benzyl alcohol electrooxidation of the Pt-CeO₂ gradient film. Thus, this work demonstrates that bipolar electrochemistry is a simple method to fabricate catalyst gradients and determine the optimal composition. Additionally, the SECM characterization offers an easy way to evaluate the local catalytic performance.

Chapter 6

Bifunctional Pt/Au Janus electrocatalyst for furfural electrochemical conversion

6.1 Introduction

The conversion of renewable biomass-derived compounds into high value-added chemicals is one of the most interesting issues due to the increasing energy consumption, the gradual depletion of petroleum resources, and the severe environmental problems.[213, 214] Therefore, using renewable starting compounds instead of fossil-based resources has become a potentially promising approach. Among various biomass-based compounds, furfural is a promising biomass-derived species which can be converted into several chemical products.[215, 216] In this regard, the synthesis of valuable chemicals using lignocellulose-derived furfural has attracted much attention.[213, 217] Additionally, it is an intermediate between the corresponding alcohol and acid compound. Therefore, it can be converted in both furfuryl alcohol and furoic acid via reduction and oxidation, respectively (see Figure 6.1).[218]

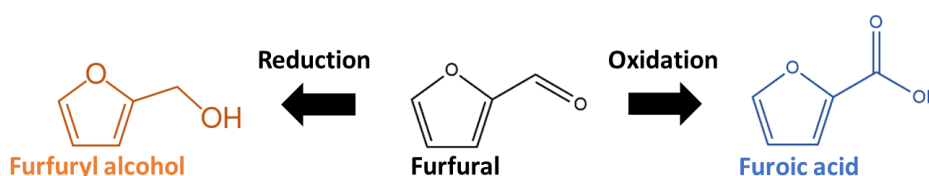


Figure 6.1 Schematic illustration of furfural conversion to furfuryl alcohol and furoic acid via reduction and oxidation reaction, respectively.

Indeed, the reduction of furfural to furfuryl alcohol, the key monomer for the synthesis of furan resins, has been widely studied. These polymers are used in various applications ranging from composites and cement to coatings and adhesives. Furfuryl alcohol is also known as an important intermediate for the production of dyes, medicine, and agricultural compounds.[219] In the typical furfuryl alcohol synthesis,

the furfural hydrogenation takes place over heterogeneous catalysts under heating and in the presence of H₂.^[220] On the other hand, electrocatalytic reduction can use the hydrogen adsorbed at the surface of the electrode (from H⁺ or H₂O) to reduce furfural. ^[221, 222] Hence, the electrochemical reaction process has some advantages as it can be carried out under mild reaction conditions, at room temperature and under atmospheric pressure without requiring additional H₂.^[223]

In addition, the oxidation of furfural to furoic acid and its derivatives, commonly utilized as pharmaceuticals, fungicides, and preservative precursors, has also been investigated.^[213] Besides that, furoic acid is considered as one of the essential compounds to produce 2,5-furan-dicarboxylic acid (FDCA), a promising renewable monomer for plastic manufacturing. Indeed, electrocatalytic oxidation of furfural offers several advantages, such as low operating temperatures and pressures, easily controllable electric potential, and a low cost oxygen source because H₂O can serve as the O-source instead of O₂ gas or other oxidants.^[214, 224]

In a conventional electrochemical process, at least two reactions occur in the system to ensure current flow. In other words, cathode and anode always provide reduction and oxidation reactions, respectively, when using a three-electrode system. Regarding this point, an interesting idea is to simultaneously use the electrochemical reduction and oxidation of furfural to synthesize the molecules of interest. Electrocatalysts have been widely used to achieve this goal.^[225-227] Typically, the electrochemical conversion of furfural has been observed simultaneously with H₂ or O₂ evolution. For example, *Y. Sun et al.* reported the design of nickel-based electrocatalysts for furfural oxidation coupled with H₂ evolution at the anode and the cathode, respectively.^[225] Additionally, in the case of the electrochemical reduction of furfural, it can take advantage of O₂ evolution at the other electrode as reported by *S. Basu* and co-workers.^[226] Interestingly, the electrochemical conversion of furfural at both anode and cathode was recently developed by *T. Noel et al.*^[227] They synthesized Cu₃P and Ni₂P on the surface of carbon fiber cloth (CFC) (Cu₃P/CFC and Ni₂P/CFC), using a vapor-phase hydrothermal method. The prepared Ni₂P/CFC and Cu₃P/CFC can be used as anode and cathode, respectively, for the simultaneous reduction and oxidation of furfural. However, to the best of our knowledge, the

development of bifunctional electrocatalytic systems for the simultaneous reduction and oxidation of furfural has not yet been demonstrated.

In theory, electrocatalysis is a fascinating approach for transforming biomass-derived intermediates because of its advantages, namely its ability to operate under ambient conditions, its versatility, and the ease of scaling up. In this context it is interesting to note that different surface coating technologies to generate bifunctional particles have been developed extensively. One of these techniques is called bipolar electrochemistry.[83] The asymmetric structure of the materials obtained by this technique is generated due to the polarization of the conductive materials induced by the applied electric field.[228] The exposed materials act in this case as bipolar electrodes. The bipolar electrode has two distinct poles on its opposite sides. Therefore, different electrochemical reactions can be carried out at the opposite extremities of the object. This means that the reduction and oxidation reactions can be performed simultaneously at the cathodic and anodic sites of the bipolar electrode, respectively. In addition, bipolar electrochemistry can be used to synthesize a bifunctional electrocatalyst by facilitating cathodic electrodeposition using the appropriate metal precursor together with a sufficiently high potential. Consequently, two-face materials, also known as Janus particles, can be obtained using this bipolar electrodeposition.

It is well-known that Janus particles, referring to the Roman god having two faces, exhibit different properties on opposite sides. Various types of micro- and nanosized particles with anisotropic properties have been reported.[229] Janus particles have unique features because they provide asymmetric chemical and physical properties on a single particle.[84, 87] We present in this study the preparation of asymmetric particles (Janus particles) composed of two electrocatalytic materials by bipolar electrochemistry. In addition, to illustrate the valuable properties of the designed materials, they have been used as asymmetric electrocatalysts to achieve the reduction of furfural at the cathodic pole and its oxidation at the anodic pole simultaneously.

6.2 Experimental section

6.2.1 Materials

All chemicals were of analytical grade and used as received without further purification. Hexachloroplatinic (IV) acid hydrate ($\text{H}_2\text{PtCl}_6 \cdot x\text{H}_2\text{O}$, Sigma-Aldrich, $\geq 99\%$), and Chloroauric acid trihydrate ($\text{HAuCl}_4 \cdot 3\text{H}_2\text{O}$, Sigma-Aldrich, $\geq 99\%$) were used as metal precursors for Pt and Au deposition, respectively. To synthesize Janus particles, spherical glassy carbon beads (630 – 1000 μm , type 2, Alfa Aesar) were used as a support material. The carbon graphite rods were used as driving electrodes for the bipolar electrochemical experiments. Potassium hydroxide (KOH, Sigma-Aldrich, $\geq 85\%$) was used as electrolyte. To carry out the electrochemical experiments, furfural (Sigma-Aldrich, $\geq 99\%$) was used as raw material. Milli-Q water (18.2 $\text{M}\Omega \text{ cm}$) was used for all experiments.

6.2.2 Method and instrumentation

6.2.2.1 Conventional three-electrode system

All experiments were performed with a potentiostat (AUTOLAB) and a conventional three-electrode system. A Pt wire and Ag/AgCl were used as the counter, and reference electrodes, respectively. Prior to all the experiments, the working electrodes were cleaned by ultrasonication in isopropanol and Milli-Q water for 15 min each time and then dried under N_2 flow. Four commercial electrodes were tested, including Pt, Au, Ni, and Cu electrodes. All the electrochemical performance tests for furfural electrochemical conversion were carried out at room temperature (25 $^\circ\text{C}$) using 50 mM KOH solution in the absence or presence of 15 mM furfural. Cyclic voltammetry was used to examine the electrocatalytic performance of each electrode with a scan rate of 20 mV/s at room temperature and ambient pressure.

6.2.2.2 Janus particle synthesis using bipolar electrodeposition

Bipolar electrodeposition was used to synthesize Janus particles composed of different metals on both sides employing an external power supply (KEITHLEY model 2450). Based on the results obtained from the CV measurements with the classic three-electrode system, Pt and Au were selected as the most appropriate materials to elaborate the Janus particles. In a first step glassy carbon beads were positioned at the center of the bipolar cell with a distance of 30 mm between the driving electrodes in a 1 mM solution of the metal precursor. Different

potentials (20, 40, 60, and 80V) were applied to optimize the deposition conditions for a fixed deposition time of 10 min. Subsequently, the prepared objects were rinsed with water and dried under N₂ flow, leading to the asymmetric particles modified with Pt or Au d on the cathodic side. In the case of Pt/Au Janus particles, Pt was deposited first on one side of the bipolar electrode, and then Au deposition was performed on the other side by switching the polarity of the driving electrodes in order to change electric field direction using the corresponding precursor solution again with a deposition time of 10 min. After that, the obtained materials were rinsed with water and dried under N₂ flow.

6.2.2.3 Furfural electrochemical conversion using bipolar electrochemistry

To investigate the electrochemical activity of the Janus particles during the electrochemical conversion of furfural, the prepared Pt/Au Janus particles were positioned at the center part of the bipolar cell, which is separated from the driving electrodes by Nafion membranes. The bipolar reaction was performed by applying the selected potential for 30 min in 50 mM of KOH solution containing 15 mM of furfural. Then, quantitative analysis was performed by using a calibration method employing high-performance liquid chromatography (HPLC) with a Shimadzu LC-2030C3D equipped with a sugar HPLC column (SP0810, 300×8 mm inner diameter) and using Milli-Q water as a mobile phase at 80 °C with a flow rate of 1 ml/min and a photodiode array (PDA) detection at 211, 245, and 276 nm for furfuryl alcohol, furoic acid, and furfural, respectively. First, the absorption peak areas of the products were integrated using Lab Solution software. Then, calibration curves (see Figure 6.2) obtained from integrated peak areas were used to calculate the electrocatalytic performance.

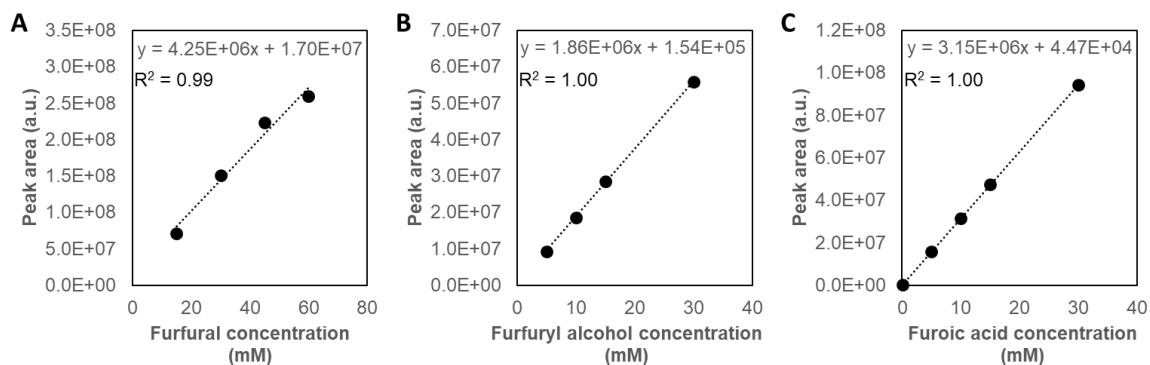


Figure 6.2 Calibration curves based on the integrated peak area obtained from HPLC measurement for (A) Furfural, (B) Furfuryl alcohol, and (C) Furoic acid.

Subsequently, the conversion of furfural (X_{FAL}) and the product selectivity (S_i) were estimated by the following equations:

$$X_{FAL} = \frac{(n_{FAL})_0 - (n_{FAL})_t}{(n_{FAL})_0} \times 100\%$$

$$S_i = \left(\frac{n_i}{(\sum n)_t} \right)$$

Where $(n_{FAL})_0$, $(n_{FAL})_t$, n_i , $\sum n$ are the initial number of moles of furfural, the number of moles of furfural at a certain time, the number of moles of the desired product i , and the total number of moles of all the products, respectively. The conservation of mass in the system was analyzed for all experiments, and the mass balance is $94.22 \pm 4.23\%$.

Additionally, scanning electron microscopy (SEM) images were obtained with a JEOL JSM-7610F microscope to study the morphology of the catalysts. The elemental analysis was carried out using SEM equipped with Energy Dispersive X-ray spectrometry (SEM-EDS).

6.3 Results and discussion

The electrocatalytic performance of different types of metals with respect to the reduction and oxidation of furfural was first investigated. Cyclic voltammetry (CV) was

used to determine the oxidation and the reduction potential of furfural to obtain the electrochemical window, which can be used for bipolar electrocatalysis. For example, as shown in Figure 6.3(A, C), the Au electrode allows furfural reduction starting at -1.3 V, while the Pt electrode doesn't give a significant signal at the same potential. A lower current density was observed for the Pt electrode when adding furfural to the solution, which might be due to molecules adsorbing at the electrode surface. To further investigate the catalytic performance of several metals, other electrodes, including Ni and Cu, were also studied, as shown in Figure 6.3(E, G). An electroactivity similar to Pt can be observed with the Ni electrode. However, for the Cu electrode, the furfural reduction starts at -1.4 V. Additionally, a characteristic peak of Cu oxidation coupled with two obvious peaks of the Cu oxide reduction at -0.8 and -1.2 V are observed.[230] From these observations, the most suitable candidate for furfural reduction is the Au electrode.

In parallel, furfural oxidation was also studied with different electrodes, as shown in Figure 6.3(B, D, F, H). Interestingly, all electrodes can promote to a certain extent furfural oxidation. Several anodic peaks are observed for the Au electrode assigned to the oxidation furfural in the potential domain between -0.2 and 0.4 V in agreement with previous studies of E.M. Belgsir and co-workers.[218] For the Pt electrode (Figure 6.3(D)), a characteristic broad peak related to furfural oxidation can be observed around 0.3 V. The other metals were also tested to examine their features (Figure 6.3(F, H)). For the Ni electrode, the current density of the classic nickel oxide peak is increasing in the presence of furfural accompanied by a slight shift of the peak position.[231] In the case of the Cu electrode, furfural oxidation can be performed from 0.2 V. Therefore, it can be concluded that the most suitable electrodes for furfural oxidation are in the following order: Pt > Cu > Au > Ni. As a global result it is therefore reasonable to use Pt for furfural oxidation and Au for its reduction.

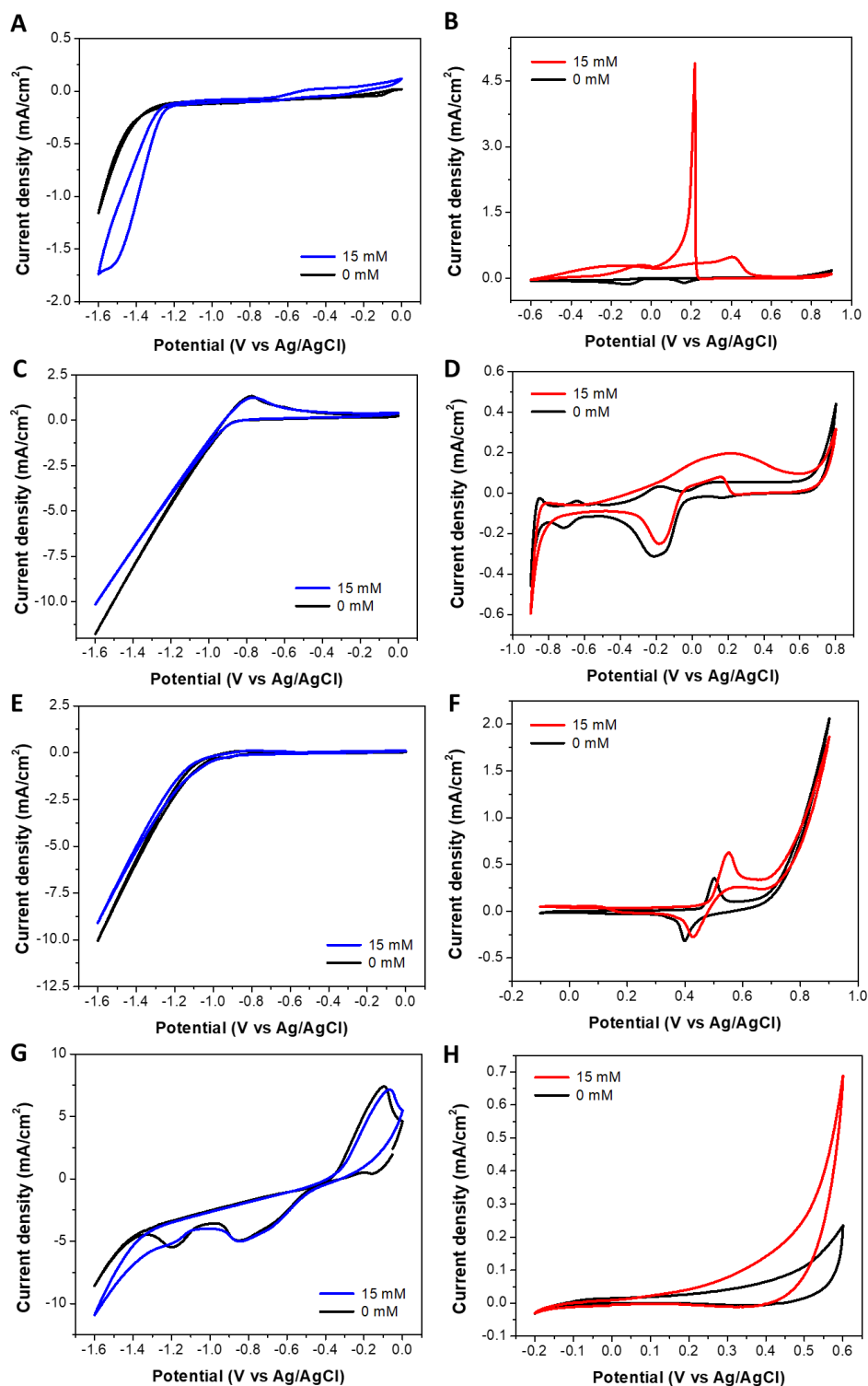


Figure 6.3 Cyclic voltammograms of (A,C,E,G) furfural electroreduction and (B,D,F,H) furfural electrooxidation at a (A-B) Au electrode, (C-D) Pt electrode, (E-F) Ni electrode and (G-H) Cu electrode, respectively, in KOH 50 mM in the absence and the presence of 15 mM furfural using a scan rate of 20 mV/s.

For further investigation, the Pt/Au Janus particles were generated using bipolar electrodeposition. In order to optimize the synthesis conditions, the impact of the potential difference between the driving electrodes was investigated. As can be seen in Figure 6.4, the most appropriate potential to deposit metal on one side of the carbon bead is 60 V with a deposition time of 10 min for both Pt and Au. It should be noted that potentials higher than 60 V are not suitable in both cases. For Pt deposition such high potentials can lead to bubble generation covering the cathodic extremity, and thus blocking Pt deposition. In contrast, for Au the deposit covers more than half of the bipolar electrode.

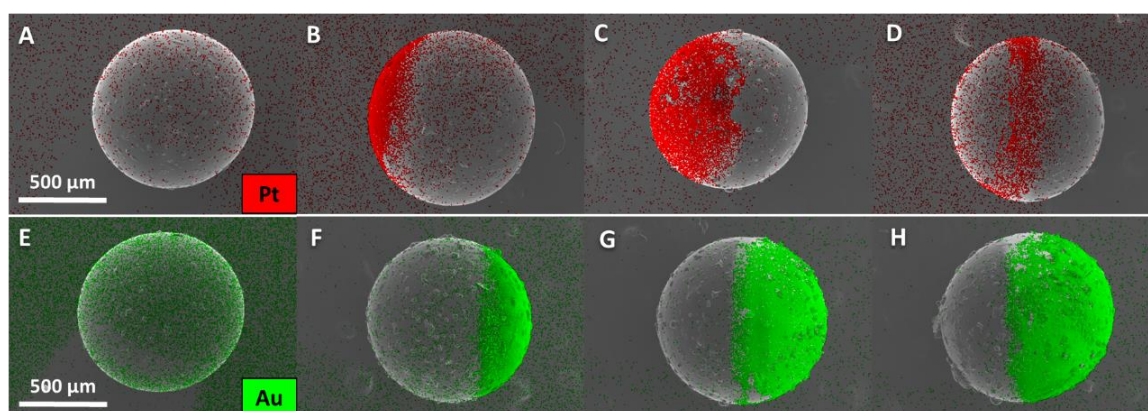


Figure 6.4 SEM-EDS images of (A-D) Pt bipolar electrodeposition at different potentials: (A) 20 V, (B) 40 V, (C) 60 V, (D) 70 V for 10 min, and (E-H) Au electrodeposition at different potentials: (E) 20 V, (F) 40 V, (G) 60 V and (H) 80 V for 10 min.

The Pt/Au Janus particles were synthesized via bipolar electrochemistry. The procedure is illustrated in Figure 6.5. Initially, the optimized potential (60 V) was applied to the bipolar cell in order to polarize the carbon beads, which were used as a support material. To deposit a metal on the support material, the electrochemical reduction of the metal source proceeds at the cathodic pole. Pt was first deposited on one side of the support material. Subsequently, the electric field was switched to the opposite direction for the Au deposition on the other side, eventually producing the Pt/Au Janus particles. Additionally, the Pt and Au deposition sequence can be changed because both elements are known to be noble metals, implying a high stability when switching the electric field direction during the Janus particle synthesis.

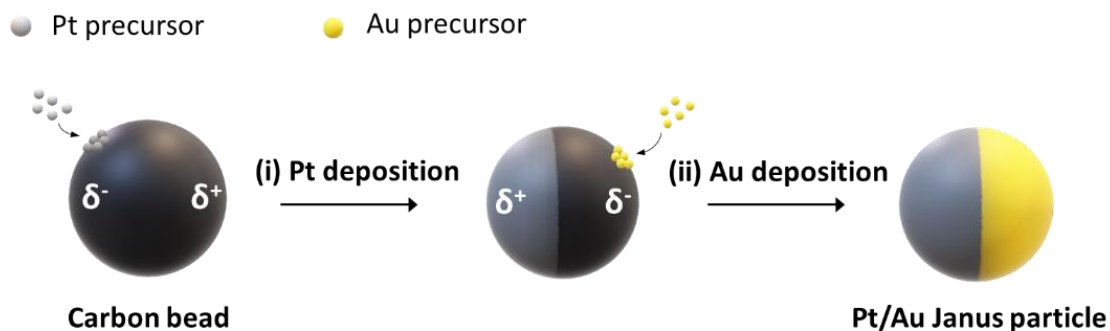


Figure 6.5 Schematic illustration of the electrodeposition process to synthesize the Pt/Au Janus particles in two steps including: (i) Pt deposition on a carbon bead and (ii) Au deposition on the opposite side by switching electric field direction.

As mentioned above, the Pt/Au Janus particles were generated by Pt deposition at 60 V for 10 min on one side of the carbon beads followed by Au deposition on the other side using 60 V for 10 min after switching the electric field direction. Then, the successfully prepared Janus particles were characterized by scanning electron microscopy and energy-dispersive X-ray spectroscopy (SEM-EDS) together with the EDS line scan profiles, as shown in Figure 6.6. Each metal is deposited on one half sphere of the carbon beads without any overlap. It should be noted that the missing EDS signal at the bottom part of the SEM-EDS images originates from the angle of orientation of the EDS detector, which cannot collect the signal hidden by the carbon bead. Thus, the entire elemental map is obtained by superposing SEM-EDS images of the two individual measurements carried out at two different angles. Additionally, the successfully deposited metals were verified each part by rotating the bead towards the detector and obtaining the EDS images.

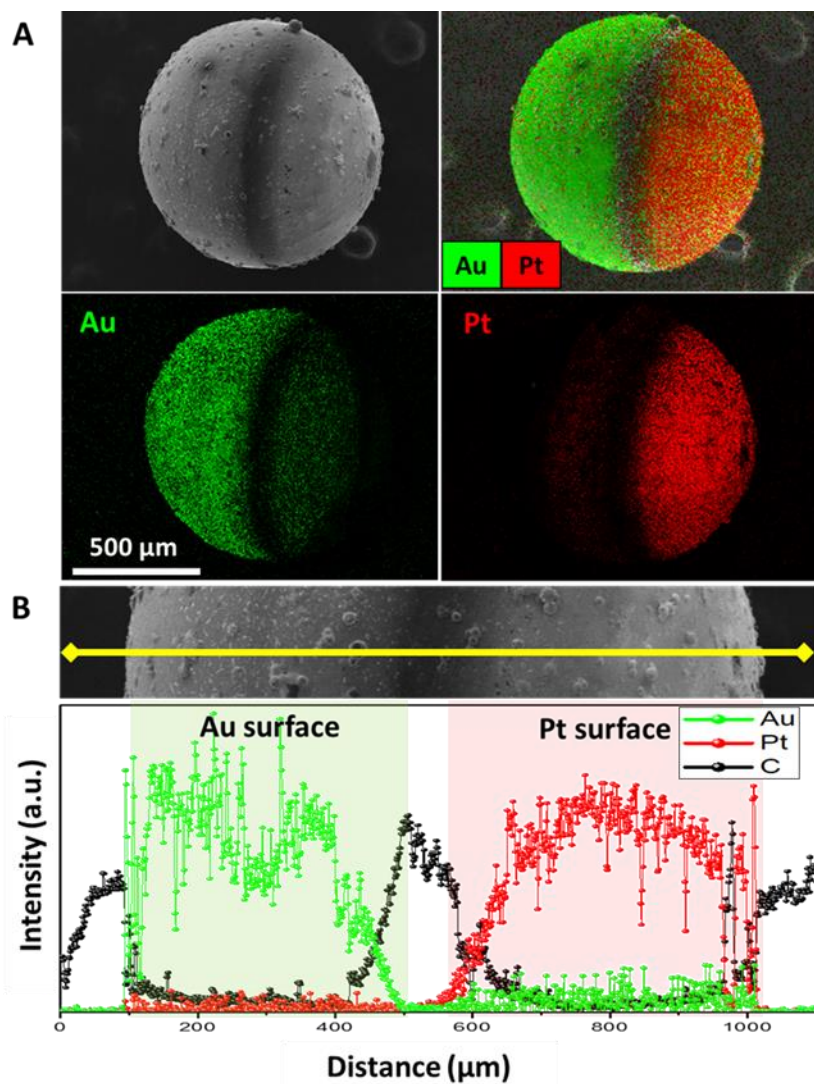


Figure 6.6 (A) SEM-EDS images and (B) SEM-EDS line scan profiles of a Pt/Au Janus particle synthesized by bipolar electrodeposition at 60 V for 10 min each side.

After the synthesis of the Pt/Au Janus particles, the electrochemical conversion of furfural was performed using bipolar electrochemistry to simultaneously produce furfural alcohol and furoic acid from furfural. The reduction of furfural to furfuryl alcohol takes place on the Au side and the oxidation of furfural to furoic acid on the Pt side, as depicted in Figure 6.7.

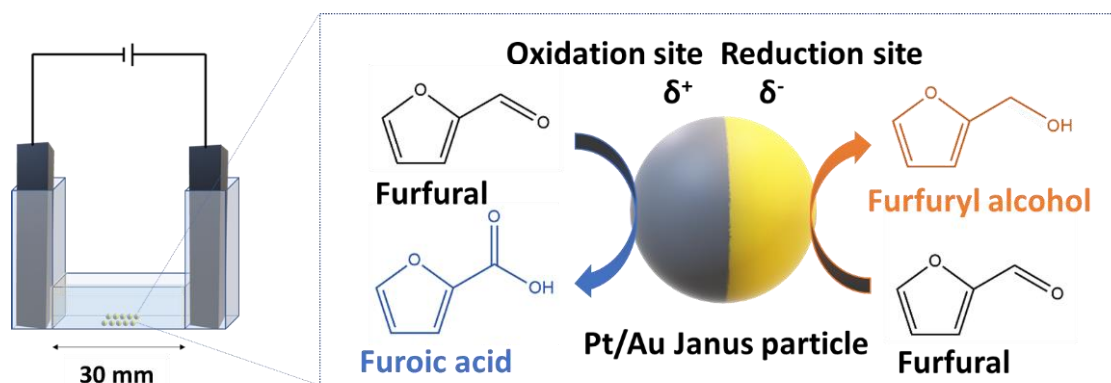


Figure 6.7 Schematic illustration of a bipolar cell coupling the two opposite furfural conversion mechanisms on a Pt/Au Janus particle.

In order for the electrocatalytic reactions to occur on the materials designed by using bipolar electrochemistry, the appropriate potential must be applied to polarize the bipolar object. The associated polarization voltage (E) is proportional to the potential window (ΔV) between the electrochemical reduction and oxidation reactions of furfural as well as the distance between the driving electrodes (d) related to the length of the bipolar electrode (l_e). E is calculated by the following equation:[86]

$$E = \frac{\Delta V}{l_e} \times d$$

The calculated potential for the bipolar electrosynthesis was 48 V. This is due to the potential window between the electrochemical oxidation of furfural on the Pt side (0.3 V) and the electrochemical reduction on the Au side (-1.3 V) coupled with the configuration of the bipolar electrochemical cell with a distance of 30 mm between the driving electrodes and the size of the beads ($l_e = \sim 1$ mm). The control experiment was performed at 48 V for 30 min with furfural but without bipolar electrodes. This experiment is used as a reference in order to take into account the effect of furfural loss during the experiment ($\sim 6\%$ loss). In contrast, the bipolar electrosynthesis reaction was carried out with a total of 24 Pt/Au Janus particles acting as bipolar electrodes at 48 V for 30 min. Interestingly, an equivalent amount of both furfuryl alcohol and furoic acid can be generated at the Pt/Au Janus particles. As can be seen in Figure 6.8(A), the selectivity for furfuryl alcohol and furoic acid is 47.8 and 52.2%, respectively, leading to a corresponding yield of 9.5 and 10.3%.

In order to analyze the total performance of the Janus Au/Pt particles in the frame of the electrosynthesis reactions, the electrocatalytic feature of each metal has been tested separately. The information on the catalytic activity is summarized in Figure 6.8(A). Furoic acid is, as expected, the main product when using Pt Janus particles, whereas the furfuryl alcohol is mostly formed with the Au Janus particle. These results again confirm the preferential oxidation and reduction on Pt and Au, respectively. In strong contrast to this, the Pt/Au Janus particles can generate both furoic acid and furfuryl alcohol simultaneously due to the preferential reactions that occur on each metal. Although only a moderate overall conversion of furfural (19.8%) was observed, this value can be easily enhanced by various factors, in particular the number of catalyst beads (see Figure 6.8(B)). To further increase the yield of both products, the number of Janus particles was increased up to 96. It was found that the efficiency of furfural conversion increases linearly with the number of Pt/Au particles. These results highlight that bipolar electrochemistry can be easily controlled and is a very valuable approach in the frame of electrocatalytic processes.

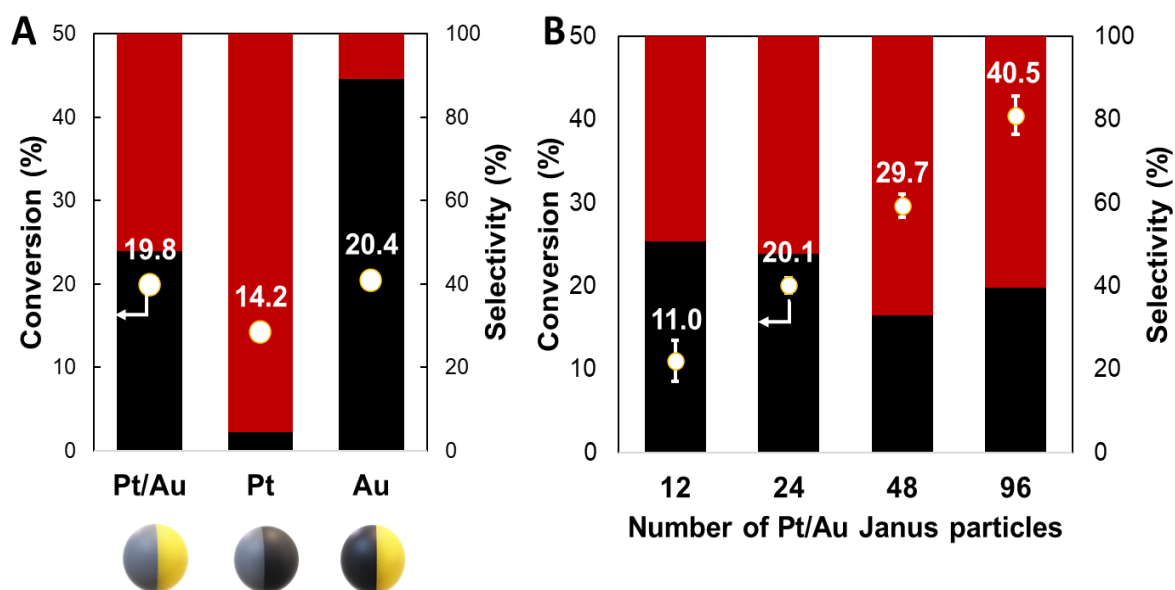


Figure 6.8 (A) Electrocatalytic performance of different Janus particles in KOH 50 mM with 15 mM of furfural using the bipolar cell with an applied potential of 48 V for 30 min. Red and black bars represent furoic acid and furfuryl alcohol selectivity, respectively, while the circle refers to the total furfural conversion.

Additional experiments were performed to verify whether the Pt/Au Janus particles were reusable. The experiments were carried out using 24 Pt/Au Janus particles. After each catalytic cycle, the Pt/Au Janus particles were recovered from the reaction mixture without any regeneration process. As shown in Figure 6.9, the Pt/Au Janus particles can be used several times with a fairly constant furfural conversion. Therefore, it is reasonable to believe that the designed Pt/Au Janus particles can be used as a bifunctional electrocatalyst for electrochemical conversion of furfural for several electrocatalytic cycles. Although a mixture of furfuryl alcohol and furoic acid was obtained after the electrocatalytic reaction, these two compounds can be easily separated due to their difference in boiling point. It is therefore not necessary to use other purification techniques. In addition, for practical applications, the process design can also be optimized. For example, the electrosynthesis might be integrated into a flow reactor in order to release each compound into separated chambers. Regarding this, the procedure should possess a liquid extraction or salting-out process, which selectively separates each product. Consequently, we will obtain the corresponding products from furfural electrochemical conversion in the separated container.

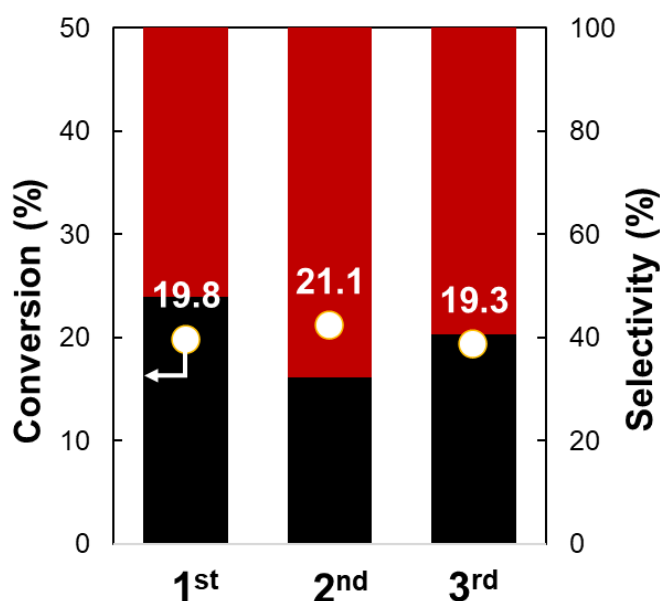


Figure 6.9 Reusability test of 24 bifunctional Pt/Au Janus particles in KOH 50 mM with 15 mM of furfural in a bipolar cell at an applied potential of 48 V for 30 min for 3 cycles. Red and black bars represent furoic acid and furfuryl alcohol selectivity, respectively, while the circle symbol refers to furfural conversion.

6.4 Conclusion

The simultaneous electrochemical conversion of furfural via both oxidation and reduction was studied as a model reaction using bipolar electrochemistry. Herein, Pt/Au Janus particles have been successfully generated using bipolar electrodeposition in order to provide the most suitable combination for furfural oxidation and reduction. Conversion of furfural into furfuryl alcohol and furoic acid can be achieved simultaneously by using Pt/Au Janus particle as bifunctional electrocatalysts. This work opens up very interesting perspectives for bipolar electrochemistry as a concept to perfectly control catalytic activity. Based on the reported proof-of-concept experiments and the obtained results, a further development for large-scale production can be envisioned, thus allowing real practical applications in the future.

Chapter 7

Conclusion and thesis perspectives

The studies performed in this thesis, were focusing on the following aspects: (i) ceria modified hierarchical zeolites for selective upgrading of ethanol dehydration to ethylene; (ii) the synergistic effect obtained by the combination of noble metal, metal oxide, and hierarchical zeolites for the selective oxidation of benzyl alcohol; (iii) the investigation of gradient films of ceria and platinum, obtained by bipolar electrochemistry, for benzyl alcohol electrooxidation using scanning electrochemical microscopy (SECM); and (iv) the design of bifunctional electrocatalysts using bipolar electrochemistry for biomass-derived compound upgrading.

In the first part, the development of a catalyst for a sustainable process to produce crucial compounds has been described. As an example, bioethanol was selectively converted to ethylene, a useful precursor for bioplastic industries. This production process derived from bio-based materials has the advantage of considering environmental and sustainable aspects. Among various catalysts, ceria (CeO_2) is one of the most promising ones owing to its abundance and its potential properties to improve catalysis efficiency. However, the bulk ceria structure is inefficient due to a low surface area, and therefore to solve this problem, we decided to disperse ceria on a solid support. Herein, we demonstrated that the use of hierarchical zeolite as solid support overcomes the drawback of conventional zeolite with respect to diffusion limitations and the accessibility of active sites. Therefore, it can be concluded that the key factors to enhance the catalytic activity are related to the accessibility of active sites and the support material properties. This context revealed that the simple fine-tuning of different factors, such as the CeO_2 insertion method, the CeO_2 quantity, and type of support material improves the catalytic performance. The CeO_2 modified hierarchical zeolite catalyst prepared by an ion-exchange method provides the best performance with a 99% yield for ethylene production. This performance is much lower for a conventional catalyst. These findings reveal the advantages of catalyst design to

accelerate the desired reaction processes. Furthermore, due to the properties of CeO₂, this CeO₂ modified catalyst can facilitate the mobility of lattice oxygen, beneficial for oxygen-related reactions. Moreover, it should be noted that the hierarchical structure of zeolite can act as a support material due to its easily optimizable properties and a high surface area. Our findings open up perspectives of using these materials for other valuable reactions involving oxygen-dependent processes.

Regarding the second research axis, CeO₂ based hierarchical zeolite catalysts have been developed for other oxygen-related reactions. As observed in the ethanol dehydration reaction, CeO₂ modified hierarchical zeolite has demonstrated the benefits of its properties, such as redox property, and oxygen mobility. The performance was further improved by combining it with other active sites such as noble metals. Platinum (Pt) was selected to be incorporated into CeO₂ and the modified hierarchical zeolite in order to enhance its catalytic performance based on a synergy effect. In this study, the selective oxidation of benzyl alcohol to benzaldehyde, which is significant for organic synthesis in academics and industry, was systematically analyzed as a model reaction for alcohol upgrading. The combination of the hydrogen adsorption capacity of Pt coupled with the oxygen mobility facilitated by CeO₂ was tested for the alcohol oxidation reaction. The performance of Pt-CeO₂ modified hierarchical zeolite with respect to the selective oxidation of benzyl alcohol with high benzaldehyde yield (~100%) again emphasizes the key role of rational catalyst design. Compared to a conventional zeolite support, the hierarchical structure reveals important benefits for the catalytic performance, among others due to the high accessibility of the active sites. Furthermore, concerning cost-effectiveness, the well-dispersed Pt on CeO₂ modified hierarchical zeolite provides high catalytic efficiency with only a small amount of Pt. Moreover, CeO₂-based materials can significantly enhance oxygen-related reactions due to their ability to facilitate oxygen mobility. Therefore, they can be applied for a wide range of reactions involving oxygen species especially biomass-derived compound upgrading.

In addition to the design of heterogeneous catalysts, the research scope was extended to electrocatalytic aspects. As we illustrated that a significant improvement can be observed for the Pt-CeO₂ modified hierarchical zeolite catalyst, we wanted to confirm the synergistic effect between Pt and CeO₂ also by using electrochemistry. An

interesting technique, namely bipolar electrochemistry, was used in this context. The principle of bipolar electrochemistry is based on a wireless configuration. There is no direct electrical contact between the bipolar electrode and driving electrodes in the electrochemical system. This generates a potential distribution along the bipolar electrode, which leads to the formation of a gradient film. The Pt-CeO₂ gradient film was directly formed using bipolar electrodeposition due to the potential drop across the bipolar electrode. Moreover, a fascinating imaging technique, SECM, was used to further identify the local electrocatalytic performance. This technique allows to study the local electrocatalytic performance of the electrocatalyst based on the interaction between a mobile ultramicroelectrode and the electrode surface at different positions. Therefore, the SECM technique was chosen to investigate the performance of the Pt-CeO₂ gradient film in the frame of benzyl alcohol oxidation. The SECM imaging reveals that the local activity of the gradient film depends on the Pt-CeO₂ composition on the surface. It offers the advantages of a facile and rapid characterization to study the electrochemical performance of non-homogeneous electrocatalysts such as multi-component electrocatalyst and multi-array electrocatalysts. Additionally, the composition of the gradient film can be easily adjusted using bipolar electrochemistry. It reveals that bipolar electrochemistry is a powerful approach to generate a gradient that helps to rapidly find the material composition with the best electrocatalytic performance.

Finally, bipolar electrochemistry was applied to the elaboration of a bifunctional electrocatalyst in the last part of the thesis. Due to the asymmetric properties of the bipolar electrode, the electrodeposition of different materials can be achieved on two opposite sides. We have shown that bipolar electrochemistry allows to synthesize Janus particles that can be used as a bifunctional electrocatalyst accelerating simultaneously reduction and oxidation reactions. In this case, electroconversion of furfural was selected as a model reaction for the upgrading of biomass-descended compounds. The transformation leads to furfuryl alcohol and furoic acid via reduction and oxidation reactions, respectively. According to the investigation, Au and Pt are suitable for the reduction and oxidation of furfural, respectively. Therefore, Pt/Au Janus particles, obtained by bipolar electrodeposition deliver, allow the simultaneous electrosynthesis of the two corresponding products, furfuryl alcohol and furoic acid, at opposite sides of the particles. This unique feature of bipolar electrochemistry paves

the way for an efficient alternative procedure to generate bifunctional catalysts and perform two crucial reactions in parallel. For the moment, two noble metals have been chosen as catalyst layers, which might impact the cost-effectiveness. Moreover, in this bipolar system, only two-dimensional arrangement can be performed at the bottom part of the bipolar cell due to the cell configuration and particle size. Thus, non-noble metals and three-dimensional arrangement with improved Janus particle size should be further studied to enhance the activity of bipolar system for practical applications.

In summary, this thesis was devoted to the development of various strategies for heterogeneous catalysis and electrocatalysis for the conversion of biomass-derived compounds. The designed materials emphasize the benefits of hierarchical zeolite structures and the synergic effects of combined materials that significantly improve the performance. Additionally, the advantages of bipolar electrochemistry allow a facile generation of gradient films and Janus electrocatalysts. Therefore, the overall results open promising perspectives for the development of environmentally friendly and sustainable processes for the valorization of biomass-derived compounds.

Amélioration de l'Utilisation de Composés Dérivés de la Biomasse en Chimie Fine

Résumé

MARISA KETKAEW

Le développement de procédés de chimie verte, utilisant des matières premières renouvelables, est un domaine de recherche en pleine expansion. En raison de la pénurie de pétrole et des préoccupations environnementales, la valorisation des composés dérivés de la biomasse est de plus en plus étudiée. Les composés issus de la biomasse sont généralement considérés comme des matières organiques renouvelables provenant de diverses sources, telles que les plantes, les déchets agricoles, les boues d'épuration et les algues. Ces composés sont considérés comme des substrats respectueux de l'environnement par opposition aux ressources en gaz naturel et en pétrole brut. Compte tenu de l'abondance de la biomasse et de ses propriétés potentielles, de nombreux produits pourraient être synthétisés. Ces produits dérivés de la biomasse auraient des applications dans divers domaines, tels que l'énergie, les cosmétiques, les parfums, les détergents et les plastiques. Par conséquent, la conception de matériaux et de processus pour convertir les composés issus de la biomasse en produits chimiques à haute valeur ajoutée est un défi important tant d'un point de vue académique qu'industriel.

Dans cette thèse, une nouvelle conception de catalyseurs hétérogènes et d'électrocatalyseurs est proposée en utilisant un oxyde métallique abondant, l'oxyde de cérium communément appelé « ceria » (CeO_2). Le ceria a été largement utilisé en catalyse en raison de ses propriétés uniques telles que ses propriétés redox et sa capacité de stockage de l'oxygène. Tout d'abord, des catalyseurs hétérogènes de zéolithes hiérarchiques modifiés ont été préparés avec succès par deux méthodes, la présynthèse et la post-synthèse. De plus, la structure hiérarchique des zéolithes a permis d'améliorer leurs performances catalytiques pour la déshydratation d'alcool. De plus, une étude électrochimique a également été réalisée pour aider au développement de processus de valorisation de la biomasse. En particulier, l'électrochimie bipolaire, a été largement étudiée en raison de ses caractéristiques particulières, telles que la possibilité de faire de l'électrochimie sans fil et de générer

une activité électrochimique asymétrique. C'est l'une des techniques électrochimiques les plus puissantes pour la conception de catalyseurs asymétriques.

Afin de surmonter l'inconvénient principal de la structure microporeuse de la zéolithe conventionnelle, qui est la limitation de la diffusion, une structure poreuse bien organisée des catalyseurs zéolithiques hiérarchiques a été conçue. Un des avantages des structures hiérarchiques est la présence de sites actifs plus exposés, ce qui peut améliorer leur efficacité catalytique. Dans ce cas, l'effet synergique entre le support en zéolithe hiérarchique et l'oxyde de cérium (CeO_2) joue un rôle important dans la déshydratation de l'éthanol en éthylène, un produit chimique à haute valeur ajoutée et un matériau clé pour les industries de production de plastique. En effet, la déshydratation catalytique de l'éthanol en éthylène, par cette méthode, est considérée comme un procédé respectueux de l'environnement, qui peut être réalisé à une température de réaction plus basse que la production traditionnelle d'éthylène par craquage thermique du gaz de pétrole ou du naphta. En utilisant la technique d'échange d'ions, la zéolithe hiérarchique modifiée par CeO_2 peut fournir de meilleures performances catalytiques (~99% du rendement en éthylène) par rapport à celle préparée par la méthode d'imprégnation. Les raisons principales de cette amélioration des performances catalytiques sont liées à l'état chimique du Ce, à l'interaction métal-support et à la réductibilité du Ce. De nombreux paramètres peuvent être facilement modifiés pour améliorer l'activité catalytique, tels que le type de matériaux de support, les méthodes de chargement en CeO_2 , la teneur en CeO_2 et le rapport Si/Al du support zéolithique, ce qui permet de stimuler la déshydratation de l'éthanol en éthylène.

Pour illustrer les bénéfices apportés par les catalyseurs préparés, l'oxydation sélective d'autres bioalcools en produits chimiques, tel que l'alcool benzylique en benzaldéhyde a été étudié. Il s'agit de l'une des voies prometteuses pour générer d'autres produits chimiques de haute valeur ajoutée. En raison de la rentabilité et des préoccupations environnementales, l'oxygène moléculaire et le CeO_2 ont respectivement été choisis comme oxydant et transporteur d'oxygène pour cette réaction. De plus, le CeO_2 possède d'autres propriétés avantageuses, il peut être utilisé à la fois comme site actif et comme matériau de support pour d'autres espèces actives. Par conséquent, la combinaison entre le métal noble, le CeO_2 et la zéolithe hiérarchique, respectivement comme site actif, promoteur et matériau de support, a

été réalisée afin d'améliorer l'activité catalytique pour l'oxydation sélective de l'alcool benzylique. L'effet du CeO_2 , qui peut favoriser la mobilité de l'oxygène dans le réseau et jouer un rôle important dans la performance catalytique, a été systématiquement étudié. L'effet synergique entre le Pt et le CeO_2 peut considérablement améliorer les performances catalytiques. Par conséquent, les rendements en benzaldéhyde ont atteint presque 100 % pour le Pt supporté sur la zéolite hiérarchique contenant du CeO_2 , alors qu'ils étaient inférieurs à 40 % en utilisant le catalyseur conventionnel. Ces observations confirment clairement que l'utilisation de la structure hiérarchique des zéolites comme matériau de support offre l'avantage d'une plus grande accessibilité du site actif. Ainsi, ces découvertes illustrent les avantages des catalyseurs synthétisés, y compris la conception structurelle couplée à des matériaux ayant une activité sélective pour améliorer leur efficacité dans les procédés de valorisation de l'alcool.

Outre la catalyse hétérogène, la fabrication d'électrocatalyseurs a également été étudiée afin d'élargir les voies de synthèse des catalyseurs. Une technique intéressante présentée dans ce manuscrit est l'électrochimie bipolaire, qui peut être décrite brièvement comme une méthode électrochimique réalisée sans connexion directe entre les objets conducteurs placés dans la solution électrolytique et les électrodes d'alimentation reliées au générateur. Elle offre divers avantages, par exemple, la possibilité de modifier de nombreuses électrodes simultanément et une polyvalence en termes de formes, tailles et modifications de matériaux. En raison du champ électrique entre les deux électrodes sources un gradient de potentiel existe dans la solution et donc le long de l'électrode bipolaire. Cela permet de former des gradients de matériaux à la surface de l'électrode bipolaire. Ainsi un gradient de Pt- CeO_2 a été synthétisé à l'aide de cette méthode. Ce film présente donc des performances, concernant l'électrooxydation de l'alcool benzylique, qui vont varier le long du gradient. Ces performances sont caractérisées par la microscopie électrochimique à balayage (SECM). La SECM est une technique d'imagerie basée sur la mesure d'un courant électrochimique circulant entre une sonde mobile (une ultramicroélectrode) et la surface qui est analysée. Cette méthode permet de repérer rapidement sur le gradient de Pt- CeO_2 quelle partie présente la meilleure activité électrocatalytique.

L'électrochimie bipolaire a également été utilisée pour élaborer des particules Janus afin de les utiliser comme électrocatalyseur bifonctionnel pour l'oxydation et la réduction simultanées d'une molécule. En effet, l'électrochimie bipolaire peut polariser un matériau conducteur afin d'y réaliser deux réactions distinctes à chacune de ses extrémités. Cette caractéristique permet de concevoir un électrocatalyseur bifonctionnel possédant deux matériaux de part et d'autre de l'électrode bipolaire. Ces composants, de nature différente peuvent contribuer simultanément à la réduction et à l'oxydation d'une espèce chimique. Pour illustrer l'approche susmentionnée, la conversion électrochimique du furfural a été choisie comme réaction modèle. Une première étude a montré que l'or (Au) et le platine (Pt) possèdent une activité électrocatalytique préférentielle par rapport à la réduction et l'oxydation du furfural. L'électrochimie bipolaire a permis dans un premier temps de les déposer à chaque extrémité de l'électrode bipolaire. Ensuite, ces particules Janus Pt/Au ont été utilisées comme électrocatalyseur bifonctionnel pour la conversion électrochimique du furfural afin de produire simultanément de l'alcool furfurylique et de l'acide furoïque. La réalisation de cet électrocatalyseur bifonctionnel Pt/Au permet également de mettre en avant les avantages de l'électrochimie bipolaire. C'est une méthode de préparation simple d'un électrocatalyseur bifonctionnel et c'est une approche qui permet de réaliser la conversion électrochimique de composé issu de la biomasse.

Par conséquent, sur la base de tous ces résultats, nous espérons que cette thèse apportera de nouvelles connaissances pour le développement de catalyseurs et d'électrocatalyseurs ainsi que des procédures de synthèse dans le cadre du développement de la chimie verte afin de produire des produits chimiques à haute valeur ajoutée à partir de la biomasse renouvelable.

Mots clés: Composés dérivés de la biomasse, Amélioration de l'alcool, Oxyde de cérium (CeO₂), zéolithes hiérarchiques, Électrochimie bipolaire, Particules Janus, Électrocatalyseur bifonctionnel

Direct Upgrading of Biomass-derived Compounds to Fine Chemicals

Summary

MARISA KETKAEW

The development of sustainable chemical production processes using renewable feedstocks is one of the most crucial research fields in Chemical Engineering, Modern Chemistry, and Sustainable Science. Because of the petroleum shortage and environmental concerns, the direct upgrading of biomass-derived compounds has gradually attracted more attention. Basically, biomass-based compounds have been generally assigned as renewable organic materials derived from various sources ranging from plants, agricultural waste, and sewage sludge to algae. These compounds are considered as environmentally friendly substrates compared to natural gas and crude oil. Based on the abundance of biomass and its potential properties, many products could be synthesized. These products derived from biomass could be used in various fields, such as energy, cosmetics, perfumes, detergents, and plastics. Therefore, the advanced design of materials and processes for converting biomass-derived compounds to high value-added chemicals is a significant challenge from both an academic and industrial point of view.

In this dissertation, a novel design of heterogeneous catalysts and electrocatalysts is proposed, based on abundant metal oxides such as cerium oxide commonly called ceria (CeO_2), which have been widely used in catalysis because of their unique properties such as the redox property and the oxygen-storage capacity. Firstly, modified hierarchical heterogeneous zeolite catalysts have been successfully prepared via two methods, the pre-synthesis, and post-synthesis modification. In addition, the benefits of the hierarchical structure of zeolites improve their catalytic performances for alcohol upgrading applications. In addition, an electrochemical study was also conducted to assist in the development of biomass valorization processes. Especially, bipolar electrochemistry, which has been extensively studied due to its original features of being a wireless electrochemical technique to generate asymmetric reactivity, is a powerful concept for asymmetric catalyst design.

For the design of hierarchical zeolite catalysts, a well-organized porous structure of zeolites has been designed to overcome its original drawback, due to the microporous structure of conventional zeolite, inducing diffusion limitations. The advantages of hierarchical structures also offer a higher amount of exposed active sites, which can enhance the catalytic efficiency. In this instance, the synergic effect between hierarchical zeolite support and ceria (CeO_2) plays an important role in ethanol dehydration to ethylene, a key material for plastic production. Indeed, the catalytic dehydration of ethanol to ethylene has been considered as an environmentally friendly process, which can be achieved at a lower reaction temperature with respect to the traditional ethylene production via thermal cracking of petroleum gas or naphtha. Using the ion-exchange technique, CeO_2 modified hierarchical zeolite can provide better catalytic performance (~99% of ethylene yield) compared to the one prepared by the impregnation method. The reasons for this improved catalytic performance relate to the chemical state of Ce, the metal-support interaction, and Ce reducibility. Numerous parameters can be easily modified to enhance the catalytic activity, such as the type of support material, CeO_2 loading methods, CeO_2 content, and the Si to Al ratio of the zeolite support, eventually boosting dehydration of ethanol to ethylene.

To illustrate the beneficial aspect of the designed catalysts, the selective oxidation of other bio-alcohols such as benzyl alcohol to benzaldehyde was studied because it is one of the promising pathways to generate valuable chemicals. Owing to cost-effectiveness and environmental concerns, molecular oxygen and CeO_2 were selected as an oxidant and an oxygen carrier for this reaction, respectively. Moreover, CeO_2 has other advantageous properties, it can be used both as an active site and as a support material for other active species. Therefore, the concept of combining noble metals, CeO_2 , and hierarchical zeolite as an active site, promoter, and support material, respectively, was adapted in order to enhance the catalytic activity for selective benzyl alcohol oxidation. The effect of CeO_2 , which can assist the lattice mobility of oxygen and play an important role in the catalytic performance, was systematically investigated. The synergetic effect between Pt and CeO_2 can considerably improve the catalytic performances. Consequently, the benzaldehyde yield reaches almost 100 % for Pt supported on CeO_2 -hierarchical zeolite, whereas it is less than 40 % when using the conventional catalyst. These observations clearly

confirm that the hierarchical structure of zeolites as support material underlines the advantages of a higher amount of accessible active sites. Thus, these discoveries illustrate the benefits of rationally designed catalysts, including a structural design coupled with selective active materials to develop their efficiency for alcohol upgrading applications.

Apart from heterogeneous catalysis, and in order to extend the scope of catalyst design, the synthesis of electrocatalysts was also investigated. An interesting technique introduced in this part is bipolar electrochemistry, which can be briefly described as an electrochemical approach performed without a direct connection between the bipolar electrode and the feeder electrodes. It can offer various advantages, such as true bulk processes due to the simultaneous modification of many electrodes and the versatility in terms of shape, size, and materials composition. Due to the wireless nature of bipolar electrochemistry, a potential gradient drops across the bipolar electrode which has been used to generate gradient films. In this contribution, a Pt-CeO₂ gradient film was elaborated based on this approach. The obtained gradient film exhibits different local performances with respect to benzyl alcohol electrooxidation, evidenced by an advanced imaging procedure based on scanning electrochemical microscopy (SECM). SECM is an imaging technique using the measurement of an electrochemical current flowing between a mobile probe (an ultramicroelectrode) and the surface being analyzed. This method allows to rapidly identify the part of the Pt-CeO₂ surface having the best electrocatalytic activity.

Bipolar electrochemistry was also employed to synthesize Janus particles in order to use them as bifunctional electrocatalysts for the simultaneous oxidation and reduction of one and the same molecule. The bipolar electrode can perform two distinct reactions at its opposite extremity and this feature allows designing a bifunctional electrocatalyst surface having two different components on each side, which can simultaneously accelerate the individual reduction and oxidation reactions. To illustrate the beneficial aspect of the above-mentioned approach, electrochemical conversion of furfural was selected as a model reaction for biomass upgrading to study the performance of this bifunctional Janus particles. According to the obtained results, gold (Au) and platinum (Pt) demonstrate a preferable electrocatalytic activity for the reduction and the oxidation of furfural, respectively. These two elements were

combined on the particles by bipolar electrodeposition. Then, the successfully prepared Pt/Au Janus particles were used as a bifunctional electrocatalyst for electrochemical furfural conversion to produce simultaneously furfuryl alcohol and furoic acid. The performance of such bifunctional Pt/Au Janus electrocatalysts highlights the advantages of bipolar electrochemistry as a straightforward approach to efficiently perform two essential electrochemical reactions simultaneously in the context of biomass conversion.

Hence, based on all these findings, we expect that this dissertation will offer novel knowledge for the development of catalysts and electrocatalysts based on concepts which can help the sustainable production of chemicals from renewable resources.

Keywords: Biomass-derived compounds, Alcohol upgrading, Cerium oxide (CeO₂), Hierarchical zeolites, Bipolar electrochemistry, Janus particles, Bifunctional electrocatalyst

References

1. Sousa ZSB, Veloso CO, Henriques CA, Teixeira da Silva V. Ethanol conversion into olefins and aromatics over HZSM-5 zeolite: Influence of reaction conditions and surface reaction studies. **Journal of Molecular Catalysis A: Chemical**. 2016;422:266-74.
2. Cimino S, Lisi L, Romanucci S. Catalysts for conversion of ethanol to butanol: Effect of acid-base and redox properties. **Catalysis Today**. 2018;304:58-63.
3. Védrine JC. Metal oxides in heterogeneous oxidation catalysis: State of the art and challenges for a more sustainable world. **ChemSusChem**. 2019;12(3):577-88.
4. Muñoz M, Heeb NV, Haag R, Honegger P, Zeyer K, Mohn J, et al. Bioethanol Blending Reduces Nanoparticle, PAH, and Alkyl- and Nitro-PAH Emissions and the Genotoxic Potential of Exhaust from a Gasoline Direct Injection Flex-Fuel Vehicle. **Environmental Science & Technology**. 2016;50(21):11853-61.
5. Inaba M, Murata K, Saito M, Takahara I. Ethanol conversion to aromatic hydrocarbons over several zeolite catalysts. **Reaction Kinetics and Catalysis Letters**. 2006;88(1):135-41.
6. Nguyen T, Le Van Mao R. Conversion of ethanol in aqueous solution over ZSM-5 zeolites: study of the reaction network. **Applied Catalysis**. 1990;58(1):119-29.
7. Makshina E, Janssens W, Sels B, Jacobs P. Catalytic study of the conversion of ethanol into 1, 3-butadiene. **Catalysis today**. 2012;198(1):338-44.
8. Takahara I, Saito M, Inaba M, Murata K. Dehydration of Ethanol into Ethylene over Solid Acid Catalysts. **Catalysis Letters**. 2005;105(3):249-52.
9. Tan TH, Scott JA, Ng YH, Taylor RA, Aguey-Zinsou K-F, Amal R. Plasmon enhanced selective electronic pathways in TiO₂ supported atomically ordered bimetallic Au-Cu alloys. **Journal of Catalysis**. 2017;352:638-48.
10. Sushkevich VL, Ivanova II, Taarning E. Ethanol conversion into butadiene over Zr-containing molecular sieves doped with silver. **Green Chemistry**. 2015;17(4):2552-9.

11. Jordison TL, Lira CT, Miller DJ. Condensed-Phase Ethanol Conversion to Higher Alcohols. **Industrial & Engineering Chemistry Research**. 2015;54(44):10991-1000.
12. Salem HM, Mohamed RS, Alkahlawy AA, Gobara HM, Hassan AEA, Hassan SA. Enhanced ethylene production by dehydration of ethanol over Al/SBA-15 mesoporous catalysts. **Journal of Porous Materials**. 2019;26(3):735-45.
13. DeWilde JF, Chiang H, Hickman DA, Ho CR, Bhan A. Kinetics and Mechanism of Ethanol Dehydration on γ -Al₂O₃: The Critical Role of Dimer Inhibition. **ACS Catalysis**. 2013;3(4):798-807.
14. Clemente MCH, Martins GAV, de Freitas EF, Dias JA, Dias SCL. Ethylene production via catalytic ethanol dehydration by 12-tungstophosphoric acid@ceria-zirconia. **Fuel**. 2019;239:491-501.
15. Ferreira Madeira F, Ben Tayeb K, Pinard L, Vezin H, Maury S, Cadran N. Ethanol transformation into hydrocarbons on ZSM-5 zeolites: Influence of Si/Al ratio on catalytic performances and deactivation rate. Study of the radical species role. **Applied Catalysis A: General**. 2012;443-444:171-80.
16. Wynblatt P, Gjostein N. Supported metal crystallites. **Progress in solid state chemistry**. 1975;9:21-58.
17. Dai R, Zheng Z, Lian C, Li X, Wu X, An X, et al. A high-performance CeO₂@Pt-Beta yolk-shell catalyst used in low-temperature ethanol steam reforming for high-purity hydrogen production. **International Journal of Energy Research**. 2019;43(6):2075-85.
18. Montini T, Melchionna M, Monai M, Fornasiero P. Fundamentals and catalytic applications of CeO₂-based materials. **Chemical reviews**. 2016;116(10):5987-6041.
19. Trovarelli A. Catalytic properties of ceria and CeO₂-containing materials. **Catalysis Reviews**. 1996;38(4):439-520.
20. Kašpar J, Fornasiero P, Graziani M. Use of CeO₂-based oxides in the three-way catalysis. **Catalysis Today**. 1999;50(2):285-98.
21. Li X-G, Liu C, Sun J, Xian H, Tan Y-S, Jiang Z, et al. Tuning interactions between zeolite and supported metal by physical-sputtering to achieve higher catalytic performances. **Scientific Reports**. 2013;3:2813.

22. Lu J, Martinez-Macias C, Aydin C, Browning ND, Gates BC. Zeolite-supported bimetallic catalyst: controlling selectivity of rhodium complexes by nearby iridium complexes. **Catalysis Science & Technology**. 2013;3(9):2199-203.
23. Liu Z, Hua Y, Wang J, Dong X, Tian Q, Han Y. Recent progress in the direct synthesis of hierarchical zeolites: synthetic strategies and characterization methods. **Materials Chemistry Frontiers**. 2017;1(11):2195-212.
24. Sedighi M, Rostami AA, Alizadeh E. Enhanced electro-oxidation of ethanol using Pt–CeO₂ electrocatalyst prepared by electrodeposition technique. **International Journal of Hydrogen Energy**. 2017;42(8):4998-5005.
25. Verboekend D, Pérez-Ramírez J. Design of hierarchical zeolite catalysts by desilication. **Catalysis Science & Technology**. 2011;1(6):879-90.
26. Dell'Anna MM, Mali M, Mastroilli P, Cotugno P, Monopoli A. Oxidation of benzyl alcohols to aldehydes and ketones under air in water using a polymer supported palladium catalyst. **Journal of Molecular Catalysis A: Chemical**. 2014;386:114-9.
27. Vu HX, Armbruster U, Martin A. Micro/Mesoporous Zeolitic Composites: Recent Developments in Synthesis and Catalytic Applications. **Catalysts**. 2016;6(12).
28. Moshoeshe M, Nadiye-Tabbiruka MS, Obuseng V. A Review of the Chemistry, Structure, Properties and Applications of Zeolites. **American Journal of Materials Science**. 2017;7(5):196-221.
29. Moliner M, Martínez C, Corma A. Multipore Zeolites: Synthesis and Catalytic Applications. **Angewandte Chemie International Edition**. 2015;54(12):3560-79.
30. Ivanova II, Knyazeva EE. Micro–mesoporous materials obtained by zeolite recrystallization: synthesis, characterization and catalytic applications. **Chemical Society Reviews**. 2013;42(9):3671-88.
31. Zhang K, Ostraat ML. Innovations in hierarchical zeolite synthesis. **Catal Today**. 2016;264(Supplement C):3-15.
32. Feliczak-Guzik A. Hierarchical zeolites: Synthesis and catalytic properties. **Microporous and Mesoporous Materials**. 2018;259:33-45.
33. Hartmann M, Machoke AG, Schwieger W. Catalytic test reactions for the evaluation of hierarchical zeolites. **Chemical Society Reviews**. 2016;45(12):3313-30.

34. Pérez-Ramírez J, Christensen CH, Egeblad K, Christensen CH, Groen JC. Hierarchical zeolites: enhanced utilisation of microporous crystals in catalysis by advances in materials design. **Chemical Society Reviews**. 2008;37(11):2530-42.
35. Ennaert T, Van Aelst J, Dijkmans J, De Clercq R, Schutyser W, Dusselier M, et al. Potential and challenges of zeolite chemistry in the catalytic conversion of biomass. **Chemical Society Reviews**. 2016;45(3):584-611.
36. Sun C, Du J, Liu J, Yang Y, Ren N, Shen W, et al. A facile route to synthesize durable mesopore containing ZSM-5 catalyst for methanol to propylene reaction. **Chemical Communications**. 2010;46(15):2671-3.
37. Li K, Valla J, Garcia-Martinez J. Realizing the Commercial Potential of Hierarchical Zeolites: New Opportunities in Catalytic Cracking. **ChemCatChem**. 2014;6(1):46-66.
38. Schmidt I, Boisen A, Gustavsson E, Ståhl K, Pehrson S, Dahl S, et al. Carbon Nanotube Templated Growth of Mesoporous Zeolite Single Crystals. **Chemistry of Materials**. 2001;13(12):4416-8.
39. Chen H, Wydra J, Zhang X, Lee P-S, Wang Z, Fan W, et al. Hydrothermal Synthesis of Zeolites with Three-Dimensionally Ordered Mesoporous-Imprinted Structure. **Journal of the American Chemical Society**. 2011;133(32):12390-3.
40. Ryoo R, Joo SH, Kruk M, Jaroniec M. Ordered Mesoporous Carbons. **Advanced Materials**. 2001;13(9):677-81.
41. Holland BT, Abrams L, Stein A. Dual Templating of Macroporous Silicates with Zeolitic Microporous Frameworks. **Journal of the American Chemical Society**. 1999;121(17):4308-9.
42. García-Martínez J, Johnson M, Valla J, Li K, Ying JY. Mesostructured zeolite Y—high hydrothermal stability and superior FCC catalytic performance. **Catalysis Science & Technology**. 2012;2(5):987-94.
43. Zhou J, Hua Z, Liu Z, Wu W, Zhu Y, Shi J. Direct Synthetic Strategy of Mesoporous ZSM-5 Zeolites by Using Conventional Block Copolymer Templates and the Improved Catalytic Properties. **ACS Catalysis**. 2011;1(4):287-91.

44. Cho K, Cho HS, de Ménorval L-C, Ryoo R. Generation of Mesoporosity in LTA Zeolites by Organosilane Surfactant for Rapid Molecular Transport in Catalytic Application. **Chemistry of Materials**. 2009;21(23):5664-73.
45. Shanbhag GV, Choi M, Kim J, Ryoo R. Mesoporous sodalite: A novel, stable solid catalyst for base-catalyzed organic transformations. **Journal of Catalysis**. 2009;264(1):88-92.
46. Kim J, Park W, Ryoo R. Surfactant-Directed Zeolite Nanosheets: A High-Performance Catalyst for Gas-Phase Beckmann Rearrangement. **ACS Catalysis**. 2011;1(4):337-41.
47. Möller K, Bein T. Mesoporosity – a new dimension for zeolites. **Chemical Society Reviews**. 2013;42(9):3689-707.
48. Michalkiewicz B, Koren ZC. Zeolite membranes for hydrogen production from natural gas: state of the art. **J Porous Mater**. 2015;22(3):635-46.
49. Rosso I, Galletti C, Saracco G, Garrone E, Specchia V. Development of A zeolites-supported noble-metal catalysts for CO preferential oxidation: H₂ gas purification for fuel cell. **Applied Catalysis B: Environmental**. 2004;48(3):195-203.
50. Rubio-Marqués P, Rivero-Crespo MA, Leyva-Pérez A, Corma A. Well-Defined Noble Metal Single Sites in Zeolites as an Alternative to Catalysis by Insoluble Metal Salts. **Journal of the American Chemical Society**. 2015;137(36):11832-7.
51. Freyschlag CG, Madix RJ. Precious metal magic: catalytic wizardry. **Materials Today**. 2011;14(4):134-42.
52. Zhang Y, Jiang H, Wang Y, Zhang M. Synthesis of highly dispersed ruthenium nanoparticles supported on activated carbon via supercritical fluid deposition. **Industrial & Engineering Chemistry Research**. 2014;53(15):6380-7.
53. Murthy S, Effiong P, Fei CC. **11 - Metal oxide nanoparticles in biomedical applications**. In: Al-Douri Y, editor. *Metal Oxide Powder Technologies*: Elsevier; 2020. p. 233-51.
54. Sun Y-F, Liu S-B, Meng F-L, Liu J-Y, Jin Z, Kong L-T, et al. Metal oxide nanostructures and their gas sensing properties: a review. **Sensors (Basel)**. 2012;12(3):2610-31.

55. Masikini M, Chowdhury M, Nemraoui O. Metal oxides: Application in exhaled breath acetone chemiresistive sensors. **Journal of The Electrochemical Society**. 2020;167(3):037537.
56. Védrine JC. Heterogeneous Catalysis on Metal Oxides. **Catalysts**. 2017;7(11).
57. Wang R, Wu J. **5 - Structure and Basic Properties of Ternary Metal Oxides and Their Prospects for Application in Supercapacitors**. In: Dubal DP, Gomez-Romero P, editors. *Metal Oxides in Supercapacitors*: Elsevier; 2017. p. 99-132.
58. Miyazawa T, Tanabe Y, Nakamura I, Shinke Y, Hiza M, Choe Y-K, et al. Fundamental roles of ZnO and ZrO₂ in the conversion of ethanol to 1, 3-butadiene over ZnO–ZrO₂/SiO₂. **Catalysis Science & Technology**. 2020;10(22):7531-41.
59. Liu Y, Deng J, Xie S, Wang Z, Dai H. Catalytic removal of volatile organic compounds using ordered porous transition metal oxide and supported noble metal catalysts. **Chinese Journal of Catalysis**. 2016;37(8):1193-205.
60. Wang W, Anderson CF, Wang Z, Wu W, Cui H, Liu C-J. Peptide-templated noble metal catalysts: syntheses and applications. **Chemical science**. 2017;8(5):3310-24.
61. Ilyas M, Sadiq M. Liquid-Phase Aerobic Oxidation of Benzyl Alcohol Catalyzed by Pt/ZrO₂. **Chemical Engineering & Technology: Industrial Chemistry-Plant Equipment-Process Engineering-Biotechnology**. 2007;30(10):1391-7.
62. Mallat T, Bodnar Z, Hug P, Baiker A. Selective oxidation of cinnamyl alcohol to cinnamaldehyde with air over Bi-Pt/alumina catalysts. **Journal of Catalysis**. 1995;153(1):131-43.
63. Bavykin DV, Lapkin AA, Plucinski PK, Torrente-Murciano L, Friedrich JM, Walsh FC. Deposition of Pt, Pd, Ru and Au on the surfaces of titanate nanotubes. **Topics in Catalysis**. 2006;39(3-4):151-60.
64. Peng R, Li S, Sun X, Ren Q, Chen L, Fu M, et al. Size effect of Pt nanoparticles on the catalytic oxidation of toluene over Pt/CeO₂ catalysts. **Applied Catalysis B: Environmental**. 2018;220:462-70.
65. Wang X, Liu D, Song S, Zhang H. Pt@ CeO₂ multicore@ shell self-assembled nanospheres: clean synthesis, structure optimization, and catalytic

- applications. **Journal of the American Chemical Society**. 2013;135(42):15864-72.
66. Carrettin S, Concepción P, Corma A, Lopez Nieto JM, Puentes VF. Nanocrystalline CeO₂ increases the activity of Au for CO oxidation by two orders of magnitude. **Angewandte Chemie International Edition**. 2004;43(19):2538-40.
67. Hosokawa S, Hayashi Y, Imamura S, Wada K, Inoue M. Effect of the preparation conditions of Ru/CeO₂ catalysts for the liquid phase oxidation of benzyl alcohol. **Catalysis letters**. 2009;129(3-4):394-9.
68. Singha R, Shukla A, Yadav A, Sasaki T, Sandupatla A, Deo G, et al. Pt–CeO₂ nanoporous spheres—an excellent catalyst for partial oxidation of methane: effect of the bimodal pore structure. **Catalysis Science & Technology**. 2017;7(20):4720-35.
69. Hong Y, Yan X, Liao X, Li R, Xu S, Xiao L, et al. Platinum nanoparticles supported on Ca (Mg)-zeolites for efficient room-temperature alcohol oxidation under aqueous conditions. **Chemical Communications**. 2014;50(68):9679-82.
70. Langa S, Nyamunda BC, Heveling J. Antimony-Modified Platinum Catalysts for the Selective and Stable Oxidation of Cinnamyl Alcohol with Hydrogen Peroxide. **Catalysis Letters**. 2016;146(4):755-62.
71. Roduner E. Understanding catalysis. **Chemical Society Reviews**. 2014;43(24):8226-39.
72. Yu K, Lou L-L, Liu S, Zhou W. Asymmetric Oxygen Vacancies: the Intrinsic Redox Active Sites in Metal Oxide Catalysts. **Advanced Science**. 2020;7(2):1901970.
73. Liu H, Zhou Y, Zhang Y, Bai L, Tang M. Effect of Preparation Processes on Catalytic Performance of PtSnNa/ZSM-5 for Propane Dehydrogenation. **Ind Eng Chem Res**. 2009;48(12):5598-603.
74. Fuku K, Goto M, Kamegawa T, Mori K, Yamashita H. Highly Efficient Thermal Decomposition of Volatile Organic Compounds by Pt/CeO₂/ZSM-5. **Bull Chem Soc Jpn**. 2011;84(9):979-81.
75. Damyanova S, Bueno JMC. Effect of CeO₂ loading on the surface and catalytic behaviors of CeO₂-Al₂O₃-supported Pt catalysts. **Applied Catalysis A: General**. 2003;253(1):135-50.

76. Santos ACSF, Damyanova S, Teixeira GNR, Mattos LV, Noronha FB, Passos FB, et al. The effect of ceria content on the performance of Pt/CeO₂/Al₂O₃ catalysts in the partial oxidation of methane. **Applied Catalysis A: General**. 2005;290(1):123-32.
77. Xu C, Shen PK. Electrochemical oxidation of ethanol on Pt-CeO₂/C catalysts. **Journal of Power Sources**. 2005;142(1-2):27-9.
78. Wang J, Xi J, Bai Y, Shen Y, Sun J, Chen L, et al. Structural designing of Pt-CeO₂/CNTs for methanol electro-oxidation. **Journal of Power Sources**. 2007;164(2):555-60.
79. Huang S-Y, Chang C-M, Yeh C-T. Promotion of platinum–ruthenium catalyst for electro-oxidation of methanol by ceria. **Journal of Catalysis**. 2006;241(2):400-6.
80. Cordeiro GL, de Camargo EF, Santos MC, Pereira CV, Ussui V, de Lima NB, et al. Improved Pt/CeO₂ Electrocatalysts for Ethanol Electro-oxidation. **Int J Electrochem Sci**. 2018;13:6388-401.
81. Qin B, Yu H, Chi J, Jia J, Gao X, Yao D, et al. A novel Ir/CeO₂-C nanoparticle electrocatalyst for the hydrogen oxidation reaction of alkaline anion exchange membrane fuel cells. **RSC Advances**. 2017;7(50):31574-81.
82. He Q, Mukerjee S, Shyam B, Ramaker D, Parres-Esclapez S, Illán-Gómez M, et al. Promoting effect of CeO₂ in the electrocatalytic activity of rhodium for ethanol electro-oxidation. **Journal of Power Sources**. 2009;193(2):408-15.
83. Loget G, Roche J, Kuhn A. True bulk synthesis of Janus objects by bipolar electrochemistry. **Advanced materials**. 2012;24(37):5111-6.
84. Loget G, Kuhn A. Bulk synthesis of Janus objects and asymmetric patchy particles. **Journal of Materials Chemistry**. 2012;22(31):15457-74.
85. Shida N, Zhou Y, Inagi S. Bipolar electrochemistry: A powerful tool for electrifying functional material synthesis. **Accounts of chemical research**. 2019;52(9):2598-608.
86. Fosdick SE, Knust KN, Scida K, Crooks RM. Bipolar electrochemistry. **Angewandte Chemie International Edition**. 2013;52(40):10438-56.
87. Kumsapaya C, Bakai M-F, Loget G, Goudeau B, Warakulwit C, Limtrakul J, et al. Wireless Electrografting of Molecular Layers for Janus Particle Synthesis. **Chemistry – A European Journal**. 2013;19(5):1577-80.

88. Fattah ZA, Bouffier L, Kuhn A. Indirect bipolar electrodeposition of polymers for the controlled design of zinc microswimmers. **Applied Materials Today**. 2017;9:259-65.
89. Liu R, Zhang C, Liu M. Open bipolar electrode-electrochemiluminescence imaging sensing using paper-based microfluidics. **Sensors and Actuators B: Chemical**. 2015;216:255-62.
90. Tisserant G, Fattah Z, Ayela C, Roche J, Plano B, Zigah D, et al. Generation of metal composition gradients by means of bipolar electrodeposition. **Electrochimica Acta**. 2015;179:276-81.
91. Koefoed L, Pedersen SU, Daasbjerg K. Bipolar electrochemistry—A wireless approach for electrode reactions. **Current Opinion in Electrochemistry**. 2017;2(1):13-7.
92. Velmurugan J, Agrawal A, An S, Choudhary E, Szalai VA. Fabrication of Scanning Electrochemical Microscopy-Atomic Force Microscopy Probes to Image Surface Topography and Reactivity at the Nanoscale. **Analytical Chemistry**. 2017;89(5):2687-91.
93. Kai T, Zoski CG, Bard AJ. Scanning electrochemical microscopy at the nanometer level. **Chemical Communications**. 2018;54(16):1934-47.
94. Bard AJ, Fan FRF, Kwak J, Lev O. Scanning electrochemical microscopy. Introduction and principles. **Analytical Chemistry**. 1989;61(2):132-8.
95. Ballesteros Katemann B, Schulte A, Schuhmann W. Constant-Distance Mode Scanning Electrochemical Microscopy (SECM)—Part I: Adaptation of a Non-Optical Shear-Force-Based Positioning Mode for SECM Tips. **Chemistry – A European Journal**. 2003;9(9):2025-33.
96. Bard AJ, Mirkin MV. **Scanning electrochemical microscopy**: CRC Press; 2001.
97. Ummadi JG, Joshi VS, Gupta PR, Indra AK, Koley D. Single-cell migration as studied by scanning electrochemical microscopy. **Analytical Methods**. 2015;7(20):8826-31.
98. Wain AJ, Cox D, Zhou S, Turnbull A. High-aspect ratio needle probes for combined scanning electrochemical microscopy — Atomic force microscopy. **Electrochemistry Communications**. 2011;13(1):78-81.
99. Preet A, Lin T-E. A review: Scanning electrochemical microscopy (secm) for visualizing the real-time local catalytic activity. **Catalysts**. 2021;11(5):594.

100. Mayer FD, Hosseini-Benhangi P, Sánchez-Sánchez CM, Asselin E, Gyenge EL. Scanning electrochemical microscopy screening of CO₂ electroreduction activities and product selectivities of catalyst arrays. **Communications Chemistry**. 2020;3(1):1-9.
101. Zimmermann H, Walzl R. Ethylene. **Ullmann's Encyclopedia of Industrial Chemistry**. 2000.
102. Matar S, Hatch LF. **Chemistry of petrochemical processes**: Elsevier; 2001.
103. Mohsenzadeh A, Zamani A, Taherzadeh MJ. Bioethylene production from ethanol: A review and techno-economical evaluation. **ChemBioEng Reviews**. 2017;4(2):75-91.
104. Froment GF. Thermal cracking for olefins production. Fundamentals and their application to industrial problems. **Chemical Engineering Science**. 1981;36(8):1271-82.
105. Sundaram KM, Shreehan MM, Olszewski EF. Ethylene. **Kirk-Othmer Encyclopedia of Chemical Technology**. 2000.
106. Zhang M, Yu Y. Dehydration of ethanol to ethylene. **Industrial & Engineering Chemistry Research**. 2013;52(28):9505-14.
107. Bedia J, Barrionuevo R, Rodríguez-Mirasol J, Cordero T. Ethanol dehydration to ethylene on acid carbon catalysts. **Applied Catalysis B: Environmental**. 2011;103(3):302-10.
108. Xia W, Wang F, Mu X, Chen K, Takahashi A, Nakamura I, et al. Catalytic performance of H-ZSM-5 zeolites for conversion of ethanol or ethylene to propylene: Effect of reaction pressure and SiO₂/Al₂O₃ ratio. **Catalysis Communications**. 2017;91:62-6.
109. Fan X, Jiao Y. **Chapter 5 - Porous Materials for Catalysis: Toward Sustainable Synthesis and Applications of Zeolites**. In: Szekely G, Livingston A, editors. Sustainable Nanoscale Engineering: Elsevier; 2020. p. 115-37.
110. Salakhum S, Yutthalekha T, Chareonpanich M, Limtrakul J, Wattanakit C. Synthesis of hierarchical faujasite nanosheets from corn cob ash-derived nanosilica as efficient catalysts for hydrogenation of lignin-derived alkylphenols. **Microporous and Mesoporous Materials**. 2018;258:141-50.

111. Chaikittisilp W, Suzuki Y, Mukti RR, Suzuki T, Sugita K, Itabashi K, et al. Formation of hierarchically organized zeolites by sequential intergrowth. **Angewandte Chemie**. 2013;125(12):3439-43.
112. Wu L, Degirmenci V, Magusin PCMM, Szyja BM, Hensen EJM. Dual template synthesis of a highly mesoporous SSZ-13 zeolite with improved stability in the methanol-to-olefins reaction. **Chemical Communications**. 2012;48(76):9492-4.
113. Xin H, Li X, Fang Y, Yi X, Hu W, Chu Y, et al. Catalytic dehydration of ethanol over post-treated ZSM-5 zeolites. **Journal of Catalysis**. 2014;312:204-15.
114. Shetsiri S, Thivasasith A, Saenluang K, Wannapakdee W, Salakhum S, Wetchasat P, et al. Sustainable production of ethylene from bioethanol over hierarchical ZSM-5 nanosheets. **Sustainable Energy & Fuels**. 2019;3(1):115-26.
115. Liu B, Yu S, Wang Q, Hu W, Jing P, Liu Y, et al. Hollow mesoporous ceria nanoreactors with enhanced activity and stability for catalytic application. **Chemical Communications**. 2013;49(36):3757-9.
116. Zhang C, Li S, Wang T, Wu G, Ma X, Gong J. Pt-based core-shell nanocatalysts with enhanced activity and stability for CO oxidation. **Chemical Communications**. 2013;49(90):10647-9.
117. Hayashi F, Iwamoto M. Yttrium-Modified Ceria As a Highly Durable Catalyst for the Selective Conversion of Ethanol to Propene and Ethene. **ACS Catalysis**. 2013;3(1):14-7.
118. Li J, Zeng P, Zhao L, Ren S, Guo Q, Zhao H, et al. Tuning of acidity in CeY catalytic cracking catalysts by controlling the migration of Ce in the ion exchange step through valence changes. **Journal of Catalysis**. 2015;329:441-8.
119. Ketkaew M, Suttipat D, Kidkhunthod P, Witoon T, Wattanakit C. Nanoceria-modified platinum supported on hierarchical zeolites for selective alcohol oxidation. **RSC Advances**. 2019;9(62):36027-33.
120. Wannapakdee W, Wattanakit C, Paluka V, Yutthalekha T, Limtrakul J. One-pot synthesis of novel hierarchical bifunctional Ga/HZSM-5 nanosheets for propane aromatization. **RSC Advances**. 2016;6(4):2875-81.

121. Tsao K, Yang H. **Oxygen reduction catalysts on nanoparticle electrodes.** Encyclopedia of Interfacial Chemistry: Surface Science and Electrochemistry: Elsevier; 2018. p. 796-811.
122. Kinger G, Lugstein A, Swagera R, Ebel M, Jentys A, Vinek H. Comparison of impregnation, liquid-and solid-state ion exchange procedures for the incorporation of nickel in HMF1, HMOR and HBEA: Activity and selectivity in n-nonane hydroconversion. **Microporous and mesoporous materials.** 2000;39(1-2):307-17.
123. Wang X, Liu D, Song S, Zhang H. Pt@CeO₂ Multicore@Shell Self-Assembled Nanospheres: Clean Synthesis, Structure Optimization, and Catalytic Applications. **Journal of the American Chemical Society.** 2013;135(42):15864-72.
124. Noor M, Al Mamun M, Ullah AA, Matsuda A, Kawamura G, Hakim M, et al. Physics of Ce³⁺↔ Ce⁴⁺ electronic transition in phytosynthesized CeO₂/CePO₄ nanocomposites and its antibacterial activities. **Journal of Physics and Chemistry of Solids.** 2021;148:109751.
125. Dutta P, Pal S, Seehra MS, Shi Y, Eyring EM, Ernst RD. Concentration of Ce³⁺ and Oxygen Vacancies in Cerium Oxide Nanoparticles. **Chemistry of Materials.** 2006;18(21):5144-6.
126. Schwandt CS. Characterizing nanometer-scale materials using a low-angle backscattered electron detector. **Amer Lab, Nov.** 2010;15:13-7.
127. Plascencia-Villa G, Starr CR, Armstrong LS, Ponce A, José-Yacamán M. Imaging interactions of metal oxide nanoparticles with macrophage cells by ultra-high resolution scanning electron microscopy techniques. **Integrative Biology.** 2012;4(11):1358-66.
128. Perez-Ramirez J, Christensen CH, Egeblad K, Christensen CH, Groen JC. Hierarchical zeolites: enhanced utilisation of microporous crystals in catalysis by advances in materials design. **Chemical Society Reviews.** 2008;37(11):2530-42.
129. Thommes M, Kaneko K, Neimark AV, Olivier JP, Rodriguez-Reinoso F, Rouquerol J, et al. Physisorption of gases, with special reference to the evaluation of surface area and pore size distribution (IUPAC Technical Report). **Pure and Applied Chemistry.** 2015;87(9-10):1051-69.

130. Liu J, Jiang G, Liu Y, Di J, Wang Y, Zhao Z, et al. Hierarchical macro-meso-microporous ZSM-5 zeolite hollow fibers with highly efficient catalytic cracking capability. **Scientific reports**. 2014;4(1):1-6.
131. Zheng X, Li Y, Zhang L, Shen L, Xiao Y, Zhang Y, et al. Insight into the effect of morphology on catalytic performance of porous CeO₂ nanocrystals for H₂S selective oxidation. **Applied Catalysis B: Environmental**. 2019;252:98-110.
132. Chen D, He D, Lu J, Zhong L, Liu F, Liu J, et al. Investigation of the role of surface lattice oxygen and bulk lattice oxygen migration of cerium-based oxygen carriers: XPS and designed H₂-TPR characterization. **Applied Catalysis B: Environmental**. 2017;218:249-59.
133. Wei Y, Liu J, Zhao Z, Duan A, Jiang G. The catalysts of three-dimensionally ordered macroporous Ce_{1-x}Zr_xO₂-supported gold nanoparticles for soot combustion: The metal-support interaction. **Journal of Catalysis**. 2012;287:13-29.
134. Scire` S, Minic` S, Crisafulli C, Satriano C, Pistone A. Catalytic combustion of volatile organic compounds on gold/cerium oxide catalysts. **Applied Catalysis B: Environmental**. 2003;40(1):43-9.
135. Tana, Zhang M, Li J, Li H, Li Y, Shen W. Morphology-dependent redox and catalytic properties of CeO₂ nanostructures: Nanowires, nanorods and nanoparticles. **Catalysis Today**. 2009;148(1):179-83.
136. Chen J, Zhang Q, Wang Y, Wan H. Size-Dependent Catalytic Activity of Supported Palladium Nanoparticles for Aerobic Oxidation of Alcohols. **Advanced Synthesis & Catalysis**. 2008;350(3):453-64.
137. Flores C, Batalha N, Marcilio NR, Ordonsky VV, Khodakov AY. Influence of Impregnation and Ion Exchange Sequence on Metal Localization, Acidity and Catalytic Performance of Cobalt BEA Zeolite Catalysts in Fischer-Tropsch Synthesis. **ChemCatChem**. 2019;11(1):568-74.
138. Kwak G, Yong K. Adsorption and reaction of ethanol on ZnO nanowires. **The Journal of Physical Chemistry C**. 2008;112(8):3036-41.
139. Davis SE, Ide MS, Davis RJ. Selective oxidation of alcohols and aldehydes over supported metal nanoparticles. **Green Chemistry**. 2013;15(1):17-45.
140. Marotta R, Di Somma I, Spasiano D, Andreozzi R, Caprio V. Selective oxidation of benzyl alcohol to benzaldehyde in water by TiO₂/Cu (II)/UV solar system. **Chemical engineering journal**. 2011;172(1):243-9.

141. Della Pina C, Falletta E, Rossi M. Highly selective oxidation of benzyl alcohol to benzaldehyde catalyzed by bimetallic gold–copper catalyst. **Journal of Catalysis**. 2008;260(2):384-6.
142. Satrio JA, Doraiswamy L. Production of benzaldehyde: a case study in a possible industrial application of phase-transfer catalysis. **Chemical Engineering Journal**. 2001;82(1-3):43-56.
143. Parmeggiani C, Cardona F. Transition metal based catalysts in the aerobic oxidation of alcohols. **Green Chemistry**. 2012;14(3):547-64.
144. Seddon KR, Stark A. Selective catalytic oxidation of benzyl alcohol and alkylbenzenes in ionic liquids. **Green Chemistry**. 2002;4(2):119-23.
145. Gamez P, Arends IW, Reedijk J, Sheldon RA. Copper (II)-catalysed aerobic oxidation of primary alcohols to aldehydes. **Chemical Communications**. 2003(19):2414-5.
146. Karimi B, Abedi S, Clark JH, Budarin V. Highly Efficient Aerobic Oxidation of Alcohols Using a Recoverable Catalyst: The Role of Mesoporous Channels of SBA-15 in Stabilizing Palladium Nanoparticles. **Angewandte Chemie International Edition**. 2006;45(29):4776-9.
147. Choudhary VR, Dhar A, Jana P, Jha R, Uphade BS. A green process for chlorine-free benzaldehyde from the solvent-free oxidation of benzyl alcohol with molecular oxygen over a supported nano-size gold catalyst. **Green Chemistry**. 2005;7(11):768-70.
148. Tsunoyama H, Sakurai H, Negishi Y, Tsukuda T. Size-Specific Catalytic Activity of Polymer-Stabilized Gold Nanoclusters for Aerobic Alcohol Oxidation in Water. **Journal of the American Chemical Society**. 2005;127(26):9374-5.
149. Maity P, Gopinath CS, Bhaduri S, Lahiri GK. Applications of a high performance platinum nanocatalyst for the oxidation of alcohols in water. **Green Chemistry**. 2009;11(4):554-61.
150. Wang Q, Cai X, Liu Y, Xie J, Zhou Y, Wang J. Pd nanoparticles encapsulated into mesoporous ionic copolymer: Efficient and recyclable catalyst for the oxidation of benzyl alcohol with O₂ balloon in water. **Applied Catalysis B: Environmental**. 2016;189:242-51.
151. Marelli M, Jouve A, Villa A, Psaro R, Balerna A, Prati L, et al. Hybrid Au/CuO Nanoparticles: Effect of Structural Features for Selective Benzyl Alcohol Oxidation. **The Journal of Physical Chemistry C**. 2019;123(5):2864-71.

152. Olmos CM, Chinchilla LE, Villa A, Delgado JJ, Hungría AB, Blanco G, et al. Size, nanostructure, and composition dependence of bimetallic Au–Pd supported on ceria–zirconia mixed oxide catalysts for selective oxidation of benzyl alcohol. **Journal of Catalysis**. 2019;375:44-55.
153. Enache DI, Edwards JK, Landon P, Solsona-Espriu B, Carley AF, Herzing AA, et al. Solvent-free oxidation of primary alcohols to aldehydes using Au-Pd/TiO₂ catalysts. **Science**. 2006;311(5759):362-5.
154. Murphin Kumar PS, Thiripuranthagan S, Imai T, Kumar G, Pugazhendhi A, Vijayan SR, et al. Pt Nanoparticles Supported on Mesoporous CeO₂ Nanostructures Obtained through Green Approach for Efficient Catalytic Performance toward Ethanol Electro-oxidation. **ACS Sustainable Chemistry & Engineering**. 2017;5(12):11290-9.
155. Tanaka A, Hashimoto K, Kominami H. Preparation of Au/CeO₂ Exhibiting Strong Surface Plasmon Resonance Effective for Selective or Chemoselective Oxidation of Alcohols to Aldehydes or Ketones in Aqueous Suspensions under Irradiation by Green Light. **Journal of the American Chemical Society**. 2012;134(35):14526-33.
156. Xu C, Shen PK. Novel Pt/CeO₂/C catalysts for electrooxidation of alcohols in alkaline media. **Chemical Communications**. 2004(19):2238-9.
157. Rocchini E, Trovarelli A, Llorca J, Graham GW, Weber WH, Maciejewski M, et al. Relationships between structural/morphological modifications and oxygen storage–redox behavior of silica-doped ceria. **Journal of Catalysis**. 2000;194(2):461-78.
158. Wei S, He H, Cheng Y, Yang C, Zeng G, Kang L, et al. Preparation, characterization, and catalytic performances of cobalt catalysts supported on KIT-6 silicas in oxidative desulfurization of dibenzothiophene. **Fuel**. 2017;200:11-21.
159. Kang L, Liu H, He H, Yang C. Oxidative desulfurization of dibenzothiophene using molybdenum catalyst supported on Ti-pillared montmorillonite and separation of sulfones by filtration. **Fuel**. 2018;234:1229-37.
160. Yang C, Zhao K, Cheng Y, Zeng G, Zhang M, Shao J, et al. Catalytic oxidative desulfurization of BT and DBT from n-octane using cyclohexanone peroxide and catalyst of molybdenum supported on 4A molecular sieve. **Separation and Purification Technology**. 2016;163:153-61.

161. Qiu L, Cheng Y, Yang C, Zeng G, Long Z, Wei S, et al. Oxidative desulfurization of dibenzothiophene using a catalyst of molybdenum supported on modified medicinal stone. **Rsc Advances**. 2016;6(21):17036-45.
162. Moeini SS, Battocchio C, Casciardi S, Luisetto I, Lupattelli P, Tofani D, et al. Oxidized Palladium Supported on Ceria Nanorods for Catalytic Aerobic Oxidation of Benzyl Alcohol to Benzaldehyde in Protic Solvents. **Catalysts**. 2019;9(10):847.
163. Xu J, Shang J-K, Chen Y, Wang Y, Li Y-X. Palladium nanoparticles supported on mesoporous carbon nitride for efficiently selective oxidation of benzyl alcohol with molecular oxygen. **Applied Catalysis A: General**. 2017;542:380-8.
164. Ramirez-Barria CS, Isaacs M, Parlett C, Wilson K, Guerrero-Ruiz A, Rodríguez-Ramos I. Ru nanoparticles supported on N-doped reduced graphene oxide as valuable catalyst for the selective aerobic oxidation of benzyl alcohol. **Catalysis Today**. 2019.
165. Tamizhdurai P, Sakthinathan S, Krishnan PS, Ramesh A, Abilarasu A, Mangesh VL, et al. Highly selective oxidation of benzyl alcohol over Pt-sulphated zirconia supported on SBA-15 catalyst by using a high-pressure fixed bed reactor. **Polyhedron**. 2018;155:390-7.
166. Liu J, Yuan Q, Zhao H, Zou S. Efficient Room-Temperature Selective Oxidation of Benzyl Alcohol into Benzaldehyde Over Pt/BiOCl Nanocomposite. **Catalysis Letters**. 2018;148(4):1093-9.
167. Corma A. State of the art and future challenges of zeolites as catalysts. **Journal of Catalysis**. 2003;216(1-2):298-312.
168. Meng L, Mezari B, Goesten MG, Hensen EJM. One-Step Synthesis of Hierarchical ZSM-5 Using Cetyltrimethylammonium as Mesopore-directing and Structure-Directing Agent. **Chemistry of Materials**. 2017;29(9):4091-6.
169. Meng L, Zhu X, Wannapakdee W, Pestman R, Goesten MG, Gao L, et al. A dual-templating synthesis strategy to hierarchical ZSM-5 zeolites as efficient catalysts for the methanol-to-hydrocarbons reaction. **Journal of Catalysis**. 2018;361:135-42.
170. Ambroz F, Macdonald TJ, Martis V, Parkin IP. Evaluation of the BET Theory for the Characterization of Meso and Microporous MOFs. **Small Methods**. 2018;2(11):1800173.

171. Galarneau A, Mehlhorn D, Guenneau F, Coasne B, Villemot F, Minoux D, et al. Specific surface area determination for microporous/mesoporous materials: The case of mesoporous FAU-Y zeolites. **Langmuir**. 2018;34(47):14134-42.
172. Galarneau A, Villemot F, Rodriguez J, Fajula F, Coasne B. Validity of the t-plot Method to Assess Microporosity in Hierarchical Micro/Mesoporous Materials. **Langmuir**. 2014;30(44):13266-74.
173. Fadoni M, Lucarelli L, Dąbrowski A. Temperature programmed desorption, reduction, oxidation and flow chemisorption for the characterisation of heterogeneous catalysts. Theoretical aspects, instrumentation and applications. **Studies in Surface Science and Catalysis**. 1999;120:177-225.
174. Sing KS. Physisorption of nitrogen by porous materials. **Journal of Porous Materials**. 1995;2(1):5-8.
175. Sotomayor FJ, Cychosz KA, Thommes M. Characterization of micro/mesoporous materials by physisorption: concepts and case studies. **Acc Mater Surf Res**. 2018;3:34-50.
176. Perrichon V, Retailleau L, Bazin P, Daturi M, Lavalley JC. Metal dispersion of CeO₂-ZrO₂ supported platinum catalysts measured by H₂ or CO chemisorption. **Applied Catalysis A: General**. 2004;260(1):1-8.
177. Ke J, Zhu W, Jiang Y, Si R, Wang Y-J, Li S-C, et al. Strong Local Coordination Structure Effects on Subnanometer PtO_x Clusters over CeO₂ Nanowires Probed by Low-Temperature CO Oxidation. **ACS Catalysis**. 2015;5(9):5164-73.
178. Jiang C, Wang Y, Zhang H, Chang N, Li L, Xie K, et al. Effect of initial Si/Al ratios on the performance of low crystallinity H β -x zeolite supported NiMo carbide catalysts for aromatics hydrogenation. **Catalysis Science & Technology**. 2019;9(18):5031-44.
179. Treesukul P, Srisuk K, Limtrakul J, Truong TN. Nature of the Metal- Support Interaction in Bifunctional Catalytic Pt/H-ZSM-5 Zeolite. **The Journal of Physical Chemistry B**. 2005;109(24):11940-5.
180. Overbury S, Huntley D, Mullins D, Glavee G. XANES studies of the reduction behavior of (Ce_{1-y}Zr_y)O₂ and Rh/(Ce_{1-y}Zr_y)O₂. **Catalysis letters**. 1998;51(3-4):133-8.

181. Sims CM, Maier RA, Johnston-Peck AC, Gorham JM, Hackley VA, Nelson BC. Approaches for the quantitative analysis of oxidation state in cerium oxide nanomaterials. **Nanotechnology**. 2018;30(8):085703.
182. Phokha S, Pinitsoontorn S, Maensiri S. Structure and magnetic properties of monodisperse Fe 3+-doped CeO₂ nanospheres. **Nano-Micro Letters**. 2013;5(4):223-33.
183. Qiu N, Zhang J, Wu Z, Hu T, Liu P. Tuning ceria nanocrystals morphology and structure by copper doping. **Crystal Growth & Design**. 2011;12(2):629-34.
184. Chen Y, Chen J, Qu W, George C, Aouine M, Vernoux P, et al. Well-defined palladium–ceria interfacial electronic effects trigger CO oxidation. **Chemical Communications**. 2018;54(72):10140-3.
185. Guo Z, Liu B, Zhang Q, Deng W, Wang Y, Yang Y. Recent advances in heterogeneous selective oxidation catalysis for sustainable chemistry. **Chemical Society Reviews**. 2014;43(10):3480-524.
186. Sun N, Hou Y, Wu W, Niu M, Wang W. Electro-oxidation of benzyl alcohol to benzaldehyde in supercritical CO₂ with ionic liquid. **Electrochemistry Communications**. 2013;28:34-6.
187. Enache DI, Edwards JK, Landon P, Solsona-Espriu B, Carley AF, Herzing AA, et al. Solvent-Free Oxidation of Primary Alcohols to Aldehydes Using Au-Pd/TiO₂ Catalysts. **Science**. 2006;311(5759):362.
188. Wang C, Yin H, Dai S, Sun S. A general approach to noble metal– metal oxide dumbbell nanoparticles and their catalytic application for CO oxidation. **Chemistry of Materials**. 2010;22(10):3277-82.
189. Rautiainen S, Chen J, Vehkamäki M, Repo T. Oxidation of vanillin with supported gold nanoparticles. **Topics in catalysis**. 2016;59(13):1138-42.
190. Yang Y, Chen Y, Du X-q, Feng S, Zhang Z. Study of Anodic Electrodeposition of CeO₂ Thin Film Using Electrochemical Noise Technique. **Int J Electrochem Sci**. 2018;13:384-95.
191. Lu X-h, Huang X, Xie S-l, Zheng D-z, Liu Z-q, Liang C-l, et al. Facile electrochemical synthesis of single crystalline CeO₂ octahedrons and their optical properties. **Langmuir**. 2010;26(10):7569-73.
192. Crooks RM. Principles of Bipolar Electrochemistry. **ChemElectroChem**. 2016;3(3):357-9.

193. Ramakrishnan S, Shannon C. Display of solid-state materials using bipolar electrochemistry. **Langmuir**. 2010;26(7):4602-6.
194. Lundgren A, Munktel S, Lacey M, Berglin M, Björefors F. Formation of gold nanoparticle size and density gradients via bipolar electrochemistry. **ChemElectroChem**. 2016;3(3):378-82.
195. Li Y, Dong Y, Yang Y, Yu P, Zhang Y, Hu J, et al. Rational design of silver gradient for studying size effect of silver nanoparticles on contact killing. **ACS Biomaterials Science & Engineering**. 2018;5(2):425-31.
196. Beugré R, Dorval A, Lavallée LL, Jafari M, Byers JC. Local electrochemistry of nickel (oxy)hydroxide material gradients prepared using bipolar electrodeposition. **Electrochimica Acta**. 2019;319:331-8.
197. Eckhard K, Chen X, Turcu F, Schuhmann W. Redox competition mode of scanning electrochemical microscopy (RC-SECM) for visualisation of local catalytic activity. **physical chemistry chemical physics**. 2006;8(45):5359-65.
198. Zhitomirsky I. Ceramic films using cathodic electrodeposition. **JOM-e**. 2000;52(1):1019745774-24607.
199. Kozu Y, Kawashima S, Kitamura F. One-step electrochemical synthesis of Pt–CeO₂ composite thin films on a glassy carbon electrode. **Journal of Solid State Electrochemistry**. 2013;17(3):761-5.
200. Hamlaoui Y, Tifouti L, Remazeilles C, Pedraza F. Cathodic electrodeposition of cerium based oxides on carbon steel from concentrated cerium nitrate. Part II: Influence of electrodeposition parameters and of the addition of PEG. **Materials Chemistry and Physics**. 2010;120(1):172-80.
201. Yang L, Pang X, Fox-Rabinovich G, Veldhuis S, Zhitomirsky I. Electrodeposition of cerium oxide films and composites. **Surface and Coatings Technology**. 2011;206(1):1-7.
202. Abellan P, Moser TH, Lucas IT, Grate JW, Evans JE, Browning ND. The formation of cerium (iii) hydroxide nanoparticles by a radiation mediated increase in local pH. **RSC advances**. 2017;7(7):3831-7.
203. Whalen III JJ, Weiland JD, Searson PC. Electrochemical deposition of platinum from aqueous ammonium hexachloroplatinate solution. **Journal of the Electrochemical Society**. 2005;152(11):C738.
204. Zhou Y, Menéndez CL, Guinel MJF, Needels EC, González-González I, Jackson DL, et al. Influence of nanostructured ceria support on platinum

- nanoparticles for methanol electrooxidation in alkaline media. **Rsc Advances**. 2014;4(3):1270-5.
205. Meng F, Fan Z, Zhang C, Hu Y, Guan T, Li A. Morphology-controlled synthesis of CeO₂ microstructures and their room temperature ferromagnetism. **Journal of Materials Science & Technology**. 2017;33(5):444-51.
206. Hong X, Sun Y. Effect of Preparation Methods on the Performance of Pt/CeO₂ Catalysts for the Catalytic Oxidation of Carbon Monoxide. **Catalysis Letters**. 2016;146(10):2001-8.
207. Qin J, Zhang Y, Leng D, Yin F. The enhanced activity of Pt–Ce nanoalloy for oxygen electroreduction. **Scientific Reports**. 2020;10(1):1-7.
208. Dronova M, Lair V, Vermaut P, Ringuedé A, An V. Study of ceria thin films prepared via electrochemical deposition: Role of selected electrochemical parameters on growth kinetics. **Thin Solid Films**. 2020;693:137674.
209. Huang Y-F, Kooyman PJ, Koper MTM. Intermediate stages of electrochemical oxidation of single-crystalline platinum revealed by in situ Raman spectroscopy. **Nature communications**. 2016;7(1):1-7.
210. Pozio Ad, De Francesco M, Cemmi A, Cardellini F, Giorgi L. Comparison of high surface Pt/C catalysts by cyclic voltammetry. **Journal of power sources**. 2002;105(1):13-9.
211. Zhou C, Chen Y, Guo Z, Wang X, Yang Y. Promoted aerobic oxidation of benzyl alcohol on CNT supported platinum by iron oxide. **Chemical Communications**. 2011;47(26):7473-5.
212. Xu F, Wang D, Sa B, Yu Y, Mu S. One-pot synthesis of Pt/CeO₂/C catalyst for improving the ORR activity and durability of PEMFC. **International Journal of Hydrogen Energy**. 2017;42(18):13011-9.
213. Wu H, Song J, Liu H, Xie Z, Xie C, Hu Y, et al. An electrocatalytic route for transformation of biomass-derived furfural into 5-hydroxy-2 (5 H)-furanone. **Chemical science**. 2019;10(17):4692-8.
214. Gong L, Agrawal N, Roman A, Holewinski A, Janik MJ. Density functional theory study of furfural electrochemical oxidation on the Pt (1 1 1) surface. **Journal of catalysis**. 2019;373:322-35.
215. Thiyagarajan S, Franciolus D, Bisselink RJ, Ewing TA, Boeriu CG, Van Haveren J. Selective production of maleic acid from furfural via a cascade approach

- combining photochemistry and electro-or biochemistry. **ACS sustainable chemistry & engineering**. 2020;8(29):10626-32.
216. Jung S, Karaiskakis AN, Biddinger EJ. Enhanced activity for electrochemical hydrogenation and hydrogenolysis of furfural to biofuel using electrodeposited Cu catalysts. **Catalysis Today**. 2019;323:26-34.
217. Xu C, Paone E, Rodríguez-Padrón D, Luque R, Mauriello F. Recent catalytic routes for the preparation and the upgrading of biomass derived furfural and 5-hydroxymethylfurfural. **Chemical Society Reviews**. 2020;49(13):4273-306.
218. Parpot P, Bettencourt A, Chamoulaud G, Kokoh K, Belgsir E. Electrochemical investigations of the oxidation–reduction of furfural in aqueous medium: Application to electrosynthesis. **Electrochimica Acta**. 2004;49(3):397-403.
219. Cao Y, Noël T. Efficient electrocatalytic reduction of furfural to furfuryl alcohol in a microchannel flow reactor. **Organic process research & development**. 2019;23(3):403-8.
220. Audemar M, Wang Y, Zhao D, Royer S, Jérôme F, Len C, et al. Synthesis of furfuryl alcohol from furfural: a comparison between batch and continuous flow reactors. **Energies**. 2020;13(4):1002.
221. Brosnahan JT, Zhang Z, Yin Z, Zhang S. Electrocatalytic reduction of furfural with high selectivity to furfuryl alcohol using AgPd alloy nanoparticles. **Nanoscale**. 2021;13(4):2312-6.
222. Shan N, Hanchett MK, Liu B. Mechanistic insights evaluating Ag, Pb, and Ni as electrocatalysts for furfural reduction from first-principles methods. **The Journal of Physical Chemistry C**. 2017;121(46):25768-77.
223. Chadderdon XH, Chadderdon DJ, Matthiesen JE, Qiu Y, Carraher JM, Tessonnier J-P, et al. Mechanisms of furfural reduction on metal electrodes: Distinguishing pathways for selective hydrogenation of bioderived oxygenates. **Journal of the American Chemical Society**. 2017;139(40):14120-8.
224. Román AM, Hasse JC, Medlin JW, Holewinski A. Elucidating acidic electro-oxidation pathways of furfural on platinum. **ACS Catalysis**. 2019;9(11):10305-16.
225. Jiang N, Liu X, Dong J, You B, Liu X, Sun Y. Electrocatalysis of Furfural Oxidation Coupled with H₂ Evolution via Nickel-Based Electrocatalysts in Water. **ChemNanoMat**. 2017;3(7):491-5.

226. Dixit RJ, Bhattacharyya K, Ramani VK, Basu S. Electrocatalytic hydrogenation of furfural using non-noble-metal electrocatalysts in alkaline medium. **Green Chemistry**. 2021.
227. Zhang X, Han M, Liu G, Wang G, Zhang Y, Zhang H, et al. Simultaneously high-rate furfural hydrogenation and oxidation upgrading on nanostructured transition metal phosphides through electrocatalytic conversion at ambient conditions. **Applied Catalysis B: Environmental**. 2019;244:899-908.
228. Shida N, Inagi S. Bipolar electrochemistry in synergy with electrophoresis: electric field-driven electrosynthesis of anisotropic polymeric materials. **Chemical Communications**. 2020;56(92):14327-36.
229. Walther A, Müller AH. Janus particles. **Soft Matter**. 2008;4(4):663-8.
230. Giri SD, Sarkar A. Electrochemical study of bulk and monolayer copper in alkaline solution. **Journal of The Electrochemical Society**. 2016;163(3):H252.
231. Akbari MSA, Bagheri R, Song Z, Najafpour MM. Oxygen-evolution reaction by nickel/nickel oxide interface in the presence of ferrate (VI). **Scientific reports**. 2020;10(1):1-11.

Author's Biography

- Name:** MARISA KETKAEW
- Date of Birth:** December 2nd, 1993
- Place of Birth:** Phayao, Thailand
- Current Address:** 3/28 Bangsaen sai 2, Mueang, Chonburi, 20130
- Education:** Bachelor of Engineering in Chemical Engineering (First-class honours), Burapha University, Chonburi, Thailand (2012-2015)
- Scholarship:** Recipient of the full scholarship from Faculty of Engineering, Burapha University
- Recipient of the full scholarship from Vidyasirimedhi Institute of Science and Technology (VISTEC)
- Recipient of the Franco-Thai scholarship from France Embassy.
- Academic Publication:** Wetchasat P, Salakhum S, Imyen T, Suttipat D, Wannapakdee W, **Ketkaew M**, Prasertsab A, Kidkhunthod P, Witoon T, Wattanakit C. One-Pot Synthesis of Ultra-Small Pt Dispersed on Hierarchical Zeolite Nanosheet Surfaces for Mild Hydrodeoxygenation of 4-Propylphenol. **Catalysts**, 2021; 11: 333.
- Suttipat D, Saenluang K, Wannapakdee W, Dugkhuntod P, **Ketkaew M**, Pornsetmetakul P, Wattanakit C. Fine-tuning the surface acidity of hierarchical zeolite composites for methanol-to-olefins (MTO) reaction. **Fuel**, 2020; 286: 11930.

Saenluang K, Imyen T, Wannapakdee W, Suttipat D, Dugkhuntod P, **Ketkaew M**, Thivasasith A, Wattanakit C. Hierarchical nanospherical ZSM-5 nanosheets with uniform Al distribution for alkylation of benzene with ethanol. **ACS Applied Nano Materials**, 2020; 3: 3252-3263.

Ketkaew M, Klinyod S, Saenluang K, Rodaum C, Thivasasith A, Kidkhunthod P, Wattanakit C. Fine-tuning the chemical state and acidity of ceria incorporated in hierarchical zeolites for ethanol dehydration. **Chemical Communications**, 2020; 56: 11394-11397.

Assavapanumat S, **Ketkaew M**, Kuhn A, Wattanakit C. Synthesis, characterization, and electrochemical applications of chiral imprinted mesoporous Ni surfaces. *Journal of the American Chemical Society*, 2019; 141: 18870-18876.

Ketkaew M, Suttipat D, Kidkhunthod P, Witoon T, Wattanakit C. Nanoceria-modified platinum supported on hierarchical zeolites for selective alcohol oxidation. **RSC Advances**, 2019; 9: 36027-36033.

Assavapanumat S, **Ketkaew M**, Garrigue P, Lapeyre V, Reculosa S, Wattanakit C, Kuhn A. Hierarchical multiporous nickel for oxygen evolution reaction in alkaline media. **ChemCatChem**, 2019; 11: 5951 – 5960.